DISSERTATION

Machine Learning-Enhanced Numerical Modeling of Modern Magnetoresistive Memories

ausgeführt zum Zwecke der Erlangung des akademischen Grades
eines Doktors der technischen Wissenschaften

unter der Betreuung von

Privatdoz. MSc PhD Viktor Sverdlov

eingereicht an der Technischen Universität Wien
Fakultät für Elektrotechnik und Informationstechnik
von

Johannes Ender, MSc.
Matrikelnummer: 01629746

Wien, im März 2024 __________________________

Abstract

The continuous down-scaling of semiconductor devices over the past decades has led to higher integration density but also higher standby power consumption due to increased leakage currents. Novolatile memory is a promising solution to this problem. Magnetoresistive random access memory (MRAM) poses to be a suitable non-volatile alternative due to its straightforward architecture and compatibility with CMOS technology. It offers the benefits of high speed and excellent endurance, making it an attractive choice for a variety of applications including IoT and automotive applications, as well as embedded DRAM and last-level cache memory. Effective simulation tools provide crucial insights for designing MRAM devices. The process of understanding how the magnetization changes over time in these devices, involves solving the Landau-Lifshitz-Gilbert (LLG) equation. This equation can be enhanced with additional terms that account for the torque acting on the magnetization, which is essential for MRAM functionality. This work is dedicated to the computational study and machine-learning assisted optimization of MRAM devices.

The first part of this work focuses on the study of the finite element method (FEM) based computation of the demagnetizing field, a crucial contribution to the effective field originating from the long-range interaction of the magnetic moments. Computational solutions to remedy the challenges of the open-boundary problem are implemented, and their performance is evaluated.

The second part of this thesis introduces novel computational approaches that combine reinforcement learning with micromagnetic simulations for MRAM device optimization. Traditionally, the application of current pulses to switch magnetoresistive memory cells relies on heuristics. However, this work demonstrates the effectiveness of reinforcement learning in MRAM device control. By autonomously interacting with the simulation, a reinforcement learning agent discovers optimal switching pulse sequences and optimizes various objectives, eliminating the need for manual experimentation.

This approach offers a promising solution for enhancing the efficiency and effectiveness of MRAM switching. The approach demonstrates that an agent trained on a fixed set of parameters can effectively transfer its knowledge of magnetization dynamics in the free layer to scenarios with varying environmental conditions. It is shown that over a wide range of material parameters, the agent is capable of achieving reversal of the free layer magnetization. Additionally, the approach is extended to SOT-assisted STT-MRAM, and it is shown that by modifying the rewarding strategy the focus of the learned pulse scheme can successfully be shifted towards different objectives. Specifically, optimization for both fast magnetization reversal and energy-efficient switching is performed. By condensing the dynamically applied pulses of the reinforcement learning agent, static pulse sequences are obtained that perform well across a wide parameter range.

Kurzfassung

Die über Jahrzente hinweg anhaltende Verkleinerung von Halbleiterbauelementen hat neben einer erhöhten Integrationsdichte auch zu einer Zunahme des Stromverbrauchs im Standby-Modus aufgrund höherer Leckströme geführt. Bei der Lösung dieses Problems sind nichtflüchtige Speicher eine aussichtsreiche Technologie. Der magnetoresistive Direktzugriffsspeicher (MRAM) stellt aufgrund seiner einfachen Architektur und Kompatibilität mit der CMOS-Technologie eine vielversprechende nichtflüchtige Alternative zu ladungsbasierten Speichern dar. Er bietet den Vorteil hoher Geschwindigkeit und einer hervorragenden Lebensdauer, was ihn zu einer attraktiven Wahl für eine Vielzahl von Anwendungen macht, darunter IoT- und Automobil Anwendungen sowie eingebettete DRAM- und Last-Level-Cache-Speicher. Effiziente Simulationswerkzeuge liefern wichtige Erkenntnisse für die Entwicklung von MRAM-Bauteilen. Hierbei ist es wichtig, die Dynamik der Magnetisierung in diesen Bauelementen über die Zeit zu verstehen, wofür die Landau-Lifshitz-Gilbert-Gleichung (LLG) gelöst werden muss. Durch zusätzliche Terme erweitert, welche das auf die Magnetisierung wirkende Drehmoment beschreiben, kann diese Gleichung für die Simulation von MRAM-Bauelementen verwendet werden. Diese Arbeit widmet sich der rechnerischen Untersuchung und der durch maschinelles Lernen unterstützten Optimierung von MRAM Bauelementen.

Der erste Teil der Arbeit konzentriert sich auf die Untersuchung der auf der Finite-Elemente-Methode (FEM) basierenden Berechnung des Demagnetisierungs-Feldes, einem entscheidenden Bestandteil des effektiven magnetischen Feldes, welches durch die langreichweitige Wechselwirkung der magnetischen Momente zustande kommt. Computergestützte Lösungen zur Überwindung des in diesem Feld auftretenden Problems der nur asymptotisch bekannten Randwerte werden implementiert und die Qualität der Resultate wird bewertet.

Der zweite Teil dieser Arbeit stellt neuartige Ansätze vor, welche Algorithmen des bestärkenden Lernens mit mikromagnetischen Simulationen zur Optimierung von MRAM-Bauelementen kombinieren. Traditionell basiert das Anlegen von Strom- oder Spannungsimpulsen zum Schalten magnetoresistiver Speicherzellen auf Heuristiken. Diese Arbeit demonstriert jedoch die Effektivität des bestärkenden Lernens bei der Steuerung von MRAM-Bauelementen. Durch autonome Interaktion mit einer Simulation lernt ein Agent Schaltpulssequenzen bezüglich verschiedener Ziele zu optimieren, wodurch das manuelle Durchführen von Experimenten überflüssig wird. Dieser Ansatz bietet eine vielversprechende Lösung zur Verbesserung der Effizienz und Effektivität von MRAM-Schaltungen. Zudem wird gezeigt, dass ein Agent, der mit einem festen Satz von Parametern trainiert wurde, sein Wissen über die Magnetisierungsdynamik der Speicherzelle effektiv auf Szenarien mit variierenden Bedingungen übertragen kann. Es wird gezeigt, dass der Agent über einen weiten Bereich von Materialparametern in der Lage ist, die Umkehrung der Magnetisierung der freien Schicht zu erreichen. Darüber hinaus wird der Ansatz auf SOT-unterstützten STT-MRAM ausgeweitet, und es wird gezeigt, dass durch Modifizierung der Belohnungsstrategie der Fokus der erlernten Impulsfolgen auf andere Ziele verlagert werden kann. Insbesondere wird eine Optimierung sowohl für eine schnelle Umkehr der Magnetisierung als auch für energieeffizientes Schalten durchgeführt. Durch die Analyse des dynamischen Agentenverhaltens werden statische Impulsfolgen extrahiert, die über einen großen Parameterbereich zu erfolgreichem Schalten der Speicherzelle führen.

Acknowledgement

First and foremost, I would like to express my deepest gratitude to my supervisor, Dr. Viktor Sverdlov, for his continuous support and guidance throughout my PhD studies.

Prof. Siegfried Selberherr deserves thanks for founding the Institute for Microelectronics in the first place, for promoting stimulating exchange in weekly seminars, and for being a great source of inspiration and cutting-edge literature.

I am grateful to have had the opportunity to work in the Christian Doppler Laboratory for Nonvolatile Magnetoresistive Memory and Logic, which was a great environment for my research. My team mates Roberto, Simone, Tomáš, Mario, Nils, Wilton, and Bernhard deserve thanks for their collaboration and all the stimulating discussions.

I would also like to thank all my other colleagues at the Institute for Microelectronics for the enjoyable discussions and the friendly atmosphere. Thanks go to Diana, for the constant support in all organizational matters, as well as to Manfred and Cerv, who make sure that the infrastructure at the institute is always up and running.

Special thanks go to my office mate Roberto, who always had an open ear for my questions and problems and for all the joint coffee breaks.

I am also grateful to my friends and family for their support throughout all my years of study.

Finally, I would like to thank my partner Pia for her patience and understanding during the last years. Everything would have been considerably harder without her support and encouragement.

Contents

List of Figures

List of Tables

List of Algorithms

List of Abbreviations

AP	antiparallel
DRAM	dynamic random access memory
FDM	finite difference method
FEM	finite element method
FL	free layer
FM	ferromagnetic
GMR	giant magnetoresistance
HM	heavy metal
IMA	in-plane magnetic anisotropy
LLG	Landau-Lifshitz-Gilbert
ML	machine learning
MRAM	magnetoresistive random-access memory
MTJ	magnetic tunnel junction
NM	nonmagnetic
P	parallel
PDE	partial differential equation
PMA	perpendicular magnetic anisotropy
RL	reference layer
SHE	spin Hall effect
SOT	spin-orbit torque
STT	spin-transfer torque
TB	tunnel barrier
TMR	tunnel magnetoresistance

List of Symbols

$A \quad (J/m)$	Exchange coefficient
$D_e \quad (m^2/s)$	Spin-flip length
$G \quad (S)$	Electrical conductance
$K \quad (J/m^3)$	Anisotropy coefficient
$M_S \quad (A/m)$	Saturation magnetization
$R \quad (\Omega)$	Electrical resistance
α	Gilbert damping constant
η	Spin-transfer torque efficiency
$\gamma \quad (rad/(T\ s))$	Gyromagnetic ratio
$\gamma_0 = -\gamma\mu_0 \quad (m/(A\ s))$	Rescaled gyromagnetic ratio
$\hbar \quad (J\ s)$	Planck constant
$\lambda_J \quad (m)$	Exchange length
$\lambda_\varphi \quad (m)$	Dephasing length
$\lambda_{sf} \quad (m)$	Spin-flip length
$\mathbf{H}_{\text{eff}} \quad (A/m)$	Effective magnetic field
$\mathbf{J}_C \quad (A/m^2)$	Charge current density
$\mathbf{S} \quad (A/m)$	Spin accumulation vector
$\mathbf{T}_S \quad (A/(m\ s))$	Spin torque vector
$\mathbf{m}$	Unit magnetization vector
$\mu_0 \quad (N/A^2)$	Vacuum permeability
$\rho \quad (\Omega\ m)$	Electrical resistivity
$\sigma \quad (S/m)$	Electrical conductivity
θ_{SH}	Spin Hall angle
$e \quad (C)$	Elementary charge
q_π	Action-value function
r	Reward

Chapter 1

Introduction

In modern day computers, nonvolatile memories are an essential part already since the middle of the 20^{th} century. Hard-disk drives provide users with large capacities at low cost. A problem, however, is their relatively slow access times, which lies in the range of 10 ms [1]. Compared to the access times of dynamic random access memory (DRAM) ($<$ 100 ns), one can see that there is a huge mismatch, leading to delays and increased energy consumption due to the time the processing units have to wait for the information fetched from the HDD. The development of the higher speed nonvolatile flash memory tried to solve this performance mismatch [1]. However, flash memory possesses relatively poor endurance and its down-scaling becomes progressively more complex [2].

Thus, in the last decades the field of spintronics, which uses the electron's spin instead of its charge to store information, gained a lot of interest from research as well as industry. Magnetoresistive random access memory (MRAM) displays promising features like the elimination of standby power consumption, while exhibiting excellent endurance and high read and write speed, while being nonvolatile and allowing scalability to high densities [3]. Compared to HDDs, MRAM is addressable purely electrically and does not require a magnetic read head. This puts MRAM devices into a great spot to serve as the next universal memory technology. Stand-alone as well as embedded applications can be covered by MRAM devices [4–20].

The centerpiece of MRAM devices is the magnetic tunnel junction (MTJ), a sandwich of two ferromagnetic layers, separated by a nonmagnetic tunnel barrier. It allows storing one bit of information, encoded in the relative orientation of the two ferromagnetic layers, which, if oriented in parallel, leads to a small electrical resistance of the MTJ, and if oriented antiparallel, leads to a large electrical resistance.

While the MTJ remains the cornerstone of basically every major type of MRAM device, different ways to alter the state of the memory cell were developed over the years. The initial wave of MRAM types focussed on the use of magnetic fields to change the information stored in the MTJ. Stoner-Wohlfarth MRAM (SW-MRAM) used two orthogonal wires through which currents have to be passed in order to select a single memory cell, with the combined effect of the magnetic fields from these current wires leading to magnetization reversal. However, it suffered from write selectivity problems and lacked good scalability [21]. First commercially available MRAM devices were so-called Toggle-MRAM devices. They were field-based as well, but the write margin was improved compared to SW-MRAM, such that half-selected bits had to overcome a significantly higher energy barrier to be switched than the fully selected ones [22]. Still, though, the additional current lines for the generation of the magnetic fields resulted in limited downsize scalability and different methods needed to be developed.

Spin-transfer torque MRAM (STT-MRAM) and spin-orbit torque MRAM (SOT-MRAM) were and still are the two most promising candidates to lead the field of spintronics into the replacement of current volatile CMOS-based memories. They largely eliminated write selectivity issues and external magnetic fields, simplifying their production and increasing their scalability.

The pace at which the field of spintronics developed was strongly supported by the continuous efforts being put into the advancement of the modeling and simulation of these devices. Being able to accurately simulate the magnetization dynamics offers an advantage over relying purely on experiments and helps to deepen the understanding of the devices' behavior.

The Landau-Lifshitz-Gilbert (LLG) equation [23, 24] describes the evolution of the magnetization over time under the influence of an effective magnetic field. Extended with terms describing torques of different origin, which act on the magnetization, it can be used to simulate the behavior of STT- and SOT-MRAM devices. Simulation tools with such capabilities are of high importance, as they allow to rapidly test new cell architectures and anticipate behavior under various boundary conditions. For this purpose, the most widely used computational methods to discretize the LLG equation are the finite difference method (FDM) and the finite element method (FEM) [25]. Each of these methods has its place in the computational toolbox for the simulation of MRAM devices, as the FDM offers higher performance and easier parallelizability, while the FEM can handle even very complex geometries, as encountered in many of today's ultra-scaled MRAM devices. Similar to the increasing interest in spintronic devices, the soaring of computational capabilities has led to widespread use of machine learning algorithms, which since have proven to be a useful tool in basically every scientific discipline [26].

All the above-mentioned computational means are being used in this thesis, showcasing their capabilities and using them to further advance the research on STT- and SOT-MRAM.

1.1 Thesis Outline

This thesis deals with various computational methods and how they can be used to investigate and improve the behavior of modern MRAM devices.

Chapter 2 gives a short introduction into the field of magnetoresistive random access memories and describes its most prominent types.

Chapter 3 then introduces the micromagnetic model, which is the most widespread approach used to describe magnetization dynamics in spintronic devices. The Landau-Lifshitz-Gilbert is presented and the most important contributions to the effective magnetic field are described.

Chapter 4 describes two different methods to spatially discretize the computational domain in simulations, namely, the finite difference method and the finite element method. First, the computational methods are introduced, and then it is shown how the effective magnetic field contributions are discretized in the respective method. After discussing time integration methods, the machine learning sub-branch reinforcement learning is discussed.

Chapter 5 shows computationally efficient approaches for the calculation of the demagnetizing field.

Chapter 6 presents the use of reinforcement learning to facilitate the discovery of novel switching schemes to optimize performance of MRAM devices.

Finally, Chapter 7 gives a summary of the main results of this work.

1.2 Research Setting

The research described in this work was carried out as part of the Christian Doppler Laboratory for Nonvolatile Magnetoresistive Memory and Logic (NOVOMEMLOG). The Christian Doppler Association fosters collaboration between research institutions and companies engaged in application-oriented basic research. In the case of this laboratory, a partnership was formed between the Institute for Microelectronics at the TU Wien and Silvaco Inc., a company developing and providing electronic device automation and software tools for Technology Computer-Aided Design (TCAD).

Chapter 2

Magnetoresistive Memory

2.1 MRAM Basics

2.1.1 Magnetoresistive Effects

For any type of memory device, it is important to understand how information is being stored, how it can be read, and how it can be changed. In the following, giant magnetoresistance (GMR) effect, as well as tunnel magnetoresistance (TMR) effect will be explained, two effects whose discovery has enabled the development of magnetoresistive devices. In general, however, one can say that spintronics deals with the question of how the electron spin can be used to influence the behavior of microelectronic devices.

Giant Magnetoresistance

The GMR effect was discovered independently by two separate research groups in 1988, one led by Albert Fert [27], and the other by Peter Grünberg [28]. Both groups investigated the influence of magnetization on the electrical resistance in stacks of magnetic and nonmagnetic conducting layers. For their discovery, Fert and Grünberg received the Nobel Prize in physics in 2007.

The GMR ratio for a given material stack can be calculated as follows [29]:

$$GMR = \frac{R_{AP} - R_P}{R_P} = \frac{\rho_{AP} - \rho_P}{\rho_P} = \frac{\sigma_P}{\sigma_{AP}} - 1 \tag{2.1}$$

where R_{AP} and R_P denote the resistance in the antiparallel and parallel state, and ρ_{AP} and ρ_P the resistivities and σ_{AP} and σ_P the conductivities in the corresponding magnetization states.

The origin of the GMR is found in electron scattering, a visual depiction can be seen in Fig. 2.1. If the magnetization in the magnetic layers is in a parallel configuration, the majority electrons are subject to less scattering than the minority electrons. Conversely, when the layers are magnetized in an antiparallel configuration, majority and minority electrons undergo equal scattering. Thus, depending on if the alignment of the magnetization in the ferromagnetic layers is antiparallel or parallel, the electrical resistance of the material stack is high or low, respectively.

The discovery of the GMR effect has sparked new interest in magnetoresistive device research and has led to the GMR effect being used in various devices, like hard disks, sensors, and also MRAM cells [21].

Tunnel Magnetoresistance

The TMR effect is another important magnetoresistance effect, with distinct differences to the GMR with respect to the structures it appears in and to its physical origin. This effect was discovered by Michel Julliere in 1975 when Fe/Ge/Co stacks for which a maximum relative change in conductance of 14% at a temperature of $T \leq 4.2K$ was observed between parallel and antiparallel states [30].

Similarly to the GMR, the TMR can be quantified by the following equation [31, 32]:

$$TMR = \frac{R_{AP} - R_P}{R_P} = \frac{G_P - G_{AP}}{G_{AP}} \tag{2.2}$$

with R_{AP} and R_P being the values of the electrical resistance and R_{AP} and R_P being the electrical conductance in the antiparallel and parallel state, respectively. G_P and G_{AP} are the conductances in the respective magnetization configurations. The magnetization in the two layers, however, is

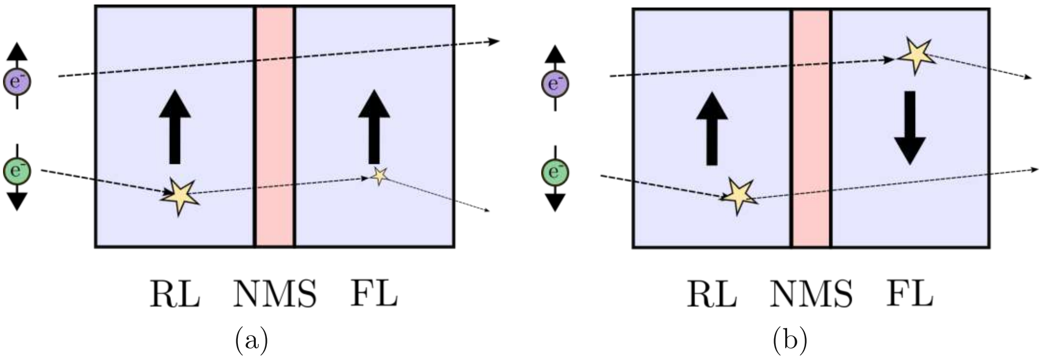

Figure 2.1: Visual depiction of the scattering effects responsible for the GMR effect. The direction of the electron flow is indicated by the dashed arrows. In the parallel configuration (a) of the reference layer (RL) and the free layer (FL), the electrons are subject to less scattering than in the anti-parallel state (b), resulting in lower electrical resistance of the parallel state.

not always in perfect (anti-)parallel alignment, and the conductance of the layered structure can be described by the following equation proportional to the cosine of the angle between the magnetization orientations, θ [32–34]:

$$\begin{aligned} G(\theta) &= \frac{G_P + G_{AP}}{2} + \frac{G_P - G_{AP}}{2} \cos\ \theta \\ &= \frac{G_P + G_{AP}}{2} \left(1 + \frac{TMR}{2 + TMR} \cos\ \theta\right) \end{aligned} \tag{2.3}$$

An explanation of the TMR effect is visualized in Fig. 2.2. The origin of the effect lies in the spin-dependent ability for electrons to tunnel through the non-conducting tunnel barrier. It depends on the majority and minority band matching of the two ferromagnetic layers. Thus, if the ferromagnetic layers are magnetized in parallel, band matching is good and the electrons have a higher probability of tunneling to the second ferromagnetic layer.

While discovered in 1975, it took until 1995, when Miyazaki *et al.* [35] and Moodera *et al.* [36] independently presented experimentally observed TMR ratios of around 20% at room temperature. This was achieved by the use of an amorphous Al_2O_3 barrier, which makes the TMR depend mainly on the electronic structure of the ferromagnetic layers. Using Al_2O_3 as well for the tunnel barrier, TMR ratios of 70% were achieved by Wang *et al.* later in the 1990s [37].

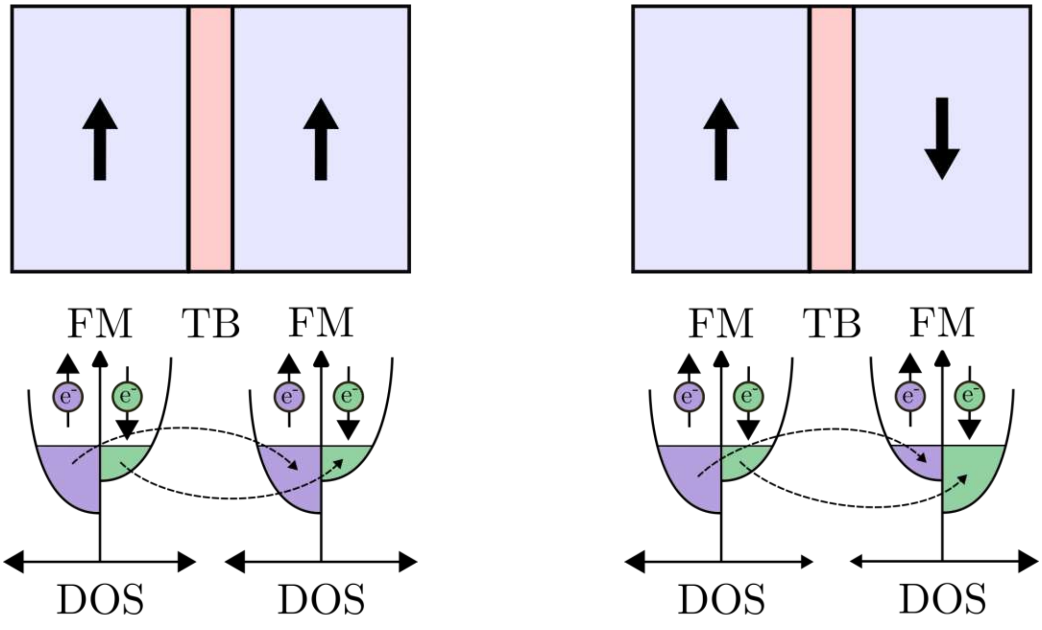

(a) (b)

Figure 2.2: Visual description of the TMR effect. The parallel magnetization state (a) exhibits better band matching as opposed to the antiparallel magnetization state (b), resulting in a lower resistance in the parallel state.

Structures consisting of two ferromagnetic layers separated by a tunnel barrier are also called MTJs and find use in several applications. Among other areas, they are used in HDD read heads [38], but also lie at the core of every magnetoresistive memory device. In these memory devices, the two states to store binary information, are represented by the magnetization states of the MTJ. The parallel state with low resistance representing the logical '0', and the antiparallel state with high resistance representing logical '1'. MTJs are fabricated in a way such that the magnetization in one of the layers, the free layer (FL), is free to move, while the orientation of the magnetization in the other layer, called reference layer (RL), is fixed.

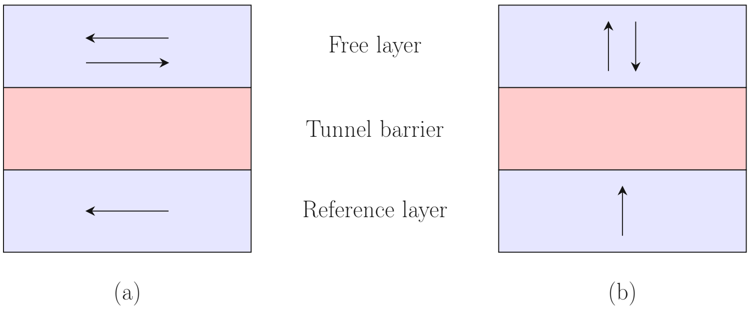

Figure 2.3: Magnetic tunnel junction with (a) in-plane and (b) perpendicular magnetization.

The orientation of the magnetization in the FL and RL can either be in-plane, or perpendicular to the plane, as depicted in Fig. 2.3. The first successfully fabricated MTJs in 1995 used amorphous Al_2O_3 barriers and only exhibited TMRs in the double digits. Soon after, the possibility to achieve higher TMRs by using crystalline MgO barriers was predicted [39, 40] and could be experimentally demonstrated in the years 2004 [41] and 2005 [42,43]. After, the TMR of MgO barriers was gradually improved, reaching 600% at room temperature under laboratory conditions [44]. Typical values for TMR in MTJs of modern perpendicularly magnetized devices are in the range of 100–200% [45].

Reading the stored information from a MTJ is performed by applying a small bias voltage, usually $0.1 - 0.2\ V$, and measuring the resistance. The reason for the small bias voltage is two-fold: firstly, keeping the bias voltage and thus also the current through the structure small reduces the probability of erroneously changing the state of the stored information; secondly, the TMR depends on the bias voltage and exhibits a maximum at very small voltages ($< 0.1\ V$) and reduces with increasing read voltage. For a voltage range of $0.1 - 0.2\ V$, the reduction in TMR is limited to at most 10% [21]. An important property of magnetoresistive random-access memory (MRAM) cells is their thermal stability factor. It is defined as the relation of the energy barrier which separates parallel and antiparallel state to the thermal energy [46]:

$$\Delta = \frac{E_B}{k_B T}, \tag{2.4}$$

with k_B being the Boltzmann constant and the temperature T. The energy barrier E_B is proportional to the magnetic anisotropy and can be calculated as follows:

$$E_B = \frac{\mu_0 M_S \mathbf{H}_K V}{2} \tag{2.5}$$

μ_0 is the vacuum permeability, M_S is the saturation magnetization, $\mathbf{H}_K$ is the anisotropy field and V is the volume of the FL. For a retention duration of >10 years, depending on the capacity of the memory device, the energy barrier should be 40–60 times larger than the thermal energy [47, 48].

What distinguishes various MRAM devices is the way the information in the MTJ is changed. Here, the focus shall lie on spin-transfer torque MRAM, spin-orbit torque MRAM and SOT-assisted STT-MRAM. These devices and their mode of operation will be explained in the following.

2.2 Spin-Transfer Torque MRAM

The mechanism for reversing the magnetization in a MTJ purely electrically by means of a spin-polarized current was predicted independently by Slonczewski [49] and Berger [50] in 1996. The general structure of an STT-MRAM cell can be seen in Fig. 2.4. The information-storing element is the previously introduced MTJ, which is sandwiched with a contact from both sides, both contacts being nonmagnetic. Altering the information in the MTJ is achieved by passing a current through the structure, either in the direction from FL to RL or from RL to FL, depending on the present state of the MTJ. The torque acting on the FL magnetization, the spin-transfer torque, is also what gives this type of MRAM cell its name.

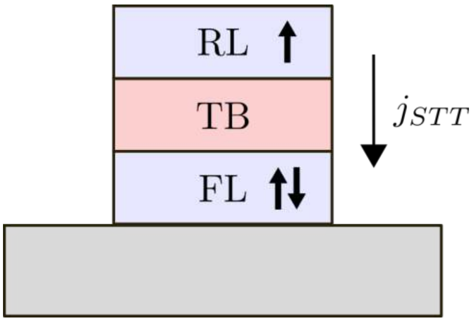

Figure 2.4: Typical structure of a spin-transfer torque MRAM cell. The path for the writing current j_{STT} is through the structure.

To change the configuration of the MTJ from an anti-parallel configuration to a parallel configuration, an electrical current is sent through the MTJ in the direction from the FL to the RL. With the electrons moving from the RL to the FL, the majority electrons are able to cross the RL, resulting in a spin-polarized current entering the FL. Due to exchange interaction with the magnetization in the FL, the spins of the electrons entering the FL become aligned with the magnetization of the FL within a short distance after entering. As the spin angular momentum is conserved, the transverse spin component of the electrons is transferred to the magnetization in the FL, which thus is tilted towards the RL magnetization's orientation. This transfer of the transverse component of the spin is the spin-transfer torque. When the current continues to be sent through the MTJ, the FL magnetization eventually fully aligns with the RL magnetization. If the two ferromagnetic layers are magnetized in a parallel configuration and a current is passed through the structure in the reverse direction, i.e. the electrons are entering on the FL side, the minority electrons are reflected back at the TB/RL interface into the FL. The transverse spin component of these reflected electrons is transferred onto the magnetization and the resulting torque can lead to switching of the magnetization if it is sufficiently large. As STT is proportional to the transverse spin component, there is no torque if the magnetization in the FL and RL are collinear. This results in the presence of an incubation delay when a write current pulse is applied. During this time period, no torque is acting, until a large enough thermal fluctuation deviates the FL magnetization from the equilibrium position. If the incubation delay exceeds the duration of the current pulse, a write error occurs [51, 52].

Initially, research on STT-MRAM cells was focussed on in-plane magnetic anisotropy (IMA) structures. These cells relied on shape anisotropy to fix the magnetization orientation and had to have elliptical or rectangular shape [53]. To provide the necessary thermal stability, IMA cells are limited to dimensions larger than 60 nm [31]. In IMA MTJ devices, the path of the magnetization during reversal does not coincide with the path of temperature-mediated switching of the FL magnetization. The reversal trajectory requires the magnetization to go out of plane [54].

The critical current density for IMA MTJ devices, i.e. the minimum current density required for the reversal of the free layer magnetization's orientation, is as follows [55–57]:

$$J_{c0\_IMA} = \alpha \frac{2e}{\hbar\eta}(\mu_0 M_S)(|\mathbf{H}_{\mathrm{ext}}| + |\mathbf{H}_{\mathrm{K}}| + \frac{|\mathbf{H}_{\mathrm{d}}|}{2})t_{FL} \tag{2.6}$$

α is the damping constant, e is the electron charge, $\hbar$ is Planck's constant, η is the spin-transfer efficiency, t_{FL} is the effective thickness of the FL, μ_0 is the vacuum permeability, M_S is the saturation magnetization, $\mathbf{H}_{\mathrm{ext}}$ is an external magnetic field, $\mathbf{H}_{\mathrm{K}}$ is the anisotropy field and $\mathbf{H}_{\mathrm{d}}$ is the demagnetizing field, a magnetic field that is caused by the long-range dipole-dipole interaction of the magnetic moments.

However, in order to be competitive with CMOS devices, structures needed to be scaled down which caused problems with in-plane magnetized structures, as the shape anisotropy was not sufficient anymore to ensure a high enough thermal energy barrier [57]. A second factor which encouraged a transition to perpendicular magnetic anisotropy (PMA) MTJs is that for switching in-plane magnetized memory devices, additionally to the anisotropy field $\mathbf{H}_{\mathrm{K}}$, also the demagnetizing field $\mathbf{H}_{\mathrm{d}}$ has to be overcome, a field which is a lot larger than the anisotropy field [56]. Without the need to surmount the demagnetizing field, the formula for the critical current density of PMA MTJs reduces to [46]:

$$J_{c0\_PMA} = \alpha \frac{e\gamma}{\mu_B \eta} M_S |\mathbf{H}_{\mathrm{K}}| t_{FL} \tag{2.7}$$

As the main contributors to PMA are interfacial anisotropy effects rather than shape anisotropy, memory cell structures can be manufactured with cylindrical shapes. Thus, PMA devices allow for better scaling and higher thermal stability, as well as lower switching currents and have become the most widely used type of magnetization configuration [58].

Looking at STT-MRAM from a more system-level perspective, a transistor is needed to access the memory cell, resulting in two-terminal MTJ, or often also called 1T-1MTJ. This single transistor then controls the current flow through the device which is needed for reading and writing the information in the cell. The fact that only a single transistor is required means that little cell area is consumed and allows for higher memory density. The two-terminal layout, however, results in limitations on the read and write current. If the read current is too high, unintentional magnetization reversal can occur [1], if the write current is too high, the tunnel barrier can be damaged [59, 60]. The next section will describe the working principles of spin-orbit torque (SOT) MRAM, a type of MRAM cell which eliminates the stress from high charge currents on the tunnel barrier during writing and allows for higher speed operation.

2.3 Spin-Orbit Torque MRAM

Spin-orbit torque MRAM is the second important representative of the MRAM family, and it distinguishes itself from STT-MRAM in the way the bit information in the MTJ is changed. Whereas for writing information in an STT-MRAM cell, a current is passed through the MTJ, in SOT-MRAM the current is passed through a heavy metal (HM) layer below the MTJ and thus does not flow through the MTJ, relieving the tunnel barrier (TB) from the stress caused by the STT write currents. In Fig. 2.5 a schematic depiction of an SOT-MRAM cell and the transverse spin current generated by the spin Hall effect (SHE) is shown. First publications presenting SOT-MRAM appeared in the years 2011 and 2012 [61, 62].

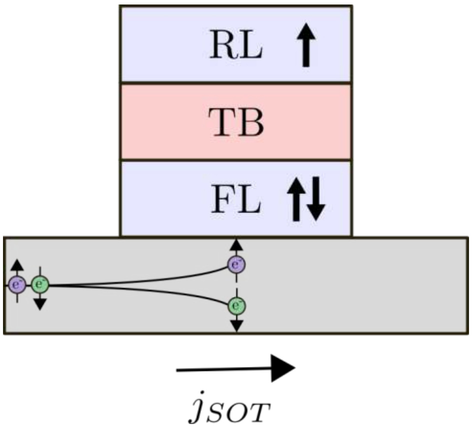

Figure 2.5: Typical structure of a three-terminal spin-orbit torque MRAM cell. The path for the writing current j_{SOT} is through the heavy metal contact attached to the FL.

There are two effects originating from spin-orbit interaction which lead to a SOT being exerted on the magnetization in the FL. The first effect which gives rise to SOT is the SHE, shown in Fig. 2.6b. The SHE transforms a charge current into a transverse spin current which, similarly to the spin-transfer torque (STT), exerts a torque on the magnetization due to the transfer of the spin angular momentum when penetrating the adjacent ferromagnetic FL. Typical heavy metals which exhibit a large spin Hall effect are Pt, Ta, and W [63]. The second effect, which is of interfacial origin, is the Rashba-Edelstein effect, shown in Fig. 2.6a [64, 65]. Typically, the electric field which induces the charge current, is applied perpendicular to the heavy metal/ferromagnet interface. Due to interfacial spin-orbit coupling, spin-dependent scattering of charge carriers occurs, resulting in a spin accumulation at the interface [64, 66–69]

The fact, that the torque-generating write current is not flowing through the MTJ in SOT-MRAM, but below it, greatly improves the endurance of the memory cell as the tunnel barrier is not degraded. However, two big challenges still have to be conquered. Due to the spin Hall angle not being large enough, the writing currents need to be rather large in order to get a sufficiently large SOT. By avoiding the direct path through the MTJ, however, higher current densities can be used, which also leads to faster magnetization reversal and switching times below one nanosecond can be achieved [1]. The second, bigger problem, however, with SOT-MRAM devices with perpendicular anisotropy is the vanishing torque once the magnetization is oriented in the plane. This is due to the fact that the SOT is proportional to $\mathbf{m}\times(\mathbf{n}\times\mathbf{E})$,

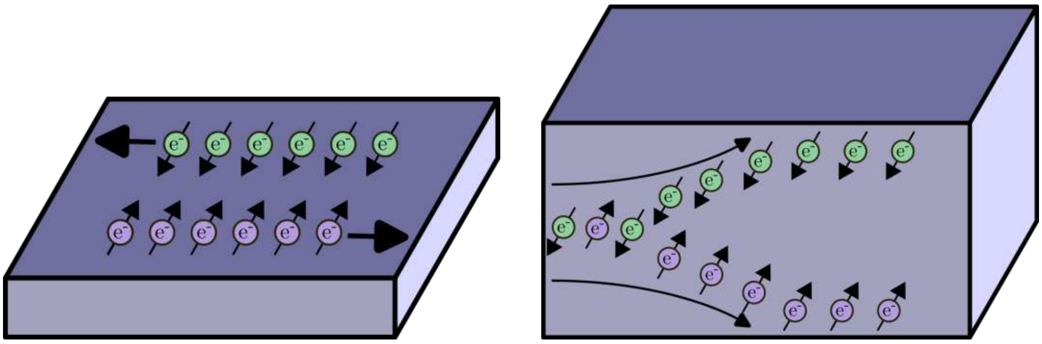

(a) (b)

Figure 2.6: Schematic depiction of (a) Rashba-Edelstein effect and (b) spin Hall effect.

with **n** being the unit normal vector of the HM/FM interface and **E** the direction of the electric field. Thus, the torque goes to zero once the magnetization is collinear with $\mathbf{n} \times \mathbf{E}$, which results in 50% probability of switching. Solving this problem requires to break the mirror symmetry with respect to the plane perpendicular to $\mathbf{n} \times \mathbf{E}$ [1]. Different approaches have been devised that circumvent the problem by applying an external magnetic field [70], structurally changing the symmetry [71, 72], introducing exchange bias by adding an antiferromagnetic layer [73, 74] or other structural changes to the memory cell [75]. However, these solutions often increase the complexity of the memory cell fabrication.

The critical current for switching a perpendicularly magnetized SOT-MRAM cell can be calculated using the following formula derived in [76]:

$$J_{\mathrm{c0}\_SHE} = \frac{2e}{\hbar}\frac{M_S t_F}{\theta_{SH}}\left(\frac{\mathbf{H}_{\mathrm{K}} - N_d M_S}{2} - \frac{\mathbf{H}_{\mathrm{x}}}{\sqrt{2}}\right) \tag{2.8}$$

t_F is the FL thickness, θ_{SH} is the spin Hall angle which measuers how efficient charge currents are converted to spin currents, N_d is the demagnetizing factor, which depends on the shape of the FL. This expression is valid for a perpendicular SOT-MRAM cell with an in-plane applied external field $\mathbf{H}_{\mathrm{x}}$ to ensure deterministic magnetization reversal.

An SOT-MRAM cell is a three-terminal device and requires two access transistors. This is referred to as 2T-1MTJ. Compared to the 1T-1MTJ structure of STT-MRAM devices, more chip area is consumed, resulting in a lower memory density. However, the 2T-1MTJ circuitry is similar in structure to 6T-SRAM typically employed in SRAM, and as the flip-flop circuitry can be exchanged with an MTJ, would work well as replacement of this type of cache memory [1]. In the following chapter, a promising solution to the existing challenges of SOT-MRAM combining STT and SOT will be described in detail.

2.4 SOT-Assisted STT-MRAM

As mentioned in the previous chapters, STT-MRAM exhibits some incubation time, limiting the maximum achievable switching time, and also requires the write current to be sent through the TB, which can potentially lead to oxide defects. In addition, read currents have to be chosen low enough, such that no erroneous writing of the FL occurs. Perpendicular SOT-MRAM on the other hand suffers from non-deterministic switching if no additional symmetry breaking measures are employed.

Only fairly recently, research has started to investigate memory cells in which the writing process uses a combination of STT and SOT [77,78]. The general idea of SOT-assisted STT-MRAM is to exploit both of these torque types in order to evade the shortcomings of pure STT- and SOT-MRAM cells, e.g. Fig. 2.7.

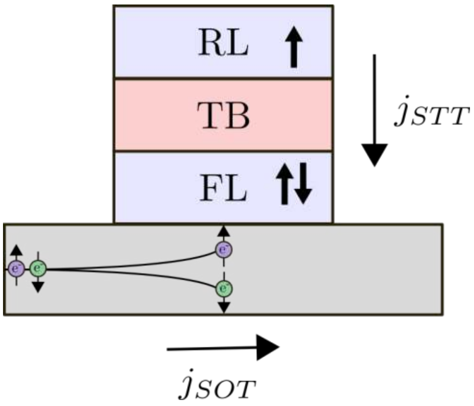

Figure 2.7: Structure of a three-terminal SOT-assisted STT-MRAM cell. The paths for the writing currents j_{STT} and j_{SOT} are through the MTJ and through the heavy metal contact attached to the FL, respectively.

The three-terminal architecture as described in Section 2.3 and depicted in Fig. 2.8a, due to its large footprint and the need for more than one transistor for the selection of the cell, renders this cell architecture less attractive for memory applications, a field where the density of the bits is of utmost importance. Especially, as currently employed technologies like DRAM and flash use a two-terminal architecture [79, 80].

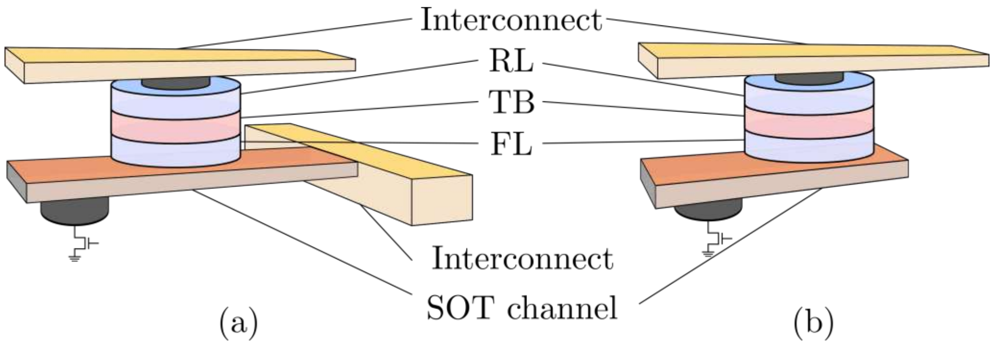

Figure 2.8: Depiction of a (a) three-terminal and a (b) two-terminal SOT-MRAM cell.

A two-terminal cell architecture as shown in Fig. 2.8b was first presented in 2013 [81]. This approach, however, loses the separation of the read and write path, as the write current always flows through the MTJ as well as the SOT channel. Eliminating the need for an additional transistor and combining STT and SOT promises lower critical currents, while reducing the switching times. While the initial investigations of SOT-assisted STT-MRAM were based on simulations, several publications presenting experimental results demonstrating the effect of combining STT and SOT were published in the last years [82–84].

Chapter 3

Micromagnetism

The origins of the theory of micromagnetism date back to the beginning of the second half of the 20^{th} century when William Fuller Brown Jr. coined the term *micromagnetism* [85]. Micromagnetism is often described as a semiclassical theory, as it combines classic field theory with approximate descriptions of quantum mechanical effects, like exchange interaction. Especially for the simulation of spintronic devices, the micromagnetic model renders itself to be useful, as purely macroscopic methods are not able to properly resolve the microscopic behavior, whereas the computational load of ab-initio methods is too high to simulate systems at the scale of spintronic devices.

There is a set of assumptions that underlie the micromagnetic model. The distribution of magnetic moments S_i is being approximated by a continuous vector density $\mathbf{M}(\mathbf{x})$. Neighboring magnetic moments S_i below the exchange length λ are coupled by exchange interaction, which leads to the moments favoring an aligned orientation. Approximating the moments' distribution as $\mathbf{m}(\mathbf{x})$ is thus valid when considering a region Ω larger than λ^3. This can be expressed with the following approximately true equation:

$$\sum_i S_i \approx \int_\Omega \mathbf{M}(\mathbf{x})\mathrm{d}\mathbf{x} \tag{3.1}$$

Another assumption in the micromagnetic model requires the magnetization $\mathbf{m}(\mathbf{x})$ to have constant norm:

$$\mathbf{M}(\mathbf{x}) = M_S \mathbf{m}(\mathbf{x}) \quad \text{with} \quad |\mathbf{m}(\mathbf{x})| = 1, \tag{3.2}$$

with $\mathbf{m}(\mathbf{x})$ thus being a unit vector field and M_S the saturation magnetization.

In the following, the governing equation in the field of micromagnetism is introduced with all its components used to describe the dynamic behavior of the magnetization in ferromagnetic systems.

3.1 Landau-Lifshitz-Gilbert Equation

The main equation describing the dynamics of the magnetization in micromagnetism was introduced in the first half of the 20^{th} century by Landau and Lifshitz [86]. This equation, however, suffered from being only applicable to low-damping scenarios, and was later ameliorated by Gilbert [23, 24]. Gilbert's form of the equation is commonly known as the Landau-Lifshitz-Gilbert (LLG) equation and looks as follows:

$$\partial_t \mathbf{m} = -\gamma_0 \left(\mathbf{m} \times \mathbf{H}_{\mathbf{eff}}\right) + \alpha \left(\mathbf{m} \times \partial_t \mathbf{m}\right) \tag{3.3}$$

Here, γ_0 is the rescaled gyromagnetic ratio, i.e. $\gamma_0 = -\gamma\mu_0$, with μ_0 being the vacuum permeability. α is the dimensionless Gilbert damping parameter. It has to be noted, though, that (3.3) is implicit, as the time derivative of the magnetization appears on both sides. However, by replacing the time derivative on the right-hand side with the equation itself, it can be rewritten in explicit form:

$$\partial_t \mathbf{m} = \underbrace{-\frac{\gamma_0}{1+\alpha^2}\left(\mathbf{m} \times \mathbf{H}_{\mathbf{eff}}\right)}_{precession} \underbrace{-\frac{\gamma_0 \alpha}{1+\alpha^2}\left(\mathbf{m} \times \left(\mathbf{m} \times \mathbf{H}_{\mathbf{eff}}\right)\right)}_{damping} \tag{3.4}$$

The first term on the right-hand side (3.4) is responsible for the description of the precessional motion of the magnetization and can be derived from classical mechanics [24]. The second term, which models the damping the magnetization undergoes, is purely phenomenological. Figure 3.1 shows trajectories of the magnetization under the influence of an effective magnetic field $\mathbf{H}_{\text{eff}}$ for precessional motion (a), damped motion (b) and damped precessional motion (c).

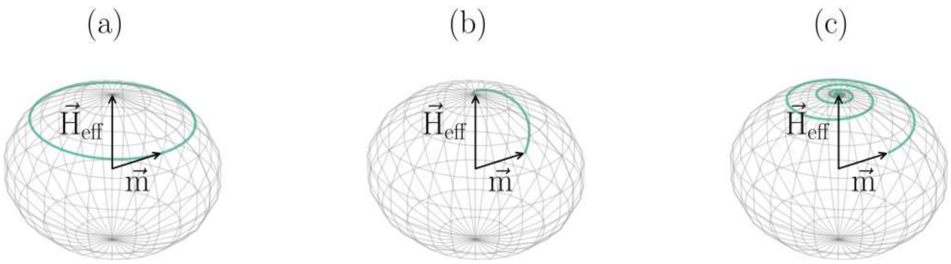

Figure 3.1: Magnetization trajectories for (a) precessional, (b) damped and (c) damped precessional configuration of the LLG.

3.2 Effective Magnetic Field

The total energy of a ferromagnet plays an important role in the dynamic behavior of the magnetization as the relation between the effective magnetic field used in the LLG equation and the total energy of the ferromagnetic system is defined as follows:

$$\mathbf{H}_{\text{eff}} = -\frac{1}{\mu_0 M_S}\frac{\delta E}{\delta \mathbf{m}} \tag{3.5}$$

It is the negative variational derivative of the Gibbs' free energy E with respect to the magnetization $\mathbf{m}$.

All the contributions to the effective magnetic field that were briefly introduced in the introductory part of this chapter shall be discussed in more detail in the following.

3.2.1 Exchange Field

Spontaneous magnetization which can be observed in ferromagnetic materials cannot be explained by classical electrodynamics, as it would predict a vanishing magnetization for a ferromagnetic system without external field [87].

However, due to the quantum mechanical effect of exchange interaction, two localized spins in ferromagnetic materials favor parallel alignment. The exchange energy is defined as

$$E_{ex} = \int_{\Omega_m} A \sum_{i,j} \left(\frac{\partial m_i}{\partial x_j} \right)^2 \mathrm{d}\mathbf{x} \tag{3.6}$$

$$= \int_{\Omega_m} A (\nabla \mathbf{m})^2 \mathrm{d}\mathbf{x} \tag{3.7}$$

Here, A is the exchange constant and $\sum_{i,j} \left(\frac{\partial m_i}{\partial x_j} \right)^2$ is a Frobenius inner product. The description of the exchange field, is given as

$$\mathbf{H}_{ex} = \frac{2A}{\mu_0 M_S} \nabla^2 \mathbf{m} \tag{3.8}$$

3.2.2 Anisotropy Field

Materials which exhibit anisotropic behavior possess one or more easy axes, preferred magnetization directions which minimize the magnetic free energy. Thus, for anisotropic materials the necessary work to change the orientation of the magnetization depends on the spatial distribution of the anisotropy characteristics. Ferromagnets exhibit anisotropic behavior from various origins. Anisotropic crystal structure (magnetocrystalline anisotropy), properties of the material interfaces (interface anisotropy), as well as the shape of the ferromagnetic system (shape anisotropy) can be the source for the direction-dependent behavior of the magnetization [88].

Uniaxial anisotropy

In the case of uniaxial anisotropy, the anisotropy energy can be written as

$$E_{ani,uni} = -\int_{\Omega_m} K_1(\mathbf{m}\cdot e)^2 \mathrm{d}\mathbf{x} \tag{3.9}$$

Here, K_1 is the material anisotropy constant and e is the unit vector pointing into the direction of the easy axis.

The uniaxial anisotropy field is given as

$$\mathbf{H}_{ani,uni} = \frac{2K_1}{\mu_0 M_S}\left(\mathbf{m}\cdot e\right) e \tag{3.10}$$

Cubic anisotropy

For materials exhibiting more than one easy axes, like iron which has cubic lattice symmetry, the anisotropy energy is

$$E_{ani,cubic} = \int_{\Omega_m} K_1\left(m_1^2 m_2^2 + m_2^2 m_3^2 + m_3^2 m_1^2\right) + K_2\left(m_1^2 m_2^2 m_3^2\right) \mathrm{d}\mathbf{x} \tag{3.11}$$

with m_i being the projections of the magnetization $\mathbf{m}$ onto the easy axes e_i and K_1 and K_2 being the material anisotropy constants for the cubic case.

$$\mathbf{H}_{ani,cubic} = -\frac{2D}{\mu_0 M_S}\mathbf{m} \tag{3.12}$$

with D being a matrix with the following structure [89]:

$$D = \begin{bmatrix} K_1\left(m_2^2 + m_3^2\right) + K_2 m_2^2 m_3^2 & 0 & 0 \\ 0 & K_1\left(m_1^2 + m_3^2\right) + K_2 m_1^2 m_3^2 & 0 \\ 0 & 0 & K_1\left(m_1^2 + m_2^2\right) + K_2 m_1^2 m_2^2 \end{bmatrix}$$

3.2.3 Demagnetizing Field

An important contribution to the effective magnetic field stems from the demagnetizing field, which originates from the long-range dipole-dipole interaction of the magnetic moments. As its name suggests, it energetically prefers a state with a reduced total magnetic moment. The demagnetizing energy is given as

$$\mathbf{E}_d = -\frac{\mu_0 M_S}{2} \int_\Omega \mathbf{m} \cdot \mathbf{H}_\mathrm{d} \mathrm{d}\mathbf{x} \tag{3.13}$$

with the factor $\frac{1}{2}$ preventing to count the self-interaction twice. In a current-free system, a description for the demagnetizing field can be derived from Maxwell's equations as follows:

$$\nabla \cdot \mathbf{B} \quad = 0 \tag{3.14}$$

$$\nabla \times \mathbf{H}_\mathrm{d} = 0 \tag{3.15}$$

According to (3.15), the demagnetizing field $\mathbf{H}_\mathrm{d}$ is conservative and can be expressed as

$$\mathbf{H}_\mathrm{d} = -\nabla u \tag{3.16}$$

By replacing the magnetic flux $\mathbf{B}$ with

$$\mathbf{B} = \mu_0 \left(\mathbf{H}_\mathrm{d} + M_S \mathbf{m} \right) \tag{3.17}$$

we arrive at the following expression for the scalar magnetic potential u

$$\nabla \cdot (-\nabla u + M_S \mathbf{m}) = 0 \tag{3.18a}$$

$$\Delta u = \nabla \cdot M_S \mathbf{m} \tag{3.18b}$$

The boundary condition for this equation is given asymptotically:

$$u(\mathbf{x}) = \mathcal{O}(\frac{1}{|\mathbf{x}|}) \quad for\ |\mathbf{x}| \rightarrow \infty \tag{3.19}$$

(3.19) states that the scalar magnetic potential decays to zero only at infinity. Such types of boundary conditions are called open boundary conditions.

Similar to the electric field, magnetic volume charges (ρ_m) and magnetic surface charges (σ_m) can be defined:

$$\rho_m = -\nabla \cdot M_S \mathbf{m} \tag{3.20}$$

$$\sigma_m = M_S \mathbf{m} \cdot \mathbf{n} \tag{3.21}$$

The component of $\mathbf{H}_\mathrm{d}$ parallel to the surface as well as the component $\mathbf{B}$ perpendicular to the surface are required to be continuous, which is described by the following equations:

$$u^{in} = u^{out} \tag{3.22}$$

$$(\nabla u^{in} - \nabla u^{out}) \cdot \mathbf{n} = \sigma_m \tag{3.23}$$

These auxiliary quantities can be used to write the magnetic potential as

$$u(\mathbf{x}) = \frac{1}{4\pi\mu_0}\left[\int_\Omega \frac{\rho_m(\mathbf{x}')}{|\mathbf{x}-\mathbf{x}'|}\mathrm{d}\mathbf{x}' + \int_{\partial\Omega} \frac{\sigma_m(\mathbf{x}')}{|\mathbf{x}-\mathbf{x}'|}\mathrm{d}\mathbf{s}'\right] \tag{3.24}$$

3.2.4 Ampere Field

The so-called Ampere field contribution to the effective magnetic field is generated when a current is flowing through the magnetic regions of an MRAM device.

The Ampere field $\mathbf{H}_\mathrm{curr}$ can be calculated by Bio-Savart's law from the current density $\mathbf{J}_C$:

$$\mathbf{H}_\mathrm{curr} = \frac{1}{4\pi}\int_\Omega \mathbf{J}_C \times \frac{(\mathbf{x}-\mathbf{x}')}{|\mathbf{x}-\mathbf{x}'|^3}\,\mathrm{d}\mathbf{x}' \tag{3.25}$$

3.2.5 Thermal Field

The influence of thermal effects on the magnetization dynamics can be described by a randomly varying contribution to the effective magnetic field. However, these thermal field contributions have to exhibit the following properties [90, 91]:

$$\langle H_{th}^{i}(t)\rangle = 0 \tag{3.26a}$$

$$\langle H_{th}^{i}(t), H_{th}^{j}(t')\rangle = D\,\delta_{ij}\,\delta(t-t') \tag{3.26b}$$

i and j are Cartesian indices, $\langle\cdot\rangle$ describes the average over several simulated realizations, δ_{ij} and $\delta(t-t')$ are the Kronecker delta function and the Dirac delta function, respectively. D is a constant measuring the strength of the thermal fluctuations and is a result from the Fokker-Planck equation [92]. Thus, Eq. (3.26) describes a field which is uncorrelated in time and space.

3.3 Modeling Spin Torque

A model commonly used to describe the torque in STT-MRAM devices is the macrospin model by Slonczewski [93]. Here, the dynamics of the free layer (FL) magnetization are described as behaving like a single spin which is influenced by the polarization occurring in a polarizing layer. The Landau-Lifshitz-Gilbert (LLG) extended by such a torque term takes the following form

$$\frac{\partial \mathbf{m}}{\partial t} = -\gamma_0 \mathbf{m}\times\mathbf{H}_{\text{eff}} + \alpha\mathbf{m}\times\frac{\partial \mathbf{m}}{\partial t} + \frac{1}{M_s}\mathbf{T}_S \tag{3.27}$$

with $\mathbf{T}_S$ being the spin torque originating from the angular momentum which is transferred from the electrons which are spin-polarized in the polarizing layer.

The spin torque $\mathbf{T}_S$ can be written in terms of a damping-like component, which moves the FL magnetization towards the axis of the RL's magnetization, and a field-like component, which makes the FL magnetization precess around the direction of the RL magnetization [94, 95]:

$$\mathbf{T}_S = \underbrace{a\mathbf{m} \times (\mathbf{m} \times \mathbf{p})}_{\text{damping}-\text{like}} + \underbrace{b(\mathbf{m} \times \mathbf{p})}_{\text{field}-\text{like}} . \tag{3.28}$$

The parameters a and b are dependent on the current density and $\mathbf{p}$ is the orientation of the magnetization in the reference layer (RL). Based on the torque expression in Eq. (3.28), the LLG in Eq. (3.27) can be rewritten as

$$\begin{aligned}\partial_t \mathbf{m} = \frac{1}{1+\alpha^2}\Big[&- \gamma_0 \left(\mathbf{m} \times \mathbf{H}_{\text{eff}}\right) - \gamma_0 \alpha \left(\mathbf{m} \times \left(\mathbf{m} \times \mathbf{H}_{\text{eff}}\right)\right) \\ &- \frac{\gamma \hbar J_C}{e M_S d_{FL}} \eta(\theta) \left[\mathbf{m} \times (\mathbf{m} \times \mathbf{p}) - \beta(\mathbf{m} \times \mathbf{p})\right]\Big]\end{aligned} \tag{3.29}$$

J_C is the modulus of the current density, d_{FL} is the thickness of the FL, the coefficient β describes the strength of the field-like torque, $\eta(\theta)$ describes the torque efficiency, which can be expressed differently, depending on whether a spin-valve or a MTJ is being described [49, 96]. The Slonczewski model is is often used when simulating STT-MRAM devices. As the reference layer is fixed, it is sufficient to simulate the dynamics of the FL magnetization. However, the fact that the FL dynamics are modeled as a single spin restricts the model's applicability. Only small systems can be simulated accurately, where the exchange interaction is most dominant and the magnetization acts nearly uniformly. To improve on this, extensions can be made to the model, such that $\mathbf{m}$ as well as $\mathbf{p}$ are functions of the lateral dimension of the FL. However, the Slonczewski model given in Eq. (3.29) disregards spin polarization diffusion to a certain degree, which is only valid for specific material systems and magnetization configurations [97]. Considering a torque expression based on the spin accumulation $\mathbf{S}$ results in a more general approach. The spin accumulation is a vector field which describes the difference of the conducting electrons' polarization in comparison to the equilibrium. A torque term employing $\mathbf{S}$ can be written as [98–101]:

$$\mathbf{T}_S = -D_e \frac{\mathbf{m} \times \mathbf{S}}{\lambda_J^2} - D_e \frac{\mathbf{m} \times (\mathbf{m} \times \mathbf{S})}{\lambda_\varphi^2} \tag{3.30}$$

Here, D_e is the electron diffusion coefficient, λ_J is the exchange length and λ_φ is the spin dephasing length. The first term in Eq. (3.30) characterizes the precession of the spins entering the FL in the exchange magnetic field of the FL magnetization, while the second term models the dephasing of the spins of the electrons flowing through the device. The steady-state ($\frac{\partial \mathbf{S}}{\partial t} = 0$) spin accumulation can be obtained by solving the following equation [102]:

$$\frac{\partial \mathbf{S}}{\partial t} = 0 = -\nabla \cdot J_{\mathbf{S}} - D_e \left(\frac{\mathbf{S}}{\lambda_{sf}^2} + \frac{\mathbf{S} \times \mathbf{m}}{\lambda_J^2} + \frac{\mathbf{m} \times (\mathbf{S} \times \mathbf{m})}{\lambda_\varphi^2} \right) \tag{3.31}$$

λ_{sf} is the spin-flip length, and $J_{\mathbf{S}}$ is the spin current. In the FEM simulator developed and implemented in this work, the spin and charge drift-diffusion formalism is used for the computation of the spin accumulation $\mathbf{S}$ in the non-magnetic and ferromagnetic layers [103]. An extensive discussion of the spin and charge drift-diffusion formalism for the simulation of STT-MRAM devices was carried out by Fiorentini [104]. Equation (3.30), however, not only allows the simulation of STT, but can also be used to take spin-orbit coupling effects into account and thus simulate torques in SOT-MRAM devices, as was shown by e.g. Lepadatu [98] and Jørstad *et al.* [105].

Chapter 4

Computational Methods

For micromagnetic simulations, the most popular discretization methods are the finite difference method (FDM) and the finite element method (FEM). Commercial and open source codes can be found, which can be used to simulate the magnetization dynamics. Recently, also machine learning (ML) approaches were introduced to tackle problems in micromagnetic simulations. In the following, these methods will be introduced, beginning with time integration methods, which are of utmost importance when performing simulations of the magnetization dynamics in MRAM devices.

4.1 Time Integration

For the simulation of dynamic micromagnetics, like switching of MRAM devices or the simulation of hysteresis in a ferromagnetic system, the LLG equation needs to be solved over multiple time steps. While both the FDM and the FEM are commonly used in micromagnetics for the spatial discretization of the computational domain, separate time integration algorithms are employed for the discretization in time. The LLG equation belongs to the class of stiff differential equations. For stiff equations, when solved numerically, the time step is dictated by stability rather than the required accuracy [106]. Thus, due to the stiffness of the LLG equation, which mainly arises due the exchange coupling, a good choice of the used algorithm can save oneself from having to use unnecessarily small time steps and thus suffering from long simulation running times [106–109]. Besides its stiffness, there is also the constraint that the modulus of the magnetization needs to be preserved over time for every magnetization vector in the computational domain. Some numerical schemes do not inherently fulfill this requirement, others project the magnetization back onto the unit sphere, and some schemes are designed such that the modulus is preserved automatically [97, 110].

In the following, an overview of some of the most often used time integration schemes will be presented. For the description of the schemes, we will make use of the following notation for the values of the magnetization over time:

$$\mathbf{m}_i \approx \mathbf{m}(t_i) \quad \text{with} \quad t_i = t_0 + i\Delta t \tag{4.1}$$

4.1.1 Explicit Runge-Kutta Methods

One of the most widely used iterative solvers for time discretization is the family of Runge-Kutta algorithms.

$$\frac{d\mathbf{m}}{dt} = f(t, \mathbf{m}) \tag{4.2}$$

$$\mathbf{m}_{n+1} = \mathbf{m}_n + h \sum_{j=1}^{s} b_j k_j \tag{4.3}$$

Here, s defines the number of stages of the specific Runge-Kutta algorithm, b_j are coefficients defining a specific Runge-Kutta method, and the k_j are evaluations of $f(t, \mathbf{m})$ at intermediate points between the current and the next time step.

$$\begin{aligned}
k_1 &= f\left(t_n, \mathbf{m}\right) \\
k_2 &= f\left(t_n + c_2 h, \mathbf{m} + (a_{21} k_1) h\right), \\
k_3 &= f\left(t_n + c_3 h, \mathbf{m} + (a_{31} k_1 + a_{32} k_2) h\right), \\
&\ \vdots \\
k_s &= f\left(t_n + c_s h, \mathbf{m} + (a_{s1} k_1 + a_{s2} k_2 + \cdots + a_{s,s-1} k_{s-1}) h\right)
\end{aligned}$$

Here, a_{ij} and c_j, like b_j, are coefficients whose choice characterizes a particular Runge-Kutta variant. One can see that the subsequent evaluations of k_j always only depend on a previously calculated k_j, which makes the method explicit.

In general, however, it is known that explicit methods are not the best choice for stiff problems. In order to achieve a desirable accuracy, one potentially has to resort to a very small time step, rendering these methods not practical [110]. In conjunction with finite-difference methods, the Runge-Kutta scheme nevertheless is commonly used, as it was shown in [111], when using a regular grid, the size of the time step is not restricted by the space discretization size anymore.

4.1.2 Implicit Midpoint Scheme

The implicit midpoint scheme makes use of the implicit midpoint rule, and it was shown in [112] that it preserves the unit sphere constraint. In this scheme, the next magnetization value is calculated as

$$\mathbf{m}_{n+1} = \mathbf{m}_n + \Delta t \partial_t \mathbf{m} \left[t_n + \frac{\Delta t}{2}, \frac{\mathbf{m}_{n+1} + \mathbf{m}_n}{2} \right] \tag{4.4}$$

which, by using the right-hand side of (3.3) and replacing $\partial_t \mathbf{m} = (\mathbf{m}_{n+1} - \mathbf{m}_n)/\Delta t$, leads to

$$\begin{aligned} \mathbf{m}_{n+1} =& \mathbf{m}_n + \Delta t \frac{\mathbf{m}_{n+1} + \mathbf{m}_n}{2} \\ & \times \left(-\gamma \mathbf{H}_{\text{eff}} \left[t_n + \frac{\Delta t}{2}, \frac{\mathbf{m}_{n+1} + \mathbf{m}_n}{2} \right] + \alpha \frac{\mathbf{m}_{n+1} - \mathbf{m}_n}{\Delta t} \right) \end{aligned} \tag{4.5}$$

According to [112], this scheme is flexible in the spatial discretization scheme used and can be applied to FDM as well as FEM. Due to the implicitness of this scheme, it is unconditionally stable. Thus, the choice of time-step is not dictated by stability and the largest time-step which still meets the accuracy demands can be chosen.

4.1.3 Tangent-Plane Integration

The tangent-plane integration scheme - first introduced in [113] and later generalized in [114] - is the time integration scheme used for the dynamic micromagnetic FEM simulations performed in this work. Thus, its description will be more detailed.

This scheme is based on a form of the LLG equation, which results from cross-multiplying (3.3) with $\mathbf{m}$:

$$\alpha\frac{\partial\mathbf{m}}{\partial t}+\mathbf{m}\times\frac{\partial\mathbf{m}}{\partial t}=\gamma_0\mathbf{H}_{\text{eff}}-\gamma_0(\mathbf{m}\cdot\mathbf{H}_{\text{eff}})\mathbf{m} \tag{4.6}$$

The time derivative of $\mathbf{m}$, which is the quantity that we solve for, is replaced by

$$\mathbf{v}=\partial_t\mathbf{m} \tag{4.7}$$

The property that gives this method its name is the fact that the space of solutions is defined as

$$V_T=\{\mathbf{v}:\mathbf{v}\cdot\mathbf{m}=0\} \tag{4.8}$$

and is thus restricted to the tangent space of $\mathbf{m}$. Using (4.7), the weak formulation for (4.6) can be written as

$$\int_\Omega(\alpha\mathbf{v}+\mathbf{m}\times\mathbf{v})\cdot\mathbf{w}\ \mathrm{d}\mathbf{x}=\gamma_0\int_\Omega\mathbf{H}_{\text{eff}}(\mathbf{m})\cdot\mathbf{w}\ \mathrm{d}\mathbf{x},\quad\forall\ \mathbf{w}\ \epsilon\ V_T \tag{4.9}$$

This scheme can subsequently be transformed into an implicit θ-scheme by inserting $\mathbf{m}_n+\theta\Delta t\mathbf{v}$ for $\mathbf{m}$. To obtain a stable numerical scheme, it is sufficient to treat the exchange field implicitly [114]. Thus, the exchange field is the only effective field contribution which is treated implicitly in this work:

$$\int_\Omega(\alpha\mathbf{v}+\mathbf{m}_nk\times\mathbf{v})\cdot\mathbf{w}\ \mathrm{d}\mathbf{x}+\theta\frac{2A_{ex}\gamma}{M_S}\Delta t\int_\Omega\nabla\mathbf{v}:\nabla\mathbf{w}\ \mathrm{d}\mathbf{x} \tag{4.10}$$

$$=\gamma\mu_0\int_\Omega\mathbf{H}'_{\text{eff}}\cdot\mathbf{w}\ \mathrm{d}\mathbf{x}-\frac{2A_{ex}\gamma}{M_S}\int_\Omega\nabla\mathbf{m}_n:\nabla\mathbf{w}\ \mathrm{d}\mathbf{x}$$

Here, $\mathbf{H}'_{\text{eff}}$ contains all the effective field terms apart from the exchange field and $\nabla\mathbf{a} : \nabla\mathbf{b} = \sum_{ij}(\partial a_i/\partial x_j)(\partial b_i/\partial x_j)$ is the Frobenius inner product of the two matrices $\mathbf{a}$ and $\mathbf{b}$. By choosing $0 \leq \theta \leq 1$, the degree to which the scheme is explicit or implicit can be adjusted: a completely explicit scheme result from setting $\theta = 0$ and a completely implicit scheme from setting it to $\theta = 1$. For stability reasons, the value of θ is set to 1 [115]. $\mathbf{m}_n$ in (4.10) is the magnetization at $t = n\Delta t$, where $n = 0, 1, 2, \ldots$ is the time step and Δt is the time step size. The magnetization at the next time step $n + 1$ is given by

$$\mathbf{m}_{n+1} = \frac{\mathbf{m}_n + \Delta t\,\mathbf{v}}{|\mathbf{m}_n + \Delta t\,\mathbf{v}|}. \tag{4.11}$$

where this calculation is performed for each node of the mesh.

In a FEM setting, the tangent constraint on the test function space given in (4.8) can be realized by using the following Lagrange multiplier ansatz to solve the resulting saddle-point problem [116, 117]

$$\begin{pmatrix} A & B^T \\ B & 0 \end{pmatrix} \begin{pmatrix} \mathbf{v} \\ \lambda \end{pmatrix} = \begin{pmatrix} f \\ 0 \end{pmatrix} \tag{4.12}$$

where $A \in \mathbb{R}^{3N\times 3N}$ is the discretized left-hand side of (4.10), $B \in \mathbb{R}^{3N\times 3N}$ comes from the constraint, $f \in \mathbb{R}^{3N}$ is the discretized right-hand side of (4.10) and the Lagrange multiplier $\lambda \in \mathbb{R}^{3N}$ is a scalar field. $B\mathbf{v} = 0$ enforces the constraint (4.8). A more detailed description of the Lagrange multiplier ansatz can be found in Abert *et al.* [116].

4.2 Finite Difference Method

The Finite Difference Method (FDM) is a cornerstone in the realm of numerical techniques, and provides a robust framework for approximating solutions to a diverse array of differential equations. Due to its simplicity, both with respect to the underlying mathematics, but also its implementation in code, FDM has become an indispensable tool across scientific disciplines. As it is so wide-spread, many introductory textbooks have been written about it, e.g. [118, 119].

At its core, the FDM operates on the principle of converting continuous differential equations into manageable discrete algebraic equations which allow for efficient computer-based computations that yield approximations closely resembling the behavior of the original continuous system.

The method achieves this by dividing the spatial and temporal dimensions of a problem into a grid of discrete points. A two-dimensional domain Ω is discretized into a set of grid points $\{x_{i,j}\}$ as

$$x_{i,j} = (ih,\ jh), \quad \text{with } i,\ j = 0,\ 1,\ \dots\ ,\ N \tag{4.13}$$

Which describes an equidistant grid with a spatial discretization width $h := 1/N$ with $N \in \mathbb{N}$ and N being the number of discretization points along the grid axes, as depicted in Section 4.2.

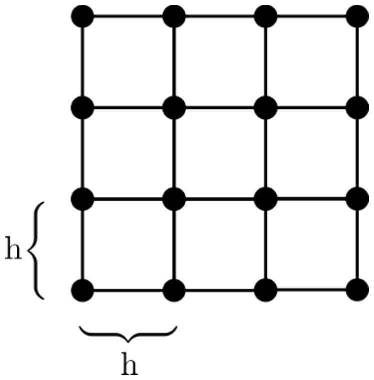

Figure 4.1: Equidistant grid with space discretization length h.

An example of a regular cuboid grid discretization of a unit sphere is shown in Fig. 4.2. It is apparent that this type of discretization is most suitable for rectangular geometries. For achieving good approximations of complex geometries, the grid needs to be refined, which can lead to a high computational cost [118].

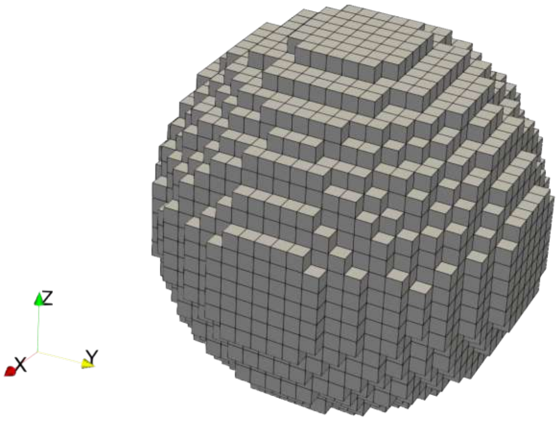

Figure 4.2: Regular cuboid grid discretization of a unit sphere.

The representation of the solution function on this grid is called grid function and the derivatives within the differential equation are approximated by replacing them with a finite difference quotient of grid function values at specific grid points.

The Poisson equation, which appears in many science and engineering applications, shall serve as an example of how differential equations are solved using the FDM. It is defined as:

$$-\nabla^2 u(x) = f(x), \qquad x \,\epsilon\, \Omega \tag{4.14a}$$

$$u(x) = u_D(x), \qquad x \,\epsilon\, \partial\Omega \tag{4.14b}$$

As already stated, in the FDM differential operators are approximated by finite difference quotients. The Laplace operator on the left-hand side of (4.14) can be discretized using the commonly employed quotient

$$\frac{\partial^2}{\partial x^2} u(x_i) \approx \frac{u_{i+1} - 2u_i + u_{i-1}}{h^2} \tag{4.15}$$

To evaluate this difference quotient for the nodes u_0 and u_N, however, it is necessary to apply a mathematical trick, as nodal values u_{-1} and u_{N+1} would be required. Adding additional nodes to the computational grid for these border cases allows the evaluation of the difference quotient. These additional nodes are called ghost points, as they are not part of the actual computational domain. The values of the ghost points are set to be [119]:

$$u_{-1} = u_1 \quad \text{and} \quad u_{N+1} = u_{N-1} \tag{4.16}$$

This ensures that the difference quotient can be evaluated correctly for the whole computational grid. By using the discretized version of the Laplace operator from (4.15) and replacing the right-hand side of (4.14) with the discrete version f_i, one gets the Poisson difference equation:

$$-\frac{u_{i+1} - 2u_i + u_{i-1}}{h^2} = f_i \tag{4.17}$$

Equation (4.17) can subsequently be reformulated in matrix form:

$$Au = r \tag{4.18}$$

The Dirichlet boundary condition given in (4.14b) can be incorporated into the discrete system of equations by setting the value of the respective boundary nodes to the Dirichlet values. This ensures that the solution satisfies the boundary conditions. Rearranging (4.18), one arrives at:

$$u = A^{-1}r \tag{4.19}$$

Consequently, the complex mathematical challenge of solving differential equations is distilled into solving a system of linear equations - a task many libraries exist for and can do efficiently.

4.2.1 Discretization of the LLG Equation

For the FDM-based simulations in this work, a code initially introduced in [120] was used. Figure 4.3 presents the program flow of this simulation tool. The general overall structure of the program follows a fairly common scheme. After an initialization phase, in which the simulation is started and parametrized through either a command line interface or a configuration file, the magnetostatic coupling between reference layer and free layer ($\mathbf{H}_{ms}$) and the field created from currents flowing through the device ($\mathbf{H}_{curr}$) are computed. This is followed by the time integration loop.

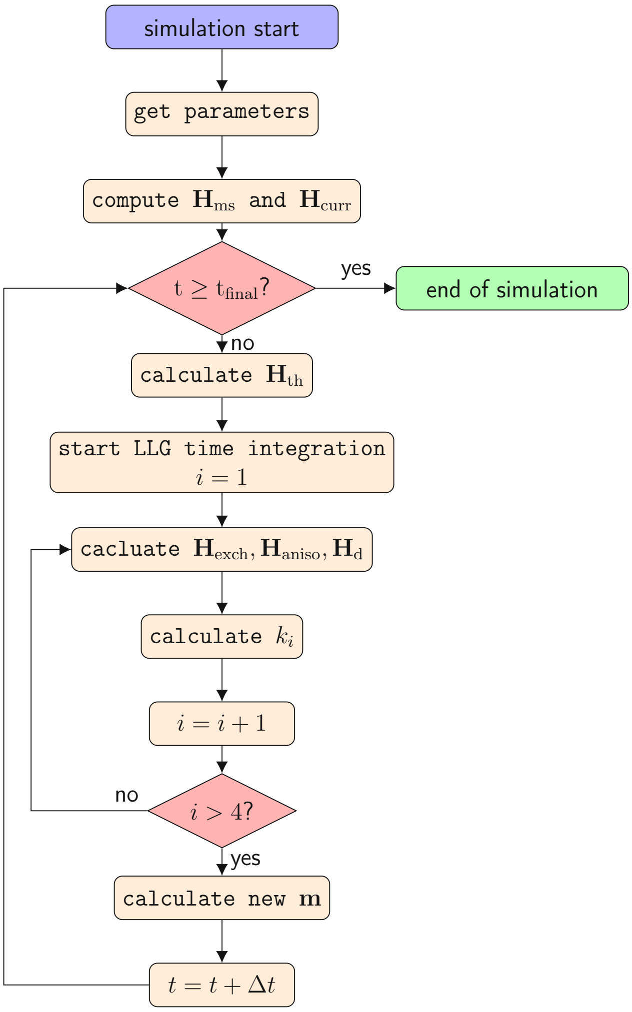

Figure 4.3: Flow chart of the general sequence of operations performed in the micromagnetic FDM simulator.

The innermost loop implements a fourth order Runge-Kutta time integration, each iteration computing one of the four coefficients k_i, according to:

$$k_1 = LLG(\mathbf{m}_n, \qquad t_n)\Delta t \tag{4.20a}$$
$$k_2 = LLG(\mathbf{m}_n + \frac{k_1}{2}, t_n + \frac{\Delta t}{2})\Delta t \tag{4.20b}$$
$$k_3 = LLG(\mathbf{m}_n + \frac{k_2}{2}, t_n + \frac{\Delta t}{2})\Delta t \tag{4.20c}$$
$$k_4 = LLG(\mathbf{m}_n + k_3, \; t_n + \Delta t)\Delta t \tag{4.20d}$$

Using these coefficients, the overall update to the magnetization is calculated as

$$\mathbf{m}_{n+1} = \mathbf{m}_n + (k_1 + 2k_2 + 2k_3 + k_4)\frac{\Delta t}{6}. \tag{4.21}$$

4.2.2 Effective Field Discretization

In the following, the finite difference discretization of the effective field contributions used within this code will be presented.

External Field

The external magnetic field is simply a configurable input function, which is defined at very computational node:

$$\mathbf{H}_{\text{ext}}(i, j, k) = \mathbf{H}_{\text{ext,input}} \tag{4.22}$$

Exchange Field

In order to calculate the exchange field, the nearest neighbors of each cell need to be known. In a regular FDM grid, these are in general the six cells with which the currently considered cell shares its cell faces.

$$\mathbf{H}_{\text{exch}}(i, j, k) = \frac{2A}{\mu_0 M_S} \sum_{i',\, j',\, k'} \frac{\mathbf{m}(i', j', k') - \mathbf{m}(i, j, k)}{d(\mathbf{m}', \mathbf{m})^2} \tag{4.23}$$

The nearest neighbors of the currently considered cell with the coordinate triplet $(i,\ j,\ k)$ are located at the position $i',\ j',\ k'$. The 6 neighboring cells have the coordinates $(i \pm 1,\ j,\ k)$, $(i,\ j \pm 1,\ k)$ and $(i,\ j,\ k \pm 1)$. $d(\mathbf{m}', \mathbf{m})$ calculates the distances between the vector components of $\mathbf{m}'$ and $\mathbf{m}$, i.e. $(\Delta x, \Delta y, \Delta z)^T$. At the boundary of the computational domain, there are obviously no six neighbors anymore, and a so-called "ghost" magnetic vector is used if no nearest neighbor is available. This vector's value corresponds to the closest magnetic vector at the boundary. The term "ghost" is used, as these ghost cells are not part of the computational domain, but are a mathematical construct that allows the evaluation of the exchange field at the boundary [119].

Anisotropy Field

To calculate the anisotropy field acting in a cell with coordinates (i, j, k), only this specific cell is considered. Thus, it is straightforward to translate (3.10) into its numerical equivalent:

$$\mathbf{H}_{\mathrm{K}}(i, j, k) = \frac{2K_1}{\mu_0 M_S}(\mathbf{m}(i, j, k) \cdot e)e \tag{4.24}$$

The same hold for the cubic anisotropy introduced in (3.12):

$$\mathbf{H}_{\mathrm{K}}(i, j, k) = -\frac{2D(i, j, k)}{\mu_0 M_S}\mathbf{m}(i, j, k) \tag{4.25}$$

with $D(i, j, k)$ being the matrix introduced in Section 3.2.2.

Demagnetizing Field

The demagnetizing field is the computationally most demanding effective field contribution, as it originates from the long-range interaction of the dipoles. Compared to the exchange field, for an accurate calculation of this field contribution it is thus not enough to only consider nearest neighbor cells. Instead, all the cells of the magnetic domains have to be considered.

$$\mathbf{H}_{\mathrm{d}}(i, j, j) = \frac{M_S}{4} \sum_{i'=1}^{N_x} \sum_{j'=1}^{N_y} \sum_{k'=1}^{N_z} (\tilde{G}(i, j, k, i', j', k') \cdot \mathbf{m}(i', j', k')) \tag{4.26}$$

The space-dependent matrix $\tilde{G}$ is formed from coefficients which describe the dipole-dipole interaction. As this interaction is long-ranged, all other magnetic moments have to be taken into account for determining the influence of the demagnetizing field in a specific cell. Thus, the computation of $\tilde{G}$ is computationally expensive. However, it can be precomputed once at the beginning of the simulation, as it only depends on the geometry of the magnetic domain and not on time. N_x, N_y and N_z are the number of computational nodes in the x, y and z direction, respectively.

Ampere Field

The discretized version of equation (3.25) to evaluate $\mathbf{H}_{\text{curr}}$ for a specific cell located at position (i, j, k) reads as

$$\mathbf{H}_{\text{curr}} = \frac{1}{4\pi} \sum_{i'}^{N_x} \sum_{j'}^{N_y} \sum_{k'}^{N_z} (\mathbf{J}_C(i', j', k') \times G'(i, j, k, i', j', k')) \tag{4.27}$$

The three nested summations go through all the cells apart from the cell for which the field is calculated $(i' \neq i,\ j' \neq j,\ k' \neq k)$. G' is a space-dependent vector which contains coefficients describing the interaction between the cells. Its derivation can be found in [121] along with the fast computation of the integrals it is based on.

Thermal Field

Following the requirement for the thermal field given in (3.26), the thermal field needs to be uncorrelated in space as well as time and can be calculated as

$$\mathbf{H}_{\text{th,(x,y,z)}} = \sigma(i, j, k) \sqrt{\frac{\alpha}{1 + \alpha^2} \frac{2 k_B T}{\gamma_0 \Delta t \Delta V M_S}} \tag{4.28}$$

The function σ returns a value from a Gaussian distribution which follows the requirements given in (3.26) and has a standard deviation of 1. ΔV is the volume of a single computational cell, Δt is the time step and T is the temperature.

4.3 Finite Element Method

Like the FDM, the FEM is a computational method to solve partial differential equations (PDE). However, the FEM is far more flexible with respect to the computational domain. In the following, the FEM will be introduced by going through the steps necessary to solve a PDE.

4.3.1 Discretization

Compared to the FDM, the FEM allows for the simulation of more complex structures, as in the three-dimensional case the computational domain is - most commonly - discretized into a mesh consisting of tetrahedral elements of finite extent, hence its name. These elements consist of nodes connecting which are shared by neighboring elements. The computational domain Ω thus consists of the union of the element domains Ω_e:

$$\Omega = \cup_e \Omega_e \tag{4.29}$$

Figure 4.4 shows an example of a unit sphere discretized into tetrahedral elements. Compared to the FDM discretization presented in Fig. 4.2, a smoother surface can be achieved while requiring $\sim 1/3$ of the number of surface nodes.

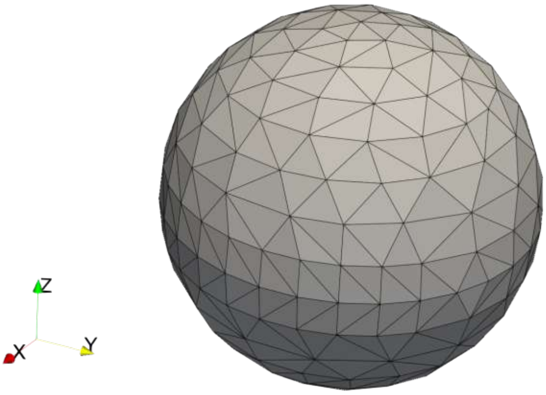

Figure 4.4: Tetrahedral discretization of a unit sphere.

In order to arrive at a computational method to solve a given PDE on a specific domain Ω, the FEM relies on two pillars. First, the representation of the solution of the PDE as a polynomial expression and, secondly, expressing the PDE as a variational formulation which allows to transform it into a computational stencil and eventually into a sparse linear system which can then be solved.

Again, the Poisson equation, given as

$$-\nabla^2 u(x) = f(x), \qquad x \,\epsilon\, \Omega \tag{4.30a}$$

$$u(x) = u_D(x), \quad x \,\epsilon\, \partial\Omega \tag{4.30b}$$

shall serve as exemplary problem to introduce the approach to transfer a problem into its weak formulation. Here, u is the solution of an unknown function, $f(x)$ is a source function. The problem at hand is a boundary value problem as (4.30b) predetermines the value of the solution u on the boundary $\partial\Omega$ to be u_D. Expressing the solution u in terms of finite element basis functions is done as follows:

$$u(x_i) = c_i \varphi_i(x_i) \tag{4.31}$$

Here, φ_i represents a piecewise polynomial and due to its following properties:

$$\varphi_i(x_j) = \delta_{ij}, \quad \delta_{ij} = \begin{cases} 1, & i = j, \\ 0, & i \neq j \end{cases} \tag{4.32}$$

(4.31) can be simplified to

$$u(x_i) = c_i \tag{4.33}$$

c_i are the coefficients we are ultimately interested int, often called *degrees of freedom*. An example of expressing a function u as a weighted sum of piecewise linear basis functions is shown in Fig. 4.5.

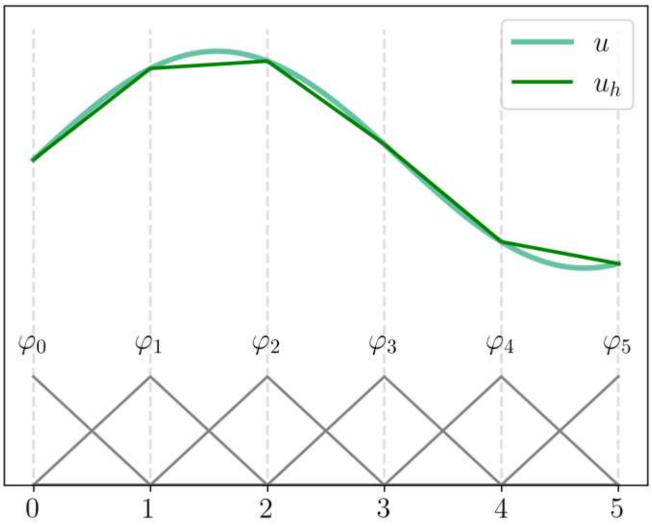

Figure 4.5: Approximation u_h of the function u as a weighted sum of piecewise linear basis functions φ_i.

The FEM uses the so-called weak formulation of the original problem to solve it. The attribute *weak* stems from the weaker requirements on the solution of the problem, as compared to its original formulation. In a first step, both sides of the original problem are multiplied by test functions v, chosen from a suitable function space V_h. By subsequently integrating this equation over the domain Ω, we get:

$$-\int_\Omega (\nabla^2 u)v \text{ dx} = \int_\Omega fv \text{ dx} \tag{4.34}$$

To lower the requirements on the basis functions with respect to differentiability, partial differential equations containing second derivatives are transformed into a representation containing only first derivatives. This can be achieved by integrating the left-hand side of Eq. (4.34) by parts:

$$-\int_\Omega (\nabla^2 u)v \text{ dx} = \int_\Omega \nabla u \cdot \nabla v \text{ dx} - \int_{\partial\Omega} \frac{\partial u}{\partial \mathbf{n}} v \text{ ds} \tag{4.35}$$

with $\frac{\partial u}{\partial \mathbf{n}} = \nabla u \cdot \mathbf{n}$ being the outward normal component of the gradient of u. The test function v needs to vanish at the parts of the boundary where the solution is known. This ensures that the basis functions do not create any contribution to the boundary value and allows to directly impose the known values, i.e. the Dirichlet condition. Thus, (4.35) reduces to:

$$-\int_\Omega (\nabla^2 u)v \text{ dx} = \int_\Omega \nabla u \cdot \nabla v \text{ dx} \tag{4.36}$$

and inserting this into (4.34) leads to

$$\int_\Omega \nabla u \cdot \nabla v \text{ dx} = \int_\Omega fv \text{ dx} \tag{4.37}$$

which is the weak formulation of the original problem. Often, this is expressed in the following more abstract variational form:

$$a(u,v) = L(v) \quad \forall v \epsilon V \tag{4.38}$$

with $a(u,v)$ being called *bilinear form* and $L(v)$ the *linear form*, which are defined as

$$a(u,v) = \int_\Omega \nabla u \cdot \nabla v \text{ dx} \tag{4.39}$$

$$L(v) = \int_\Omega fv \text{ dx} \tag{4.40}$$

As stated previously, in the process of bringing the original equation into its weak form, the test functions v have to be chosen from a suitable discrete function space V_h. The general requirements on such a discrete function space can be expressed as:

$$V_h = \{ \, v \,\epsilon\, L^2(\Omega) \mid \frac{dv}{dx} \,\epsilon\, L^2(\Omega), \text{ and } v(x) = 0 \; \forall x \,\epsilon\, \partial\Omega \, \} \tag{4.41}$$

with the *Hilbert* space $L^2(\Omega)$ consisting of all the functions which are square-integrable on Ω:

$$L^2(\Omega) = \int_\Omega v^2 dx < \infty \tag{4.42}$$

The function space V_h defined in (4.41) consists of all functions whose zeroth- and first-order derivatives are square integrable on Ω. Further, for V_h it is also required that v is zero at the boundary. Function spaces as defined in (4.41) are called *Sobolev spaces*. Though being very flexible in the choice of function space, usually the solution and test functions are chosen to be piecewise affine, globally continuous functions.

The discretized version of the variational form given in Eq. (4.38) can then be expressed as the linear system of equations

$$\sum_i A_{ij} u_i = b_j \tag{4.43}$$

with A_{ij} and b_j being defined as

$$A_{ij} = \int_\Omega \nabla\varphi_i \cdot \nabla\varphi_j \mathrm{dx} \tag{4.44}$$

$$b_j = \int_\Omega f\varphi_j \mathrm{dx} \tag{4.45}$$

and u_i being the discrete solution.

As the basis functions φ have compact support and are nonzero only on a small part of the domain Ω the matrix A is sparse. Further, the matrix A is symmetric and positive definite. Thus, iterative solvers can be employed to exploit these properties for the efficient solution of the linear system [122].

4.3.2 Discretization of the LLG Equation

The flow chart shown in Fig. 4.6 depicts the general sequence of operations of the simulation software ViennaMag [123], a FEM-based simulation tool for the computational investigation of MRAM devices. The software is written in C++ and is based on the FEM library MFEM [124]. MFEM provides the required basic FEM functionality, including efficient data structures, mesh handling, solvers, as well as means to save and visualize the results. On top of MFEM, ViennaMag adds the functionality specific to the simulation of micromagnetic systems, such as the calculation of the demagnetizing field, the spin accumulation, and the solution of the LLG equation. The phases of the simulation are described in the following.

In the initial phase, input parameters are read, such as the mesh of the structure which is to be simulated. The data structures are initialized to establish an initial magnetic configuration in the grid function representing the ferromagnetic layers. Additionally, the method used to calculate the demagnetizing field is selected, and the corresponding data structures are set up. Afterwards, the general simulation loop is started. First, the demagnetizing field is calculated for the given initial magnetization, followed by the computation of the spin accumulation. This part is performed in two steps: first, the charge current is computed followed by the solution of the systems of equations for the spin accumulation. The demagnetizing field and the spin accumulation are required inputs to the LLG equation and once they are available, the matrices can be assembled and the system of equations can be solved. After updating the magnetization and the time step, the next iteration is performed, until the final simulation time is reached.

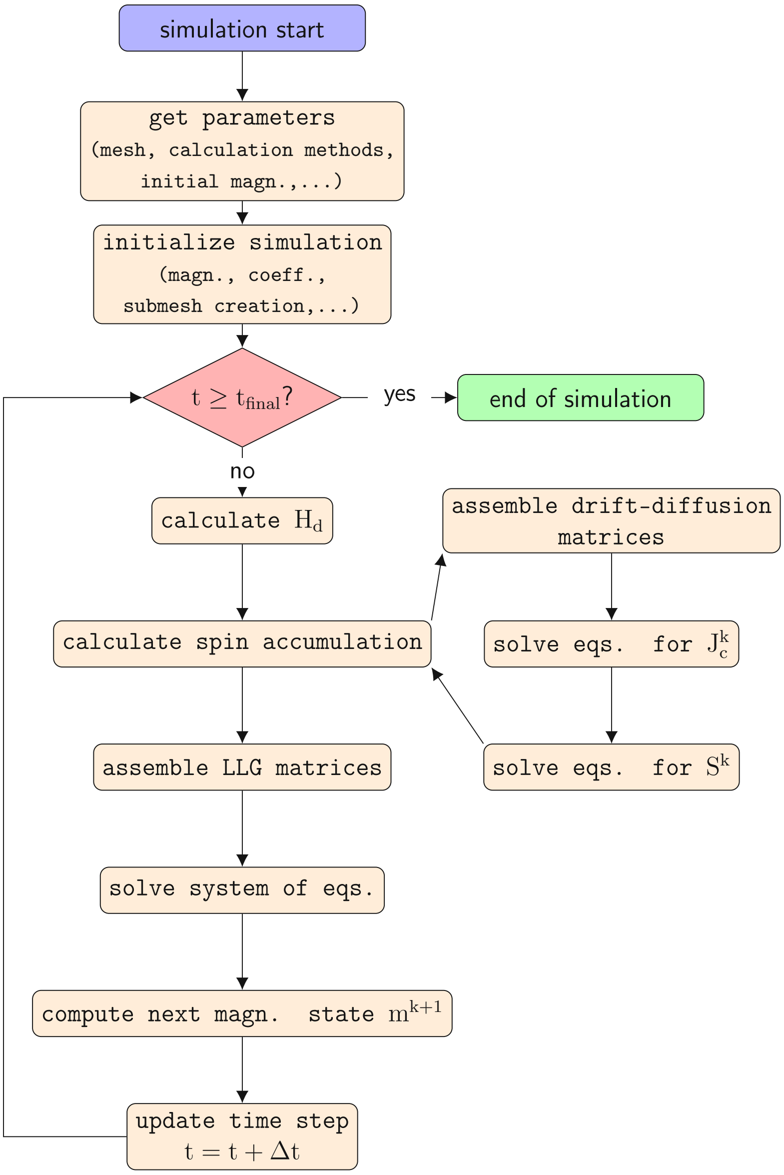

Figure 4.6: Flow chart of the general sequence of operations performed in the ViennaMag simulator.

The general equation which needs to be solved by the simulation, is based on the Landau-Lifshitz-Gilbert equation:

$$\alpha \frac{\partial \mathbf{m}}{\partial t} + \mathbf{m} \times \frac{\partial \mathbf{m}}{\partial t} = \gamma_0 \mathbf{H}_{\text{eff}} - \gamma_0 (\mathbf{m} \cdot \mathbf{H}_{\text{eff}}) \mathbf{m} \tag{4.46}$$

For the sake of stability, however, this is transformed into the tangent-plane integration scheme. The tangent-plane scheme solves for the time derivative of the magnetization instead of the magnetization directly. By inserting $\mathbf{v} = \frac{\partial \mathbf{m}}{\partial t}$ and multiplying by test functions $\mathbf{w}$ one gets the weak formulation of Eq. (4.46):

$$\int_\Omega (\alpha \mathbf{v} + \mathbf{m} \times \mathbf{v}) \cdot \mathbf{w} \, \mathrm{d}\mathbf{x} = \gamma_0 \int_\Omega \mathbf{H}_{\text{eff}}(\mathbf{m}) \cdot \mathbf{w} \, \mathrm{d}\mathbf{x} \tag{4.47}$$

After solving (4.47) for the time derivative of the magnetization $\mathbf{v}$, the new magnetization can be calculated as

$$\mathbf{m}^{k+1} = \mathbf{m}^k + \theta \, \Delta t \, \mathbf{v} \tag{4.48}$$

When employing the tangent-plane integration scheme, each field contribution can be treated implicitly by adding a θ to the corresponding expression. However, as the exchange field is the main source of stiffness in the LLG equation, in the formulation used in the simulation tool employed for this work, only the exchange field is treated implicitly. The following equation presents the full weak formulation as it is solved in the simulation tool depicted in Fig. 4.6:

$$\begin{aligned}
&\int_\omega \left(\alpha \mathbf{v} + \mathbf{m}^k \times \mathbf{v}\right) \cdot \mathbf{w} \, \mathrm{d}\mathbf{x} + \theta \frac{2A_{ex}\gamma}{M_S} \delta t \int_\omega \nabla \mathbf{v} : \nabla \mathbf{w} \, \mathrm{d}\mathbf{x} \\
= \gamma\mu_0 &\int_\omega (\mathbf{H}_{\text{ext}} + \mathbf{H}_{\text{K}} + \mathbf{H}_{\text{d}}) \cdot \mathbf{w} \, \mathrm{d}\mathbf{x} - \frac{2A_{ex}\gamma}{M_S} \int_\omega \nabla \mathbf{m}^k : \nabla \mathbf{w} \, \mathrm{d}\mathbf{x} \\
&+ \frac{D_e}{M_S} \int_\omega \left(\frac{1}{\lambda_J^2} \mathbf{S}^k + \frac{1}{\lambda_\varphi^2} \mathbf{m}^k \times \mathbf{S}^k \right) \cdot \mathbf{w} \, \mathrm{d}\mathbf{x}.
\end{aligned}$$

The demagnetizing field cannot be handled implicitly, as for its computation another partial differential equation must be solved. This will be described in more detail in Chapter 5.

The simulation software ViennaMag, whose flow chart is shown in Fig. 4.6, uses the MFEM library [124] to solve the weak formulation of the LLG equation. For the solution of the time derivative of the magnetization $\mathbf{v}$, the generalized minimal residual (GMRES) method is used, an iterative solver suitable for the solution of indefinite nonsymmetric systems of linear equations, as is the case for the present problem.

4.4 Reinforcement Learning

In the preceding sections, the Greek symbols α and γ have been employed in the context of micromagnetics, where α represents the Gilbert damping factor and γ denotes the gyromagnetic ratio. These symbols were chosen for their conventional usage within the field. In the field of reinforcement learning, however, α and γ are also used to denote the learning rate and the discount factor, respectively. Thus, in the following sections, the symbols α and γ will be used with their meaning in the context of reinforcement to maintain consistency with the conventions used in the literature. To avoid confusion, in the context the symbols are used in, their meaning will be explicitly stated.

4.4.1 Introduction

Machine learning can be roughly divided in three categories of algorithms, as shown in Fig. 4.7. The most prominent ones are the supervised learning algorithms which learn input-output relationships of given, labeled data sets. Examples include image recognition tasks, as well as natural language processing.

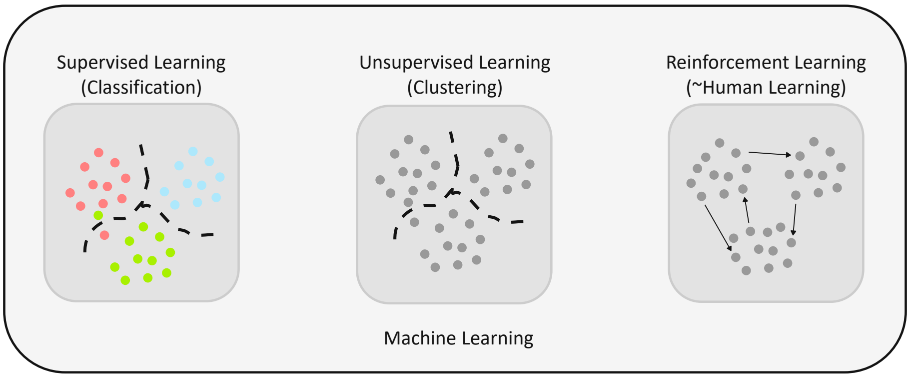

Figure 4.7: Machine learning branches.

Data for unsupervised learning algorithms on the other hand is not labelled, and the purpose of these algorithms is to make sense of the data and find patterns. The third category of machine learning algorithms is reinforcement learning. With its origins in optimal control theory and Markov decision processes, these algorithms try to computationally mimic the way humans and other animals learn. Driven by a goal which they try to achieve in a sequential decision-making problem, the data used for learning is generated during the training phase.

4.4.2 Markov Decision Processes

The mathematical basis for describing reinforcement learning are Markov decision processes (MDP). Originating from optimal control theory, MDPs describe decision-making processes in which current actions have influence not only on immediate rewards, but also on rewards further into the future. The difficulty thus lies in balancing decisions for instantaneous reward and for reward delayed in time. As depicted in Fig. 4.8, a reinforcement learning system consists of a learning agent and an environment. The agent's task is to achieve an objective by maximizing the accumulation of reward through repeated interaction with the environment. In this process, there are a number of signals which are exchanged between these two entities: the agent is able to perform *actions* in the environment, causing the environment to transition from its current state to a new one. This *state* information is returned to the agent together with a *reward* signal. Depending on whether the action performed by the agent was good with respect to the objective, the reward signal is used to *reinforce* good actions or *discourage* bad actions. This information is thus used by the agent to improve its action-producing function, commonly called *policy* and denoted as π.

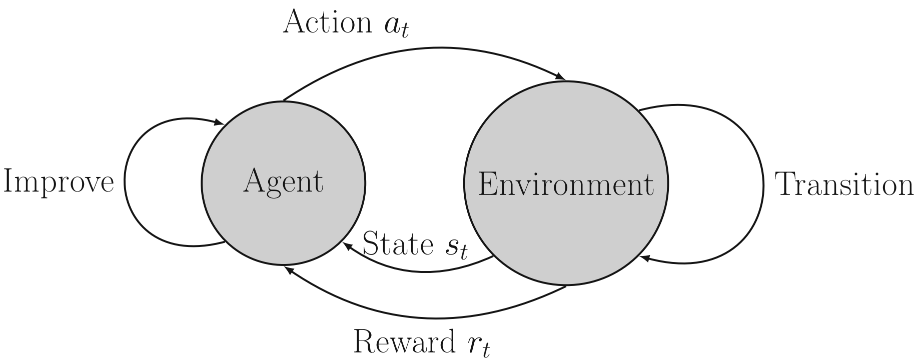

Figure 4.8: Basic setup of a reinforcement learning system.

Thus, in the course of training an RL agent, the trajectories of the signals exchanged by the agent and the environment follow the patterns

$$S_0, A_0, R_1, S_1, A_1, R_2, \cdots \tag{4.49}$$

with S_i being states, A_i actions and R_i rewards. In the MDP framework the environment is described as the transition function

$$p(s', r|s, a) \doteq \Pr\{S_t = s', R_t = r|S_{t-1} = s, A_{t-1} = a\} \tag{4.50}$$

It describes the dynamics of the environment by returning the probabilities with which the environment transitions into a next state s' and returns reward r, given that the environment is currently in state s and action a is taken.

For training an agent to learn how to best behave in order to achieve an objective, many iterations of the agent interacting with the environment are performed in which the agent experiences (*state, action, reward*) tuples. Each of these trajectories, spanning state transitions from the initial state to some terminal state, contributes to improving the agent's ability to navigate the environment's state space. A very important property of the state in the MDP framework is that it possesses the *Markov property*. This means, that the state has to contain enough information about the past to be sufficient for the agent to make a decision at the current time step. Many real-life problems can be framed as RL decision-making problems and there are no clear-cut rules on how to divide goal-directed problems into agent and environment. What is clear, however, is that the agent needs to have enough control over the environment, such that it is possible to achieve the desired objective.

The reward signal is one of the most important and prominent features in RL. It encodes the goal that is to be achieved and leads to the notion of overall return over the timespan of the task, which is to be maximized by the agent. The reward function returns a scalar value which can be either positive or negative and is an indication of how good (or bad) the state transition from the previous time-step $t-1$ to the current time step t was. The exact definition of the reward is implementation-dependent, as it can be sufficient for the reward to only depend on the previous state s, but often also the performed action a, and potentially even the next state s' are taken into account.

A definition for a reward which depends on the tuple (s, a) looks as follows:

$$r(s,a) \doteq \mathbb{E}\left[R_t | S_{t-1} = s, A_{t-1} = a\right] \tag{4.51}$$

The reward is thus defined as the expected value of the reward at time t, R_t, given that the environment is in state s and action a is taken. Consequently, in a deterministic environment $r(s,a)$ would exactly equal the reward R_t.

Whereas the reward function in Eq. (4.51) gives a general definition for the reward whose explicit expression depends on the problem at hand, there is the notion of the return, the overall reward accumulated during a task episode:

$$G_t = R_{t+1} + \gamma R_{t+2} + \gamma^2 R_{t+3} + \cdots = \sum_{k=t+1}^{T} \gamma^{k-t-1} R_k \tag{4.52}$$

The return at time t, G_t, is the discounted cumulative reward, with T being the episode length of the task to be learned, R_k the reward received at time k and γ the discount factor, a positive real value commonly chosen to be less than one. The choice of γ balances how strongly future rewards influence the estimate of the return and thus the decision-making of the learning agent. If γ is zero, an agent knowing the return at time t can only act short-sighted, as his information horizon does only include the reward for the current time step. Figure 4.9 shows how different choices of γ affect the discounting of future rewards, i.e. it answers the question “How much is a reward received t time steps in the future worth now”?

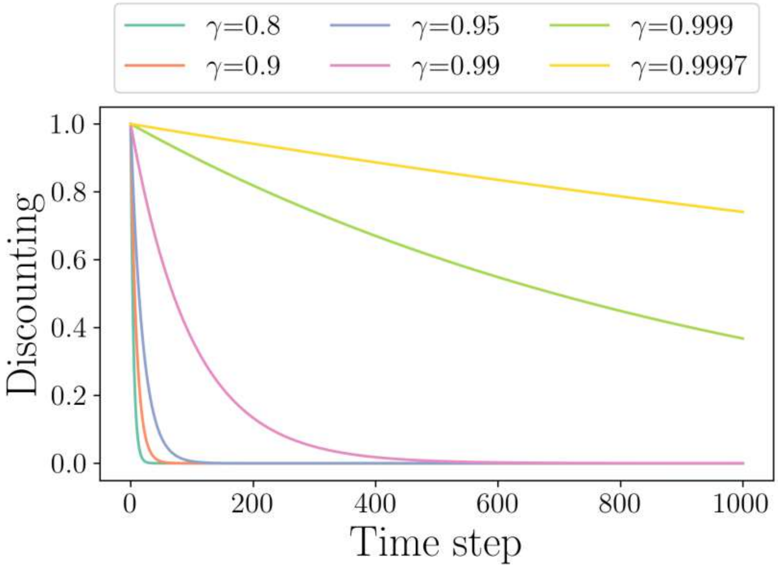

Figure 4.9: Discounting of different γ values over time.

Looking at the two extremes shown in Fig. 4.9, when choosing $\gamma = 0.8$, after only around 20 time steps discounting reduces the reward to below 1% and very quickly goes to zero, encouraging short-sighted decisions. Setting $\gamma = 0.9997$, on the other hand, a reward received 1000 times steps in the future is only discounted by ~ 0.74 and will thus still have an influence on the decision-making at the present time step [125].

However, one of the biggest difficulties in RL lies in defining a rewarding scheme which unambiguously encodes the desired objective. It was shown in various publications that it can easily happen, that, when not carefully designed, a reward function can lead the agent to learning suboptimal behavior which exploits an imperfect rewarding strategy and achieves a higher accumulated reward by taking an undesired sequence of actions, a behavior called “specification gaming” [126–129].

The way most RL agents judge how good the environment’s current state and specific actions are, is by maintaining a *value function*. Value functions are estimates for the expected return for following a certain policy of action, given the state the agent is currently in. With policies being given as $\pi(a|s)$, a mapping from a given state to an action, the value function for state s following policy π is defined as

$$v_\pi(s) \doteq \mathbb{E}_\pi \left[R_t | S_t = s \right] \tag{4.53}$$

However, for deciding what to do in a specific state, having an estimate of the value function does not help much. A more useful function is the *action-value function*

$$q_\pi(s,a) \doteq \mathbb{E}_\pi \left[R_t | S_t = s, A_t = a \right] \tag{4.54}$$

In contrast to the value function, it directly gives estimates for the value of all possible actions, whereas the value function combines these estimates.

An important feature of these value functions is that they can be written in recursive form, which describes the relationship of the value of state s and its successor states. This recursive formulation is the so-called *Bellman equation* for the value functions. For the action-value function q_π it looks as follows:

$$q_\pi(s,a) = \sum_{s',r} p(s',r|s,a) \left[r + \gamma v_\pi(s') \right] \quad \forall s \in \mathcal{S},\ \forall a \in \mathcal{A}(s) \tag{4.55}$$

The value function as well as the action-value function depend on a specific policy. If the policy changes, so does the estimation of the value function and action-value function, respectively. It was already mentioned, that they are action-producing functions, given a current state of the environment. It should be added, though, that they are not merely a static plan for a specific trajectory through an environment. Policies should be plans that are universal in the sense that they should provide actions for all possible states and not just for a subset of them.

Knowing about policies and how the quality of states can be described by value functions, what is left is to find out about algorithms that deal with the problem of approximating value functions and improving policies such that they converge towards the optimal ones. This is done using a process called generalized policy iteration (GPI) and consists of two phases. In the first phase, the current policy is evaluated (“Policy Evaluation”) and in the second phase the policy is improved based on the outcome of the evaluation (“Policy Improvement”). Evaluation of a given policy works by going through the state space and iteratively improving the estimates of the value function. This iterative process is usually performed until the change to the value function is below a certain threshold. The value function in the end gives an idea of how good a state (or state-action pair in the case of the action-value function) is, when following the given policy. With a way at hand to evaluate any given policy, one approach for coming up with a better policy could be to randomly generate new policies, evaluate them using this evaluation approach and select the best one to continue. A better and more efficient way to improve the current policy is to make use of the action-value function Q.

As the action-value function assigns a value for each state-action pair, one can easily adjust the current policy to take the action with the highest value estimate in the respective states.

4.4.3 (Deep) Reinforcement Learning Algorithms

After presenting the basics of reinforcement learning in the previous section, the upcoming sections shall introduce the different types of RL algorithms and present one of them, the Deep Q-Network algorithm in more detail.

Value-Based Algorithms

Value-based algorithms aim to assign a value to states or state-action pairs, representing the potential overall reward the agent can expect, i.e. how valuable a state or state-action pair is. Decisions are made by choice of a policy which, in most cases is based on the approximated value.

Policy-Based Algorithms

In policy-based algorithms, the policy, i.e. the mapping from states to actions, is learned directly. No value function indicating the expected return in any specific state is being approximated.

Model-Based Algorithms

Whereas policy-based algorithms directly learn the state-action mapping and value-based algorithms learn a proxy allowing for the best action selection, model-based algorithms directly learn a model of the environment or use an existing model, if the dynamics of the environment are known. This allows for the prediction of the behavior of the environment and thus these algorithms can “predict” how the environment will respond to certain actions.

In the following we will focus on value-based reinforcement learning algorithms, as these are the ones which are used in this thesis.

4.4.4 Estimating Value Functions

Now we know how the action-value function is defined. But how do we arrive at a good estimate of it?

Two of the most well-known methods in RL for the estimation of the action-value function are SARSA [130] and Q-learning [131]. The target update equations are:

$$\text{SARSA:} \quad Q_{\text{target}}(S_t, A_t) = r + \gamma Q(S_{t+1}, A_{t+1}) \tag{4.56}$$

$$\text{Q-Learning:} \quad Q_{\text{target}}(S_t, A_t) = r + \gamma \max_a Q(S_{t+1}, a) \tag{4.57}$$

The difference between the two update equations is that the SARSA algorithm on the right-hand side uses the action which was actually taken at time-step $t+1$ to calculate the value of the action-value function. The Q-learning algorithm, on the other hand, uses the action which returns the maximum value from the action-value function. These different approaches are called *on-policy* (SARSA) and *off-policy* (Q-learning).

The target update, however, is only an intermediate result for the actual update of the action-value function:

$$Q(S_t, A_t) = Q(S_t, A_t) + \alpha_t \left[Q_{\text{target}}(S_t, A_t) - Q(S_t, A_t)\right] \tag{4.58}$$

One of the biggest difficulties in RL is the trade-off between *exploration* and *exploitation*. Should the agent exploit its current knowledge and base all decisions on the present approximation of the value function, or should it continue to explore the state-action space? By focussing too much on the exploitation of existing knowledge the agent risks getting stuck in a local maximum. With the current estimate of the value function, a certain action might promise the highest reward, exploration of other actions, however, could possibly lead to an even higher overall return. The most prominent policy balancing exploration and exploitation is the so-called ϵ-greedy policy. Here, in ϵ percent of the cases, a random action is taken, at all other times it's the action promising the highest return for the respective state.

4.4.5 Deep Q-Network Algorithm

The deep Q-network algorithm (DQN) is an important algorithm in the history of RL. It was first published in [132], where the authors presented how using this algorithm, an agent could be trained to play Atari games with superhuman performance with merely receiving the pixel images as state information. Later on an improved version was published in [133].

First, the "deep" in its name stems from the fact that it uses a deep neural network to approximate the action-value function, for which the notation needs to be changed to $Q(S_t, A_t, \theta_t)$, as it now also depends on the neural network weights θ_t, which are changing as training progresses. Using neural networks as universal approximators has become the standard in practical applications, where usually the amount of states cannot be reasonably represented anymore with table-based approaches [134].

The DQN algorithm can be broken down into three main tasks: collecting experiences, calculate the target update for the experiences, update the action-value function estimate. A simple version of the algorithm which will be discussed in more detail is given in Algorithm 4.1:

Algorithm 4.1: Deep Q-Network Algorithm

```
1 for each step do
2     gather experience $(S_i, A_i, R_i, S_{i+1})$
3     for each batch do
4         $y_i \leftarrow r_i + \gamma \max_a Q_\pi(S_{i+1}, a, \theta^-)$
5         $L(\theta) \leftarrow \frac{1}{N} \sum_i (y_i - Q^\pi(S_{i+1}, A_i, \theta_i))^2$
6         $\theta \leftarrow \theta - \alpha \nabla_\theta L(\theta)$
7     end
8 end
```

As stated in Line 2, at the beginning of each time step, the agent gathers experience tuples $e_i = (S_i, A_i, R_i, S_{i+1})$ using the current policy, e.g. an ϵ-greedy policy. These experiences are stored in a buffer, from where batches of a pre-defined size are randomly sampled. Using these samples, the target update in Line 4 is performed. This target is then used in Line 5 to calculate the mean-squared error loss, whose gradient is subsequently computed. With the gradient one knows in which direction to move the weights, taking small steps scaled by the learning rate α, in order to reduce the loss and get a better approximation of the action-value function. The DQN algorithm uses two sets of neural network weights, the constantly updated ones, θ_i in Lines 5 to 6, and a set of weights that is only updated at larger intervals, θ^- in Line 4, to avoid the chasing of a moving target when evaluating the loss in Line 5.

Chapter 5

Efficient Demagnetizing Field Calculation

In the following, methods for the numerical computation of the demagnetizing field described in Section 3.2.3 will be presented and compared. The computational complexity due to the long-range interaction of the magnetic moments poses a challenge which will be discussed as well.

5.1 Truncation Approach

The simplest approach to approximate the open boundary condition and compute the demagnetization field is the so-called truncation approach. Here, the magnetic domain Ω_m is surrounded by an external domain Ω_e, exemplified in Fig. 5.1 by a magnetic cube surrounded by a spherical non-magnetic domain. This external domain is truncated at a certain distance, hence the name of the method.

The Poisson equation given in (3.18b) is then solved in the whole computational domain with Dirichlet boundary conditions setting the magnetic potential to zero at the outer surface of the sphere to account for the decay of the potential:

$$H_d = -\nabla u \tag{5.1}$$

$$u = 0 \qquad \text{on } \partial\Omega_e \tag{5.2}$$

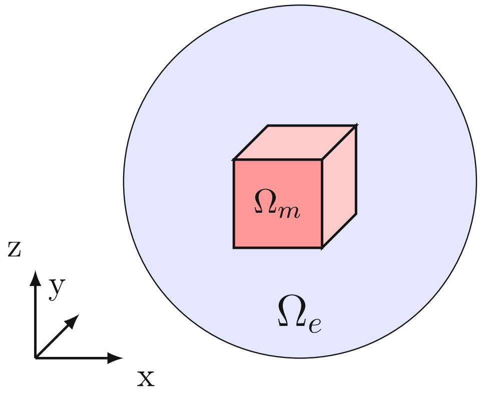

Figure 5.1: Truncation approach: truncating a non-magnetic external domain Ω_e surrounding the magnetic domain Ω_m at a finite distance.

The weak formulation to calculate the scalar magnetic potential based on Eq. (3.18b), reads as

$$\int_\Omega \nabla \cdot (\nabla u - M_s \mathbf{m})\, v d\mathbf{x} = 0 \tag{5.3}$$

Thus, the equation is solved in the whole domain $\Omega = \Omega_m \cup \Omega_e$. And when restricting the test and trial functions to the following space

$$V_0 = \{v \in V : v(\mathbf{x}) = 0 \quad \forall \mathbf{x} \in \partial\Omega\}\,, \tag{5.4}$$

and by integration by parts of Eq. (5.3) leads to:

$$\int_\Omega \nabla u \cdot \nabla v d\mathbf{x} = \int_\Omega M_s \mathbf{m} \cdot \nabla v d\mathbf{x} \quad \forall\, v \in V_0 \tag{5.5}$$

Of course, setting the potential to zero at a finite distance is an approximation and as the potential should reach a value of zero only at infinity, the larger the dimension of the external domain, the better the approximation. This, however, also comes with higher computational effort. Choosing the dimension of the external domain ~ 5 times the dimension of the magnetic domain in general leads to a good compromise between computational demand and accuracy [135]. As the potential decays slowly, to further save computational resources the mesh can progressively be made coarser towards the outer surface of the external domain (cf. Fig. 5.1).

5.2 FEM-BEM Approach

An approach which allows a reduction of the computational domain to the magnetic regions only, combines the finite element method with the boundary element method (BEM). It was introduced in the early 1990s in [136] and is implemented and used in this thesis to solve the open boundary problem of the demagnetizing field computation. In the following, the general idea of the method will be introduced, and the computational implementation will be discussed.

5.2.1 General Description

Like in the truncation approach, presented in Section 5.1, the hybrid FEM-BEM approach also uses the scalar magnetic potential as an intermediate quantity to be calculated, from which afterwards the gradient is taken to compute the demagnetizing field.

The ansatz of this approach is to split the potential u as

$$u = u_1 + u_2 \tag{5.6}$$

The partial potential u_1 accounts for the divergence of the magnetization and is calculated by solving the Poisson equation inside the magnetic domain Ω_m and u_1 is set to zero outside:

$$\nabla^2 u_1(\mathbf{r}) = \nabla \cdot \mathbf{M} \quad \text{for } \mathbf{r} \in \Omega_m \tag{5.7a}$$

$$u_1 = 0 \quad \text{for } \mathbf{r} \notin \Omega_m \tag{5.7b}$$

At the interface of magnetic and non-magnetic regions, the following Neumann boundary condition must be fulfilled:

$$\nabla u_1 \cdot \mathbf{n} = \mathbf{M} \cdot \mathbf{n} \quad \text{for } \mathbf{r} \in \partial\Omega_m \tag{5.8}$$

To have potential $u = u_1 + u_2$ satisfy the properties described in Section 3.2.3, the partial potential u_2 must satisfy the following Laplace equation in the whole domain Ω:

$$\nabla^2 u_2(\mathbf{r}) = 0 \quad \text{for } \mathbf{r} \in \Omega \tag{5.9}$$

as well as the two boundary conditions $\partial\Omega_m$:

$$\left(\nabla u_2^{in} - \nabla u_2^{out}\right) \cdot \mathbf{n} = 0 \tag{5.10}$$

and

$$u_2^{in} - u_2^{out} = u_1^{in} \tag{5.11}$$

$u_{1,2}^{in}$ and $u_{1,2}^{out}$ are the values of the potential at the inside (magnetic domain) and at the outside (nonmagnetic domain) of the interface $\partial\Omega_m$. The following double-layer potential fulfills the requirements given in Eqs. (5.9) to (5.11):

$$u_2(\mathbf{r}) = \frac{1}{4\pi} \oint_{\partial\Omega_m} u_1(\mathbf{r}') \frac{\partial}{\partial \mathbf{n}} \frac{1}{|\mathbf{r} - \mathbf{r}'|} \mathrm{dS}' \tag{5.12}$$

It would be possible to evaluate (5.12) in the whole magnetic domain. However, the discretization of the integral operator in Eq. (5.12) leads to densely populated matrices, which, as opposed to the sparse matrices in FEM, are computationally more expensive to handle and the computation scales with $\mathcal{O}(n^2)$. Thus, (5.12) is only evaluated at the boundary of the magnetic domain $\partial\Omega_m$ by means of the boundary-element method. After discretization, the relation between the boundary values of u_1 and u_2 results in the following matrix-vector multiplication:

$$\underline{u_2} = \mathbf{B}\underline{u_1} \tag{5.13}$$

The size of B and thus its memory consumption still scale with $\mathcal{O}(n^2)$. A remedy for the unfavorable memory consumption arising from this scaling behavior are matrix compression algorithms [137, 138]. So-called hierarchical matrix compression algorithms decompose a matrix into low-rank sub-matrices and improve the scaling of the handling of these matrices to $\mathcal{O}(n\ \log(n))$. Figure 5.2 shows the improved scaling of the memory consumed by the BEM operator matrix with and without compression algorithms.

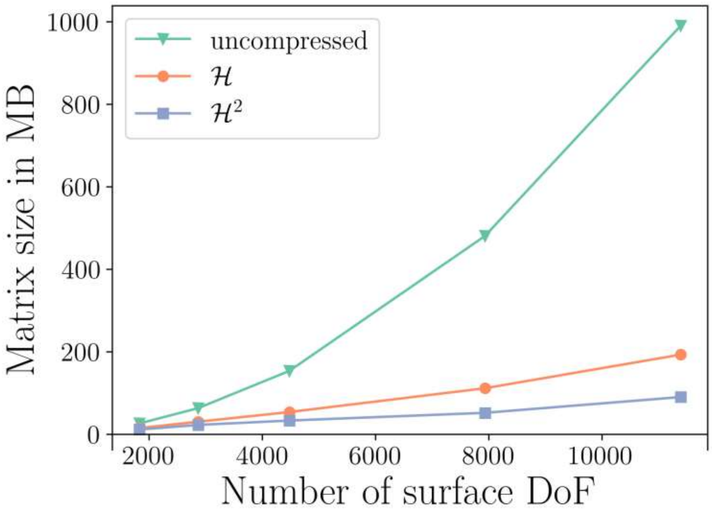

Figure 5.2: Scaling of matrix size with number of surface degrees of freedom. Comparison of the uncompressed matrix with $\mathcal{H}$- and $\mathcal{H}^2$-compressed matrices. This figure was published in [139]

5.2.2 Disconnected Geometries

As the interaction of the magnetic moments acts over a long range, even the magnetic moments in structures consisting of multiple disconnected magnetic regions interact with each other. Figure 5.3 depicts the approach how, in a simulator handling complete MRAM cell simulation, the FEM-BEM method can be implemented to account for these interactions.

First, a full mesh consisting magnetic and nonmagnetic domains needs to be preprocessed. A surface mesh of only the magnetic regions needs to be extracted. This mesh can subsequently be used to set up the BEM operator matrix. In this case, this is done by a BEM library which then returns a discretized version of (5.12).

Figure 5.4 shall exemplify how the interaction between magnetic moments in disconnected magnetic domains is properly incorporated. The three discs are uniformly magnetized in the directions as indicated by the arrows in the middle. Figure 5.4a presents the calculated scalar magnetic potential. In a scenario where no interaction would be considered, the potential would be varying linearly in the direction of the uniform magnetization. One can clearly see that this is not the case and that the potentials are shifted.

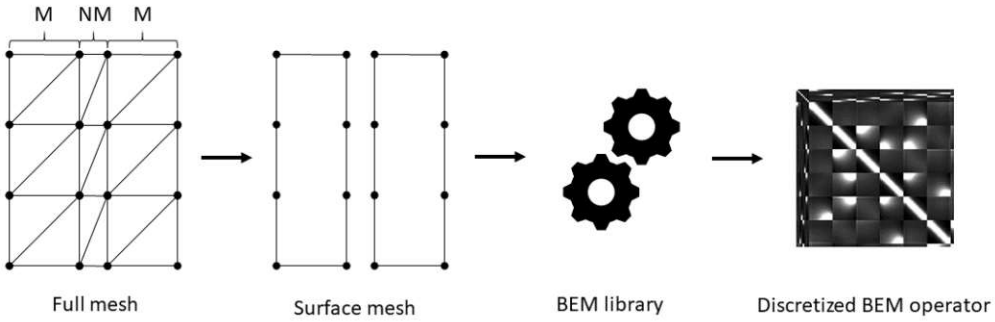

Figure 5.3: Depiction of the process for discretizing a boundary integral operator, which considers the interaction between disconnected magnetic parts. This figure was published in [139]

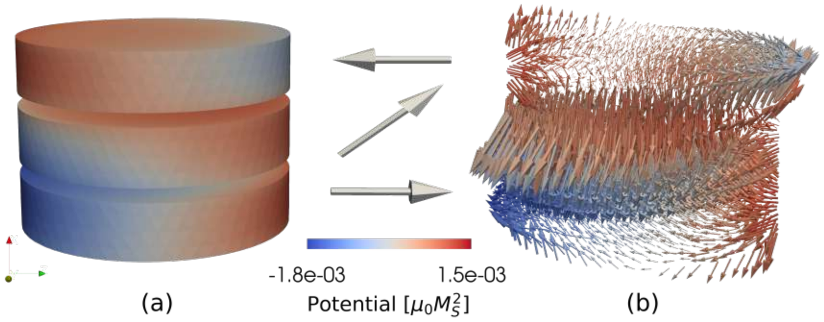

Figure 5.4: Magnetic potential (a) and demagnetizing field (b) calculated for a three-layer structure. The arrows indicate the magnetization orientation in the respective layers. The color-coding in both figures indicates the magnetic potential value. This figure was published in [139]

5.3 Benchmark Results

The Micromagnetic Modeling Activity Group[1] at the NIST Center for Theoretical Computational Materials Science has defined a set of standard problems which allow researchers to compare their micromagnetic simulation software with published results. In the following magnetization states as described in the μMag standard problem #3 [140] as well as problem settings for which analytical solutions are available will be used to verify the

---

[1] `https://www.ctcms.nist.gov/~rdm/mumag.org.html`

correctness of our implementation of the two methods for the computation of the demagnetizing field. A unit cube with three different magnetization states will be used to evaluate the accuracy of the two methods for single ferromagnetic domains. Then, analytic expressions for the computation of the demagnetizing field outside a ferromagnetic disc will be used to evaluate the quality of the methods in a multi-domain scenario. These diverse test cases provide a comprehensive evaluation of the two methods.

For a uniformly magnetized unit cube, the demagnetizing field and thus the demagnetizing energy given as

$$\mathbf{E}_d = -\frac{\mu_0 M_S}{2} \int_\Omega \mathbf{m} \cdot \mathbf{H}_{\mathrm{d}} \mathrm{d}\mathbf{x} \tag{5.14}$$

can be calculated analytically. Figure 5.5 shows the initial magnetization (Fig. 5.5a) as well as the result of the calculated scalar magnetic potential (Fig. 5.5b). Qualitatively, one can see in Fig. 5.5b that the magnetic potential is highest at the top interface of the cube, where the divergence of the magnetization is highest. A quantitative discussion of the results follows after the presentation of the remaining test cases.

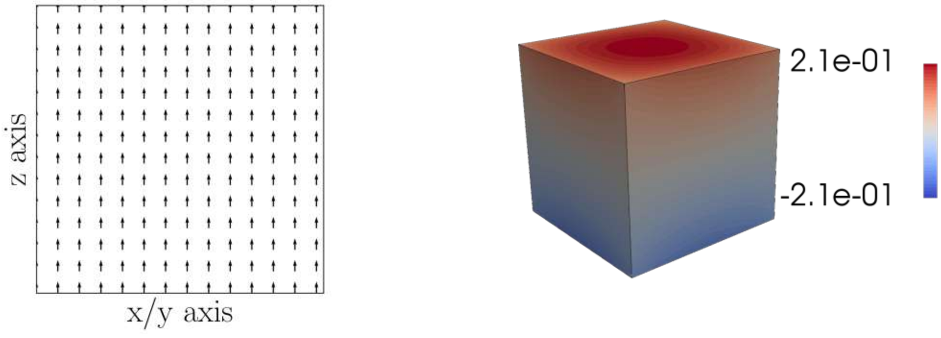

(a) (b)

Figure 5.5: (a) Uniform magnetization (b) Magnetic potential

[140] defines two more scenarios with non-uniform magnetization. The first of these uses an initialization of the magnetization into a so-called flower state which is defined as the normalized version of [141]

$$\mathbf{m}_x(\mathbf{r}) = \frac{1}{a}xz \tag{5.15}$$

$$\mathbf{m}_y(\mathbf{r}) = \frac{1}{c}yz + \frac{1}{b^3}y^3z^3 \tag{5.16}$$

$$\mathbf{m}_z(\mathbf{r}) = 1 \tag{5.17}$$

For this initialization, the center of the unit cube must lie at (0, 0, 0). a, b and c are parameters free to choose. In accordance with [141], the values were chosen to be $a = c = 1$ and $b = 2$.

The initial magnetization state and the resulting scalar magnetic potential can be seen in Fig. 5.6.

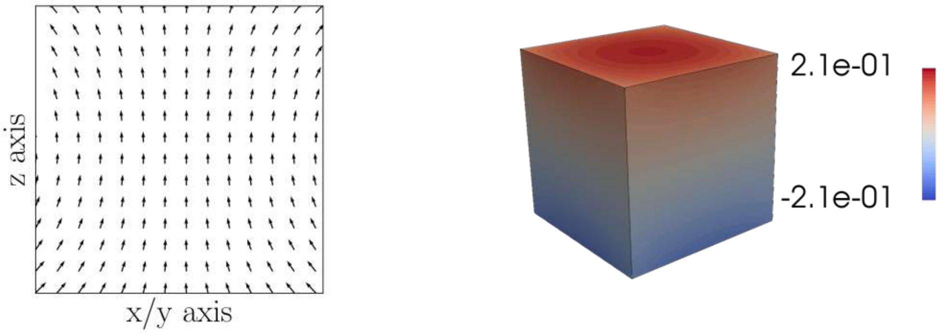

(a) (b)

Figure 5.6: (a) Flower magnetization (b) Magnetic potential

The third test case initializes the magnetization into a vortex state (cf. Fig. 5.7a). The magnetization in the unit cube is described by the following equations

$$\mathbf{m}_x(\mathbf{r}) = -\frac{y}{r}\left(1 - \exp(-4\frac{r^2}{r_C^2})\right)^{1/2} \tag{5.18}$$

$$\mathbf{m}_y(\mathbf{r}) = \frac{x}{r}\left(1 - \exp(-4\frac{r^2}{r_C^2})\right)^{1/2} \tag{5.19}$$

$$\mathbf{m}_z(\mathbf{r}) = \exp\left(-2\frac{r^2}{r_C^2}\right) \tag{5.20}$$

Here, $r = \sqrt{x^2 + y^2}$ and r_C being the radius of the vortex, which was set to 0.14, in accordance with [141].

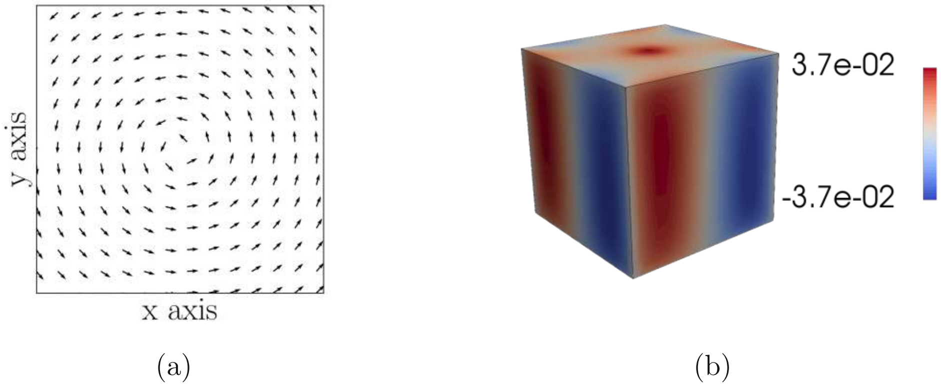

(a)

(b)

Figure 5.7: (a) Vortex magnetization (b) Magnetic potential

Figure 5.8 presents a comparison of the demagnetizing energies of the three aforementioned magnetization states, computed with the truncation approach as well as the FEM-BEM approach compared to the reference result [141]. In all three test cases, the FEM-BEM method consistently demonstrates improved agreement with the reference result when employing an identical mesh resolution for the magnetic domain.

A closer look at the relative error shown in Fig. 5.9 gives more quantitative insight. While the maximum relative error of the FEM-BEM approach rises to ∼5% in the vortex scenario, and otherwise lies below 1%, the relative error of the truncation approach is consistently above 10%.

So far, only single magnetic domains were tested, and the correct computation of the demagnetizing field inside the magnetic domain was evaluated. In [142], an analytic expression to calculate the component of the demagnetizing field along the symmetry axis of a ferromagnetic disc outside the ferromagnetic domain can be found and reads as follows

$$H_d(x) = \frac{\mu_0 \mathbf{M}}{2} \left(\frac{x}{\sqrt{x^2 + R^2}} - \frac{x - L}{\sqrt{(x - L)^2 + R^2}} \right) \tag{5.21}$$

This equation describes a scenario where the x-axis is the symmetry axis, L the thickness of the magnetic disc and R its radius.

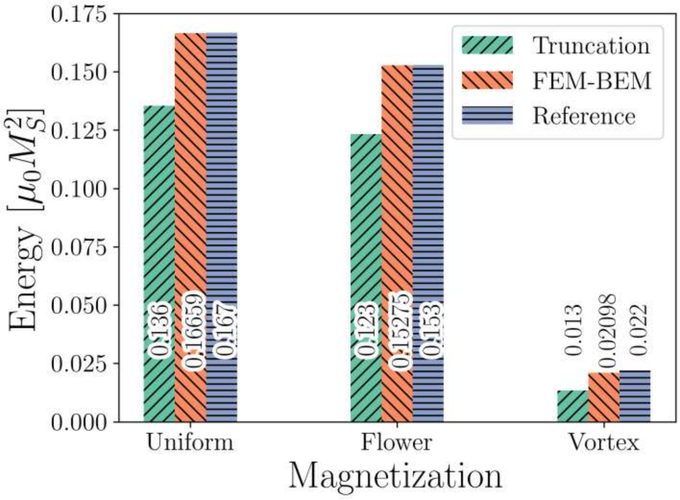

Figure 5.8: Demagnetizing energy for differently magnetized unit cubes computed using the truncation approach and the FEM-BEM method compared to the reference result.

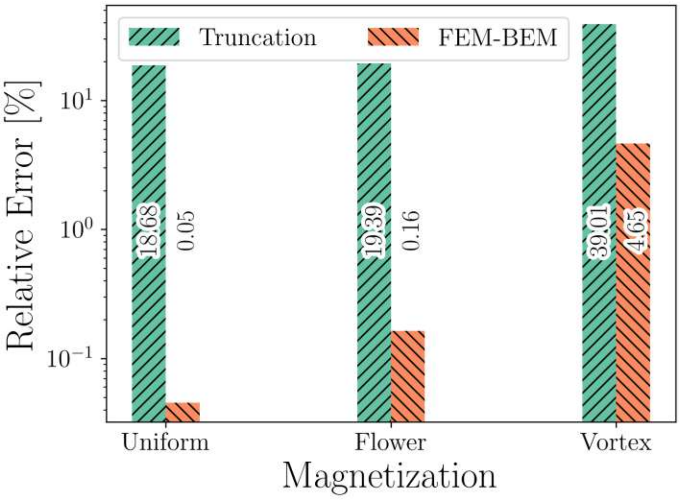

Figure 5.9: Relative error of the demagnetizing energy for differently magnetized unit cubes computed using the truncation approach and the FEM-BEM method.

First, simulations of a single ferromagnetic disc with a thickness of 0.1 nm and a radius of 1 nm, uniformly magnetized in the x direction, were performed, and its value was compared to the analytic one. The value of the demagnetizing field component along the symmetry axis was then compared between a distance of 2 nm and 7 nm. The results of this analysis are shown in Fig. 5.11.

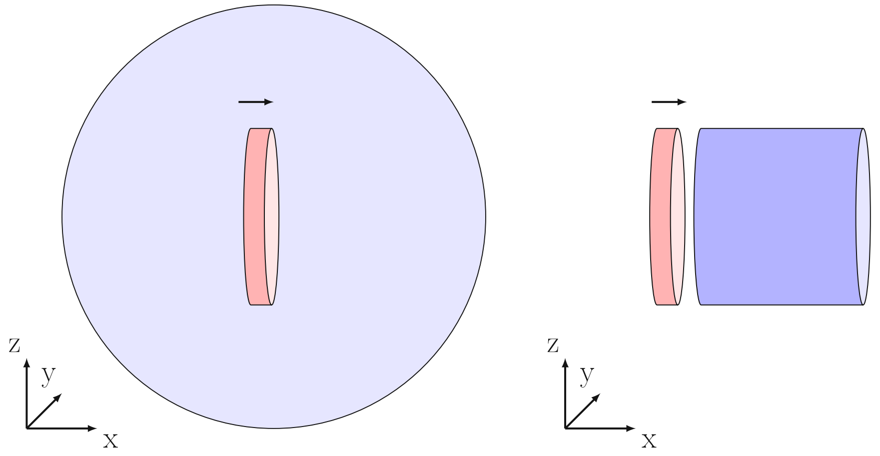

(a) Truncation (b) FEM-BEM

Figure 5.10: Computational domains for the evaluation of the demagnetizing field outside the ferromagnetic region (red) with the respective computational methods.

As can be seen, the hybrid FEM-BEM approach reproduces the demagnetizing field very well and achieves a relative error which reaches its highest value at a distance of 7 nm with 1%. The truncation approach, however, is only able to match the analytic results with a relative error at around 10%, closer to the magnetic domain even reaching 13%.

Further simulations are performed to evaluate the accuracy of the two methods with respect to also considering interaction between magnetic domains. For this purpose, again a magnetic disc will be used, however, with a second magnetic disc placed at a certain distance.

Figure 5.12a shows the computational domain used for calculating the demagnetizing field employing the truncation approach. As required by this method, the two magnetic discs are surrounded by a nonmagnetic region.

As the hybrid FEM-BEM approach only takes into account the magnetic domain and thus the demagnetizing field values are not available outside, the test structure has to be adjusted as shown in Fig. 5.12b. In order to receive values for the demagnetizing field between the two magnetic discs, a third magnetic disc is inserted in the middle. The disc in the middle, however, possesses a saturation magnetization $\ll 1 \frac{A}{m}$, allowing the evaluation of the demagnetizing field in this region of space without distorting its calculation.

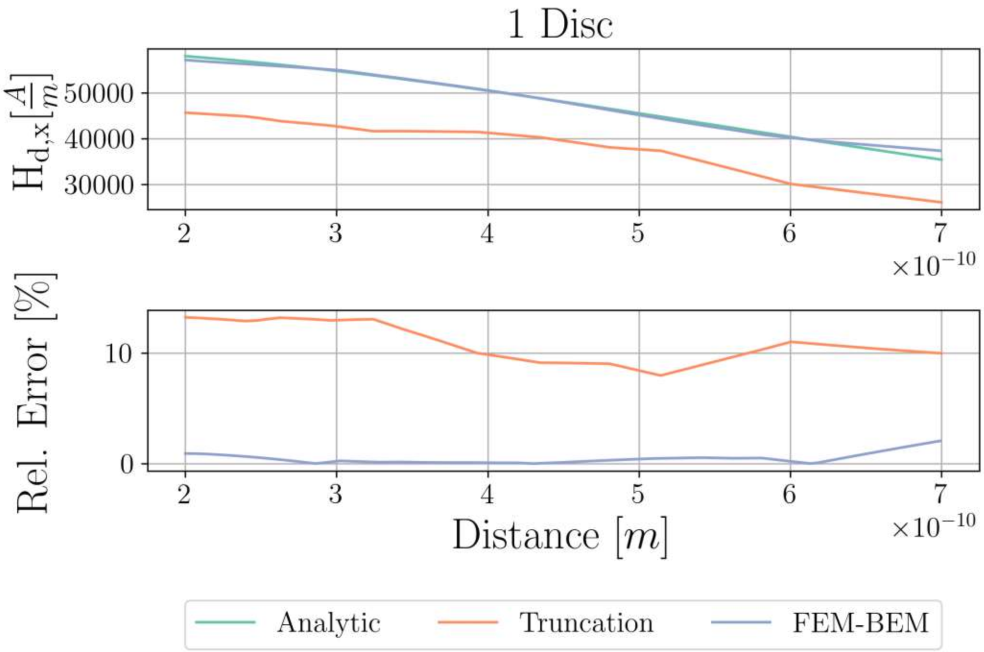

Figure 5.11: Demagnetizing field component along the symmetry axis of a magnetic disc with L=0.1 nm and R=1 nm.

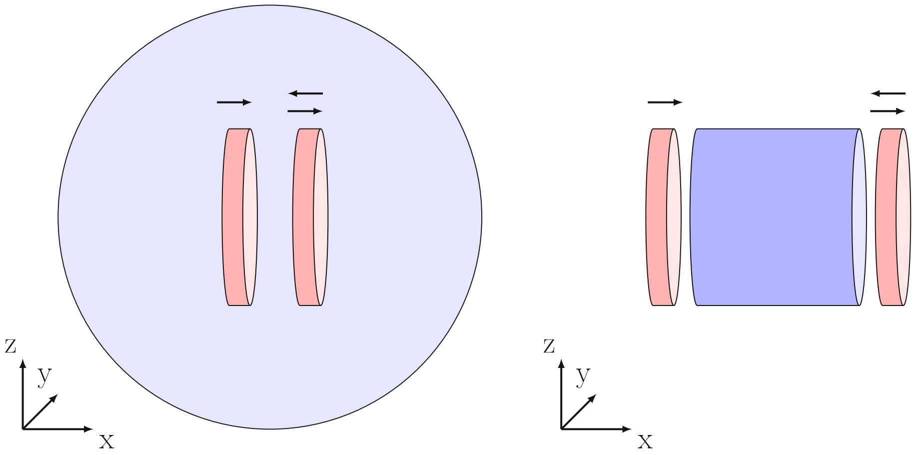

(a) Truncation

(b) FEM-BEM

Figure 5.12: Computational domains for the evaluation of the demagnetizing field outside the ferromagnetic region (red) in a multi-domain scenario.

Figure 5.13 presents a comparison of the truncation approach and the FEM-BEM method with the analytic formula for two magnetic discs with parallel magnetization. It can be seen that all results are in qualitative agreement, but the field value is again strongly underestimated by the truncation approach. The relative error again is consistently above 10%, while the FEM-BEM results lie on top of the analytic values, only close to the boundary the relative error rises to 0.44%.

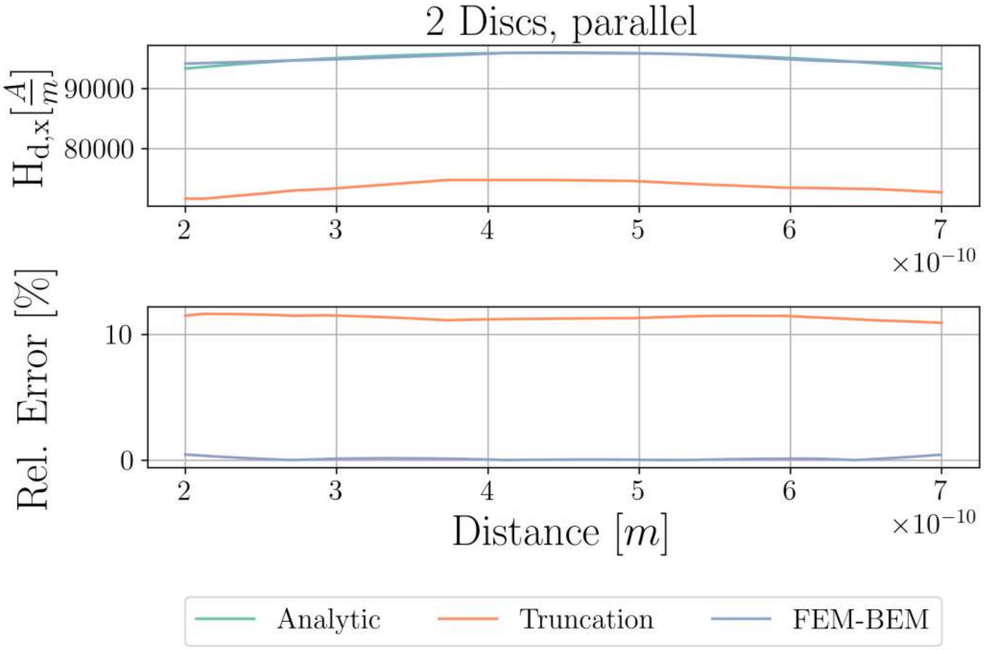

Figure 5.13: Demagnetizing field component along the symmetry axis of two magnetic discs with L=0.1 nm and R=1 nm and parallel magnetization. Upper panel: absolute field values. Lower panel: relative error.

Changing the scenario to an antiparallel configuration of the magnetic discs leads to the results shown in Fig. 5.14. Again, qualitative agreement is achieved by both methods, however, more so with the FEM-BEM approach. The zero-crossing of the demagnetizing field component accurately determined by both methods, but towards the ends of the tested distance range the errors grow for both of them.

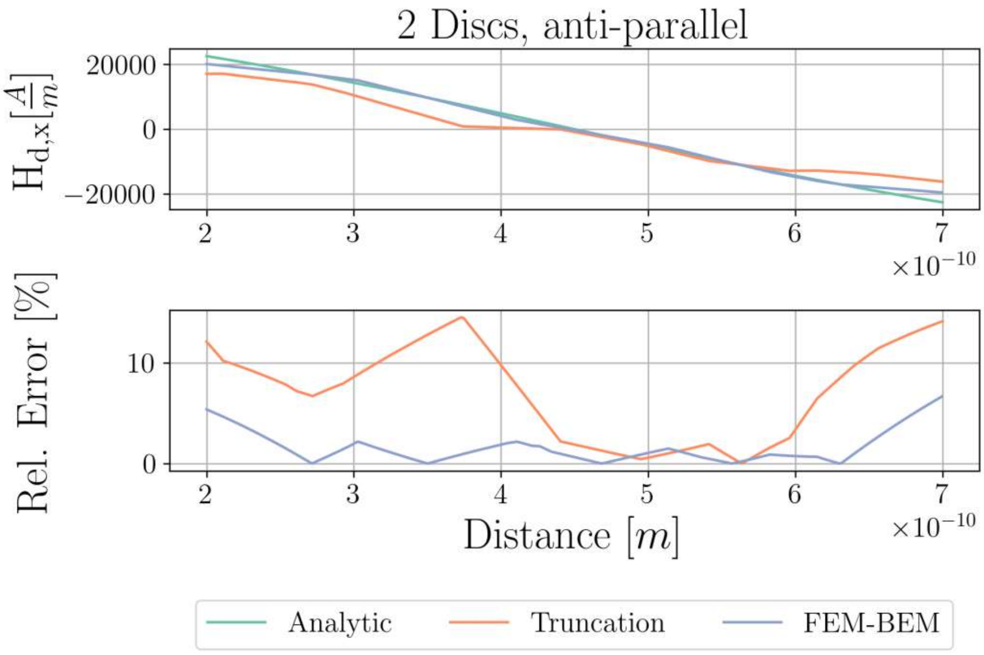

Figure 5.14: Demagnetizing field component along the symmetry axis of two magnetic discs with L=0.1 nm and R=1 nm and antiparallel magnetization. Upper panel: absolute field values. Lower panel: relative error.

5.4 Summary

Due to the long-range interaction of the magnetic moments which are the origin of the demagnetizing field, its calculation is computationally very demanding. Several techniques to cope with this open boundary problem were implemented and analyzed. It was shown that the simple truncation of a nonmagnetic domain surrounding the magnetic domain can be a solution to the problem, but only leads to a large relative error of $\sim$10%. In addition to the relatively large error, computations need to be performed outside the region of interest, i.e. the magnetic regions, which results in a computational penalty.

The FEM-BEM approach on the other hand reduces the computational domain required for the calculation of the demagnetizing field to the magnetic region. Not without sacrifice, though, as the involved matrices are dense and require special treatment. By employing matrix compression algorithms, also this problem can be partially circumvented, reducing the memory consumption and the computational demands of this approach. With the use of 3rd party libraries which provide the BEM as well as the matrix compression capability, a more efficient and, equally important, more accurate approach for the calculation of the demagnetizing field was implemented.

This chapter presented how these two approaches for the calculation of the demagnetizing field work and compared their accuracy. A standard problem as well as problem settings, for which an analytical expression is available, were used to check the validity of the results.

Chapter 6

MRAM Switching Scheme Discovery using Reinforcement Learning

In the beginning, this chapter introduces a recently developed type of SOT-MRAM cell which enables the purely electrical reversal of the free layer magnetization. The challenging task of discovering new, efficient pulse schemes for reliable and deterministic memory cell switching is subsequently shown to be solvable using the machine learning sub-branch of reinforcement learning. The switching performance of a trained RL agent is evaluated by changing various material parameters and is used as a basis to derive a static pulse sequence of which the reliability is tested further.
Extending these results, the introduced ML-based approach is expanded to allow for the optimization of SOT-assisted STT-MRAM cell switching which is then discussed.

6.1 Pulsed SOT-MRAM Cell

As discussed in Section 2.3, one of the biggest challenges of SOT-MRAM devices is that they require special means for guaranteeing deterministic reversal of the magnetization. A simple heavy metal wire attached to the device's free layer producing SOT does not suffice for reliable reversal of the perpendicular magnetization. Additional means which often complicate the fabrication of the device are required. An SOT-MRAM cell first presented in [143] circumvents this issue while requiring no changes to the memory cell structure and maintains purely electrical control of the cell. This special type of SOT-MRAM cell, shown in Fig. 6.1, possesses an additional heavy metal wire orthogonal to the first one. This second wire NM2, however, in contrast to the NM1 wire, is only partially overlapping the free layer and instead of lying below the free layer, it is positioned on top of it. Current pulses can be sent through the NM1 and NM2 wires independently, creating spin-orbit torques interacting with the free layer. It was shown in previous publications that by carefully placing the pulses, the free layer magnetization can be reversed deterministically [143–148].

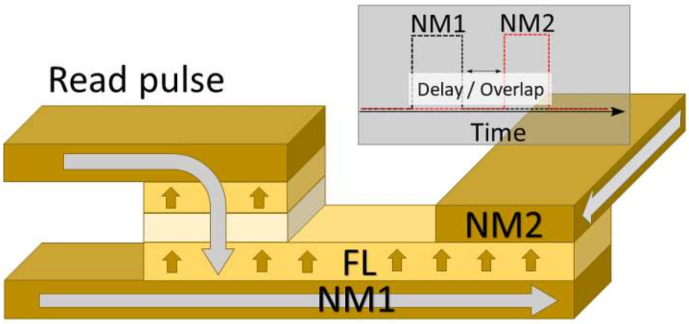

Figure 6.1: SOT-MRAM cell for switching based on two orthogonal current pulses. The pulses are sent through the structure via two non-magnetic heavy metal wires, of which one is fully overlapping the FL (NM1) and one only partially (NM2). This figure was published in [149]

The general idea behind this approach is, that a first pulse through the NM1 wire brings the magnetization towards the plane of the free layer, and a current pulse through the partially overlapping NM2 wire completes the switching and allows for the deterministic reversal of the magnetization [147].

The dynamics of the magnetization in the FL of the pulsed SOT cell are described by the following extended Landau-Lifshitz-Gilbert equation [143]:

$$\begin{aligned}\frac{\partial \mathbf{m}}{\partial t} = &-\gamma\mu_0 \mathbf{m} \times \mathbf{H}_{\mathbf{eff}} + \alpha \mathbf{m} \times \frac{\partial \mathbf{m}}{\partial d} \\ &-\gamma \frac{\hbar}{2e} \frac{\theta_{SH} j_1}{M_S d} \left[\mathbf{m} \times (\mathbf{m} \times \mathbf{y})\right] f_1(t) \\ &+\gamma \frac{\hbar}{2e} \frac{\theta_{SH} j_2}{M_S d} \left[\mathbf{m} \times (\mathbf{m} \times \mathbf{x})\right] f_2(t)\end{aligned} \tag{6.1}$$

Here, $\mathbf{m}$ is the normalized magnetization, γ is the gyromagnetic ratio, μ_0 is the vacuum permeability, α the Gilbert damping factor, M_S is the saturation magnetization. The two terms on the right-hand side of the equation describe the torque generated by the two current pulses through the NM1 and NM2 wires. This torque depends on the effective Hall angle θ_{SH}, the current densities j_1/j_2 through NM1/NM2, the thickness of the FL, d, and the two functions $f_1(t)$ and $f_2(t)$, which define when the current pulses are turned on or off.

Numerous publications have investigated performance and reliability of the memory cell, e.g. [147,148,150–159]. For an investigation of the influence of different pulse widths on the switching behavior of the memory cell shown in Fig. 6.1, a simulation tool based on the finite difference method was used for the numerical solution of (6.1) [120]. However, the equation was adjusted by replacing f_1 and f_2 with the functions $\Lambda_1(t,\ T_1)$ and $\Lambda_2(t,\ T_1,\ T_2)$, respectively. This, allowed for the investigation of the influence of the pulse widths T_1 (NM1) and T_2 (NM2) on the switching behavior of the memory cell. The parameters used for the simulations are given in Table 6.1.

The effective field included the demagnetizing field, the exchange field, the anisotropy field, the current-induced field, and a stochastic thermal field at 300 K. Between the two current pulses, a perfect synchronization was assumed, i.e. immediately after the first pulse is turned off, the second pulse is turned on. The pulse widths T_1 and T_2 were varied from 100 ps to 300 ps and for each simulation configuration 50 realizations were performed to account for the stochasticity of the thermal field. The trajectories of the z-component of the magnetization, averaged over the FL, are shown in Fig. 6.2. One can see that there is a strong influence of the pulse width T_1 on the trajectory of

Table 6.1: Simulation parameters. Heavy metal wires of β-tungsten and a magnetic FL of CoFeB on MgO are assumed.

Parameter	Value
Saturation magnetization, M_S	1.1×10^6 A/m
Perpendicular anisotropy, K	8.4×10^5 J/m^3
Exchange constant, A	1.0×10^{-11} J/m
Gilbert damping factor, α	0.035
Spin Hall angle, θ_{SH}	0.3
Free layer dimensions	40 nm × 20 nm × 1.2 nm
NM1: w_1 x l	20 nm × 3 nm
NM2: w_2 x l	20 nm × 3 nm

the magnetization. When the pulse width is short, either 100 ps or 120 ps, successful magnetization reversal can be achieved. For longer pulse widths T_1, however, the magnetization is not reversed.

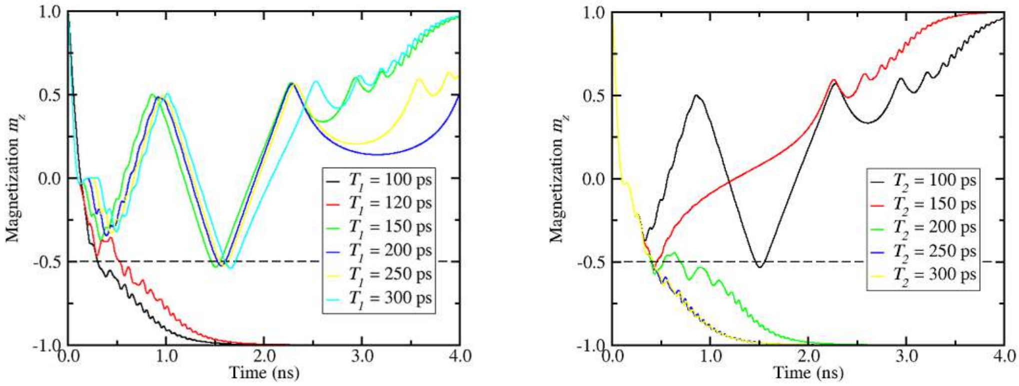

(a) Pulse width T_2 fixed to 200 ps.

(b) Pulse width T_1 fixed to 150 ps.

Figure 6.2: Perpendicular component of the magnetization vector (average of 50 realizations) as a function of time for various durations of the pulses T_1 and T_2, respectively. Simulation parameters as given in Table 6.1, with $j_1 = 2.7 \times 10^{12} A/m^2$, $j_2 = 1.3 \times 10^{12} A/m^2$ and pulse widths being varied from 100 ps to 300 ps. These figures were published in [148].

When fixing the width of the current pulse T_1 and allowing the width of the second pulse, T_2, to vary, the results shown in Fig. 6.2b are obtained. The magnetization is successfully reversed for pulse widths T_2 of 200 ps, 250 ps and 300 ps. To gain a better understanding of the influence of the pulse widths on the switching behavior, simulations for all possible combinations of the previously used pulse widths were performed. The switching probabilities for the various combinations are presented in Fig. 6.3.

The results show that if the pulse T_2 is short, i.e. ≤ 150 ps, the value of T_1 determines, whether reversal can be achieved or not. If, however, T_2 is longer than 200 ps, the exact duration of T_1 becomes less important and the probability of switching tends to 1. For the present investigations, a relatively small set of pulse widths was used. However, when also taking into account the multiple realizations performed per pulse width combination due to the thermal spread, the number of simulations that is required to cover a wider parameter space grows exponentially. An automated approach to find the functions f_1 and f_2 thus is highly desirable. Reinforcement learning can help with discovering novel pulse schemes, which do not just reverse the

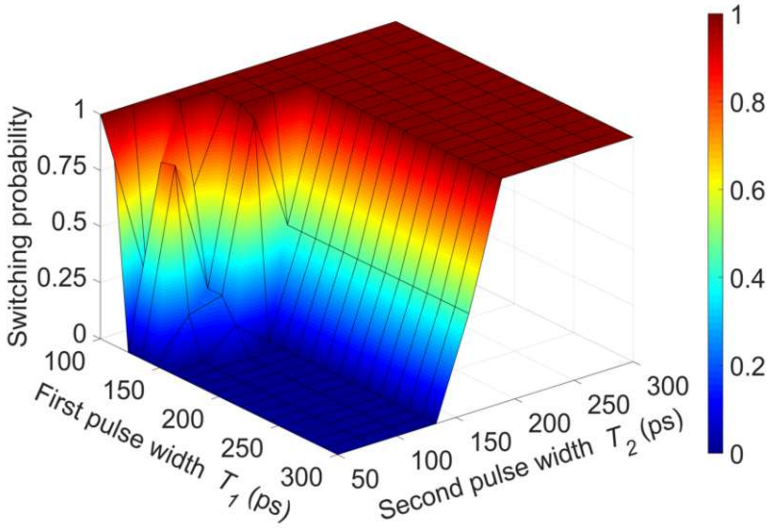

Figure 6.3: Switching probability as a function of the first and the second current pulse widths, T_1, T_2. This figure was published in [148].

magnetization, but also optimize the pulses in order to achieve objectives like fast, reliable, or energy-efficient reversal.

6.2 Reinforcement Learning Setup

In the following, the approach of how to use reinforcement learning for the discovery of novel switching schemes, an idea initially introduced in [160], will be presented.

Figure 6.4 presents the agent-environment system that was used to train an agent to learn how to switch the previously introduced pulsed SOT-MRAM cell. The environment consists of a finite difference simulation of the memory cell. The agent interacts with the environment by controlling the current pulses on the two heavy metal wires. The spin-orbit torque generated thereby acts on the magnetization, causing it to deviate from its current position, which, from the point of view of the RL agent, corresponds to a change of the state vector. State information of the simulation as well as a reward signal are fed back into the agent. A detailed description of the action, state and reward signals will be given in the following sections.

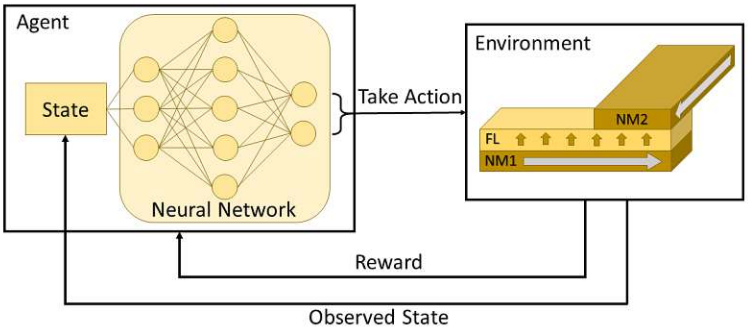

Figure 6.4: General setup of the reinforcement learning approach: A simulation of the SOT-MRAM cell acts as environment which an agent interacts with to build up a policy based on a neural network. This figure was published in [149].

6.2.1 States

The state information that is returned to the agent after every iteration consists of 11 variables. These variables are the average values of the magnetization components $m_{x,y,z}$, the change of the average magnetization components compared to the previous iteration, $\Delta m_{x,y,z}$ the average values of the vector components of the effective magnetic field, $H_{eff_{x,y,z}}$, as well as two variables indicating whether the current pulses through the NM1 and NM2 wires can currently be enabled. It is important to include the change of the magnetization components into the state vector, as otherwise the agent would have no way of telling if and in which direction the magnetization is moving. Before being fed into the neural network the state vector is normalized. With the state vector consisting of 11 variables, this is also the number of nodes of the first layer of the neural network, cf. Fig. 6.7.

6.2.2 Actions

The current pulses on the NM1 and NM2 wires can be in 4 different states: both are turned on, both are turned off, NM1 is off and NM2 is on, and NM1 is on and NM2 is off. This is also the set of actions the RL agent can choose from. The available actions determine the number of nodes in the output layer of the neural network (cf. Fig. 6.7).

However, certain restrictions apply to the control of the current pulses. To avoid that the RL agent turns the pulses on and off arbitrarily fast and to reflect technical limitations of pulse generation, the state of the current pulses through the NM1 and NM2 wire cannot be changed for a time period of 100 ps, limiting the switching frequency to 10 GHz. A visualization of the various pulse configurations can be seen in Fig. 6.5, with the different background shading indicating the different actions.

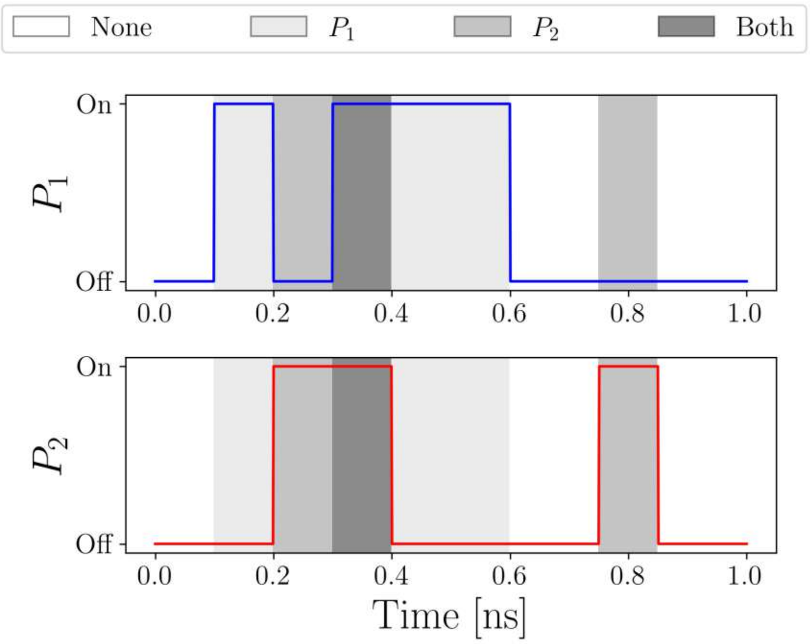

Figure 6.5: Possible pulse combinations under the restriction of a minimum pulse width of 100 *ps*. The different background shadings represent the 4 possible actions.

The amplitude of the current pulses is fixed as well. Previous publications have shown that the critical current for the pulsed SOT-MRAM cell is 120 μA for the NM1 wire [161]. It was also shown that the amplitude for the NM2 wire can lie below this value, while maintaining reliable switching behavior. Based on these results, the current amplitude values for the NM1 and NM2 wire are fixed to 130 μA and 100 μA, respectively.

6.2.3 Rewarding Scheme

As stated previously, the rewarding scheme is one of the most important parts of reinforcement learning algorithms. It encodes the optimization objective and drives the learning of the agent. The objective here is to reverse the z-component of the magnetization from +1 to −1. It shall be discouraged that the magnetization is far away from the target value, but the closer the magnetization gets to the desired state, the better the reward shall be. This was achieved with the following rewarding scheme:

$$r = m_{z,target} - m_{z,current} \tag{6.2}$$

Figure 6.6 shows a visualization of how the reward defined in (6.2) changes with respect to the orientation of the magnetization in the FL.

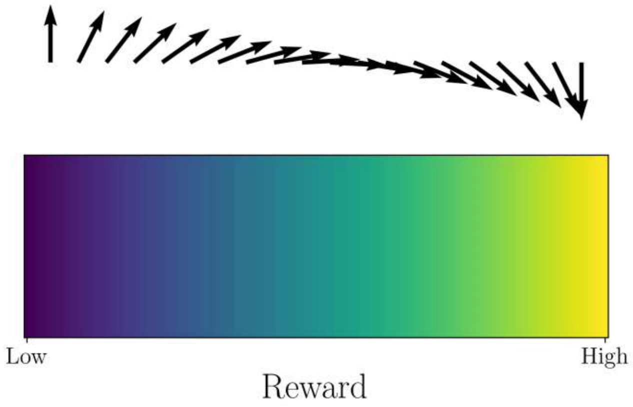

Figure 6.6: Visualization of the reward function with color coding representing the reward returned by (6.2).

This rewarding scheme not only encourages the RL agent to reverse the z-component of the magnetization from +1 to −1, but also to do it fast. As the target value of the z-component of the magnetization is −1, the difference $m_{z,target} - m_{z,current}$ is always negative. However, its value is more negative if the magnetization is further away from the target value than when it is closer. Because it's the agent's aim to maximize its overall accumulated reward, or, phrased differently for the given reward function, minimize the overall accumulated negative reward, it is more favorable for the agent to bring the magnetization towards the target value as fast as possible.

6.2.4 Agent Training

Using the agent-environment setup described in the previous sections, an RL agent was trained to learn how to reverse the magnetization in the FL of a pulsed SOT-MRAM cell described in Section 6.1. The code implementation consists of the RL part implemented in the Python programming language, and the environment part, which is a simulator written in C++ [120]. The Python RL library *Stable Baselines3* [162] provides implementations of the most common RL algorithms and supports the easy creation of custom environments.

Empirically, a dense neural network architecture with input and output layers with dimensions 11 and 4, respectively, as well as two hidden layers with 150 and 100 nodes, has shown to perform well. Table 6.3 gives an overview of the used parameters for the training of the neural network. For parameters not mentioned in the table, the default values of the library were used.

A total of 1×10^6 training steps were performed. To strike the balance between exploitation of existing knowledge about state-action pairs and the exploration of new ones, a linearly decreasing schedule was applied to the ϵ-greedy policy. The schedule starts with an initial value of 1, meaning every choice of action is random and explorative. It then is reduced linearly to a final value of 0.01 over the first 30% of the training time, gradually converging to a more exploitive policy.

Once training of the RL agent is finished, one ideally has a trained neural network model which is able to predict the best action for every possible state the environment can be in. To test the capabilities of the trained agent network, the trained model which is the outcome of the training period, can be loaded again, and switching simulations can be performed with the agent-environment setup. In contrast to the training phase, the reward and state signal which are returned to the agent are only used to predict the next action, but the weights of the neural network remain fixed. From the initial magnetization state with the magnetization uniformly pointing in the posi-

Table 6.2: Environment simulation parameters.

Parameter	Value
Saturation magnetization, M_S	1.1×10^6 A/m
Perpendicular anisotropy, K	8.4×10^5 J/m^3
Exchange constant, A	1.0×10^{-11} J/m
Gilbert damping factor, α	0.035
Spin Hall angle, θ_{SH}	0.3
Free layer dimensions	40 nm × 20 nm × 1.2 nm
NM1: w_1 x l	20 nm × 3 nm
NM2: w_2 x l	20 nm × 3 nm

Table 6.3: DQN algorithm parameters.

Parameter	Value
NN layer dimensions	$11 \times 150 \times 100 \times 4$
Discount factor, γ	0.9997
Learning rate	7.5×10^{-4}
Exploration fraction	0.3
Final exploration probability	0.01
Replay buffer size	3×10^5
Batch size	512

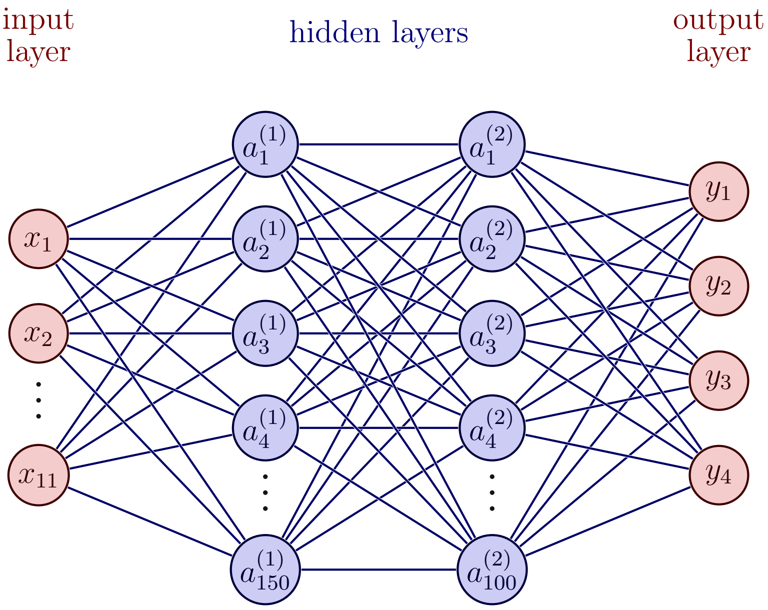

Figure 6.7: Neural network architecture used for the approximation of the Q-function. Input size (11) is determined by the state vector $x_{1\ldots11}$ and output size (4) is determined by the number of possible actions $y_{1\ldots4}$. Internal nodes $a_i^{(l)}$ are numbered according to the layer l they belong to and the node number i within that layer.

tive z direction, the trained agent decides how to apply the pulses. Figure 6.8 shows results of 50 independent realizations in which the trained agent decided about the placement of the pulses. The single plot lines are slightly transparent such that they appear more solid when multiple lines overlap, indicating magnetization trajectories which occurred more often and pulse positions which were applied more frequently. It is immediately apparent, that in all 50 realizations the magnetization was successfully reversed. After around 1700 *ps* most of the magnetization trajectories cross the threshold level of -0.9 at which the magnetization cell is considered to be switched. Looking at the current pulses, another interesting thing can be observed. Only a single NM1 pulse is applied right in the beginning in all the realizations. For the NM2 current pulse, however, there is more variation. After two consecutive pulses in the beginning, a third pulse is applied in all the realizations. The exact position of this third pulse varies, resulting in a slightly blurry appearance of the pulse, due to the transparency of the plot lines.

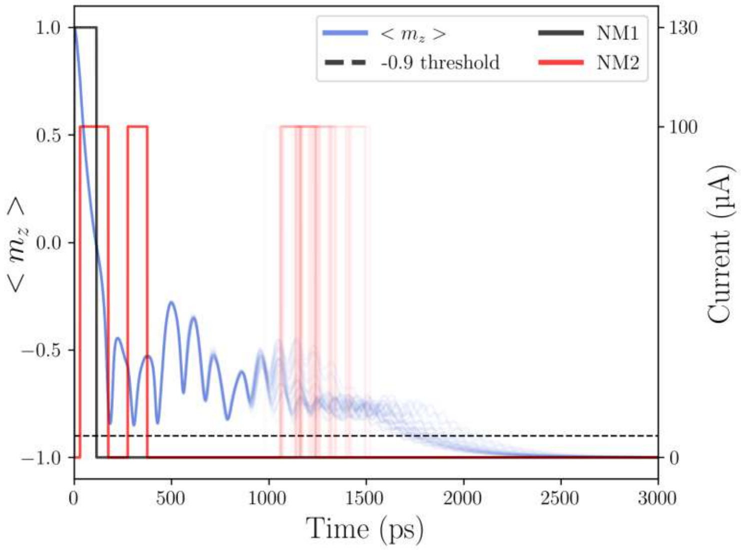

Figure 6.8: Trajectories of the z-component of the magnetization as well as applied NM1 and NM2 pulses of 50 realizations. Lines are plotted slightly transparent, such that regions with more overlapping plot lines appear more solid than regions with less overlapping lines. This figure was published in [163].

As there is also a thermal field contribution, it is to be expected that the magnetization trajectories exhibit a degree of variation. These slightly different trajectories subsequently also lead to the pulses being applied at slightly different points in time. Albeit, it can be seen that the training of the RL agent was successful, and it eventually could deterministically reverse the magnetization of the memory cell.

As already stated, the critical current of the given SOT-MRAM was evaluated to be $130 \mu A$ in [161]. Experiments with a reduced current through the NM1 wire show that the RL agent is still able to achieve deterministic switching, as is shown in Fig. 6.9.

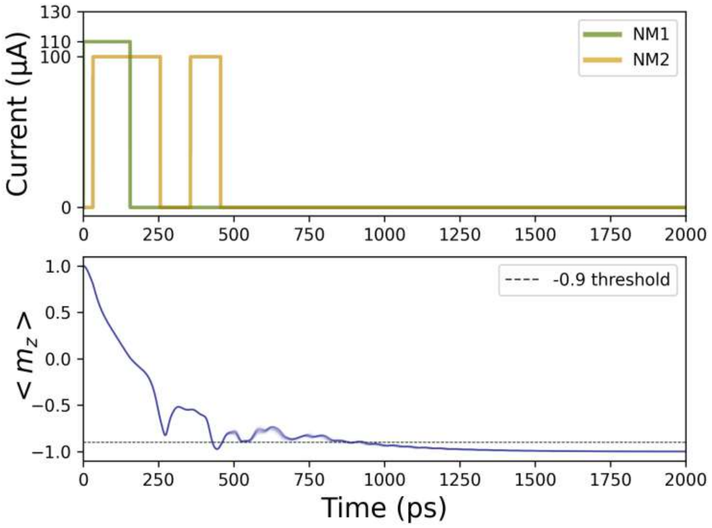

Figure 6.9: Results of 50 realizations for fixed material parameters and an NM1 current value of $110\mu A$ using the learned neural network model. Results of the single runs are plotted slightly transparent, such that regions where multiple lines overlap appear more solid. This figure was published in [149].

The NM1 current was reduced to $110\mu A$, which led the agent to keep the first of the NM2 pulses turned on slightly longer, and, as opposed to the results shown in Fig. 6.8, after the initial two NM2 pulses, no further ones are applied, without detrimental effects on the magnetization dynamics.

6.3 Performance Under Material Parameter Variation

The training phase described in the previous section was performed with a static environment configuration, i.e. an SOT-MRAM cell whose parameter set did not change during training time. This, of course, is an idealized case, as it was shown in [164] that MRAM device manufacturing processes can exhibit material parameter variations of up to 10%. To evaluate how well the agent learned to control the memory cell and to test more realistic scenarios, simulations were performed with varying material parameters. The saturation magnetization M_S and the anisotropy constant K were changed individually up to ±10% from their base values given in Table 6.2, with 1%

increments and a total of 441 realizations were simulated. Figure 6.10 shows the resulting magnetization trajectories (Fig. 6.10a) as well as the percentage of realizations that reached a certain final z-value at the end of the simulation time (Fig. 6.10b).

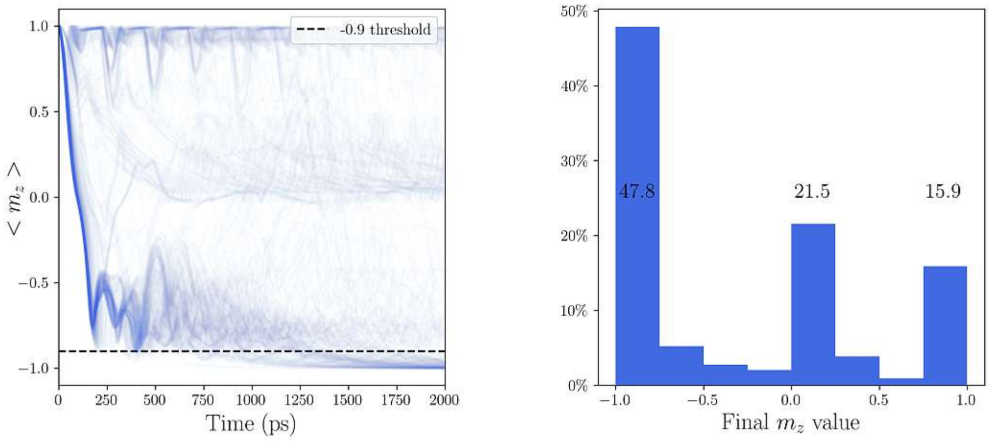

(a) Average z-component of the magnetization for 441 realizations with varying material parameters. Results of the single runs are plotted slightly transparent, such that regions where multiple lines overlap appear more solid.

(b) Histogram showing the percentage of realizations that reached a certain final m_z value.

Figure 6.10: These figures were published in [163].

Each bin in the bar chart of Fig. 6.11 covers a range of 0.25, e.g. from 0.75 to 1. It can be seen that the RL agent manages to bring a large amount, i.e. 47.8% of the magnetization trajectories towards -1. Another peak in the distribution remains close to the initial magnetization value of 1, amounting to 15.9% of the trajectories. The third peak occurs in the region between 0 and 0.25, i.e. where the magnetization is in the xy-plane. Figure 6.11 gives a slightly different view on the results of this experiment. During these experiments, the same setup is used to run switching simulations as was used for training the agent but without changing the weights of the neural network. The action, reward and state signals, however, are still exchanged between agent and environment, and the agents decision is made based on the current state vector. Thus, the agent also continuously accumulates reward, which he tries to maximize and the total accumulated reward at the end of a switching simulation can be seen as a proxy for how good the magnetization in the memory cell could be reversed. The color-coding in Fig. 6.11 represents the total accumulated reward.

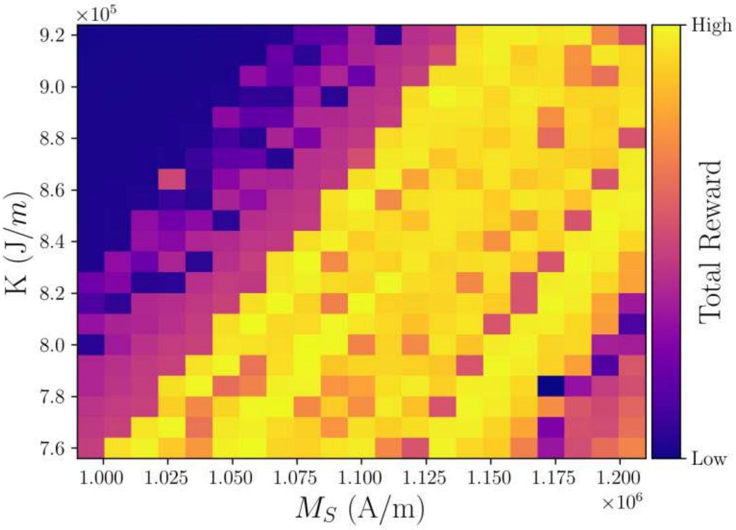

Figure 6.11: Accumulated reward achieved for anisotropy constant K and saturation magnetization MS varied by ±10%. Results are shown for a total of 441 realizations. This figure was published in [163].

Yellow corresponds to a high achieved total reward, while dark blue/purple corresponds to a low total reward. One can clearly see a pattern along the diagonals. The smaller the saturation magnetization and the larger the anisotropy constant, the more the switching performance degrades. This, however, is in line with previous publications that have shown that this regime of saturation magnetization and anisotropy constant exhibits a higher critical current [161]. Thus, for the used current of 130 μA it is not possible to switch the memory cell, which is confirmed by the simulation results.

The performed study demonstrates that the neural network, initially trained under static conditions, exhibits remarkable generalizability when tested against variable parameters typical of MRAM device production. This adaptability is crucial, as it lowers the requirements for the generation of training data, which is a time-consuming process. At the same time, it allows for the exploration of new pulse sequences in a more efficient manner. In practical applications, however, a static pulse sequence is more desirable. The next section presents a method to derive such a sequence from the results achieved with the trained RL agent.

6.4 Static Pulse Sequence Extraction

The previous section presented that a neural network trained with RL can successfully be used to switch a pulsed SOT-MRAM cell. Here, the neural network dynamically adjusts the pulses depending on the current state of the memory cell, allowing for the successful switching of the memory cell over a wide material parameter range. However, for practical purposes, a static pulse sequence would be more desirable. By analyzing the results presented in Fig. 6.10 and Fig. 6.11, a static pulse sequence can be derived. The upper panels of Fig. 6.12a and Fig. 6.12b show the percentage of simulation runs in which the NM1 and NM2 pulse were active at any given point in time during the 2 ns simulation time.

In the heuristic approach presented here, it is considered important to turn a pulse on, if in more than 50% of the simulation runs the respective pulse was active. By setting this threshold, the pulse schemes shown in the lower panels of Fig. 6.12a and Fig. 6.12b were derived.

The final derived pulse sequence consists of a single NM1 pulse, turned on right in the beginning of the simulation with a duration of 100 ps and two NM2 pulses, the first pulse active shortly after the simulation starts and lasting for 143 ps and the second NM2 pulse activated ~ 100 ps after the first NM2 pulse, with a duration of 106 ps. This derived pulse sequence can then again be put under test by first performing switching simulations without changing the material parameters. The results of these simulations are shown in Fig. 6.13.

Again, the magnetization in the memory cell can deterministically be reversed in all realizations. Interestingly, there is less variation between the single magnetization trajectories as compared to the results presented in Fig. 6.8. Further, the time it takes for the trajectories to cross the -0.9 threshold has shifted to ~ 1000 ps, so the time to reverse the magnetization has reduced by ~ 700 ps. Again varying the saturation magnetization and the anisotropy constant, the reliability of this derived pulse scheme can be determined, and the outcome is visualized in Fig. 6.14.

It is immediately apparent that using a static pulse sequence, the behavior is more uniform across the material parameter variation range. As expected, the general pattern remains and the best-performing realizations lie on the diagonal from the bottom left to the top right, and the transition from this region to the top left becomes more abrupt. This can be explained by the fact that with the static pulse sequence after the last pulse is turned off, the

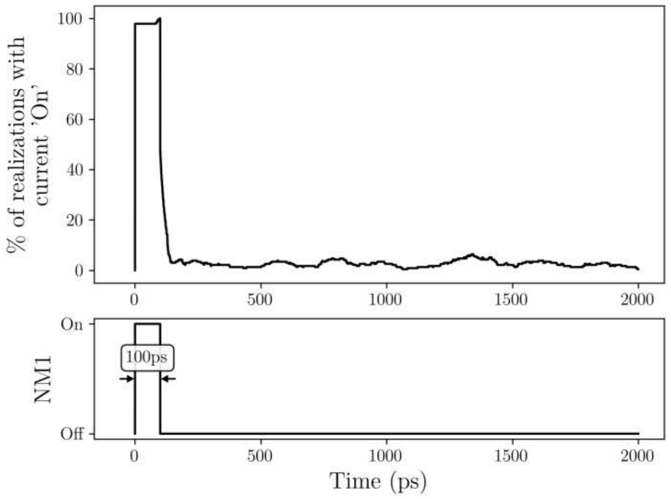

(a) Results for NM1

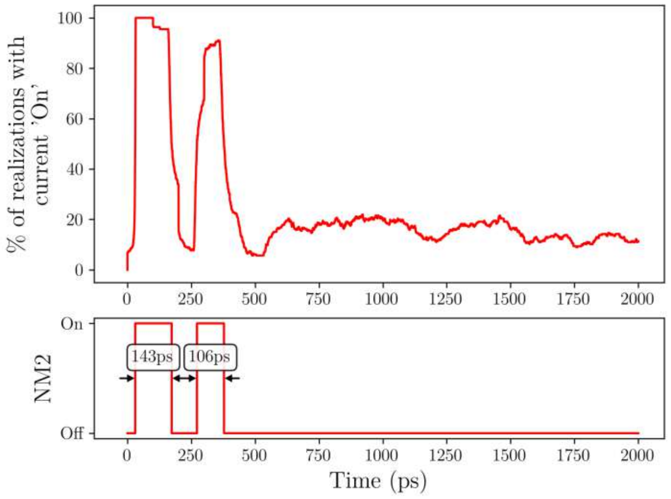

(b) Results for NM2

Figure 6.12: The top panels of (a) and (b) show the percentage of the switching realizations which had the respective pulse turned on at the respective times of the simulation. The bottom panels show the derived static pulse sequences, in which pulses are turned on, if more than 50% of the realizations had the pulse turned on. These figures were published in [163].

magnetization relaxes to the final state, either +1 or −1, but when using the trained RL agent, the agent repeatedly applies pulses to try to bring the magnetization towards −1, accumulating more reward, resulting in a less abrupt transition between the yellow and dark blue/purple regions.

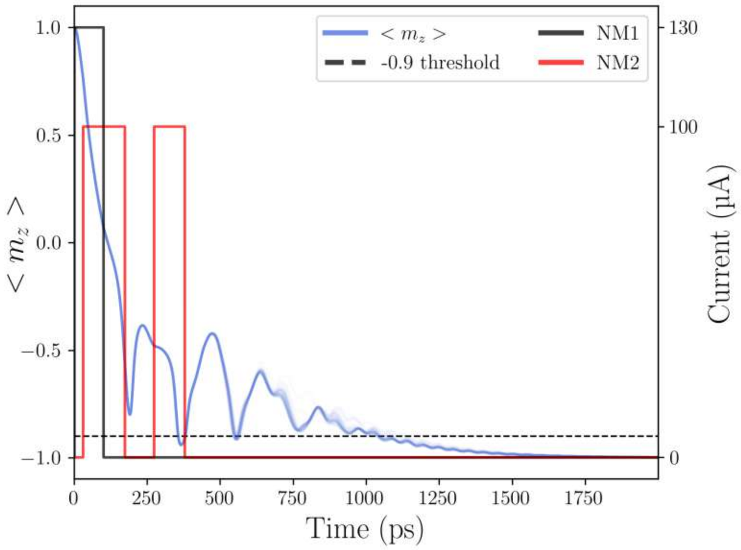

Figure 6.13: Trajectories of the z-component of the magnetization as well as applied NM1 and NM2 pulses of 50 realizations. Lines are plotted slightly transparent, such that regions with more overlapping plot lines appear more solid than regions with less overlapping lines. This figure was published in [163].

Like material parameters, the thickness of the free layer of an MTJ also has significant impact on the switching behavior. Thus, it is further investigated how the derived static pulse sequence performs under variations of the free layer thickness. For this purpose, the base thickness of 1 nm was varied $\pm 10\%$ with 1% increments. For each thickness, five realizations were performed, the results are shown in Fig. 6.15.

Switching time is measured as the time it takes for the z-component of the magnetization to reach the -0.9 threshold. If the free layer thickness is larger than 106% of the base design value, no switching can be achieved anymore (indicated by the red coloring of the circles). It appears, as if there is a sweet spot of free layer thicknesses, for which reversal of the magnetization is easier. Between 1.13 nm and 1.19 nm the switching time is reduced to $\sim 600\ ps$.

As the NM2 wire is shared between neighboring memory cells, every NM2 pulse going through the metal wire is also “experienced” by those. It is thus important to perform an analysis of the switching scheme’s influence on cells adjacent to the targeted cell. Erroneous reversal of other memory cells should

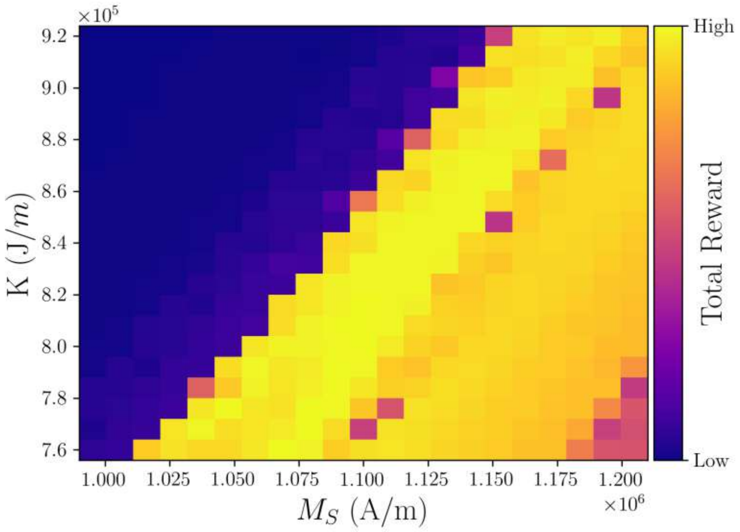

Figure 6.14: Parameter variation with derived pulse sequence. This figure was published in [163].

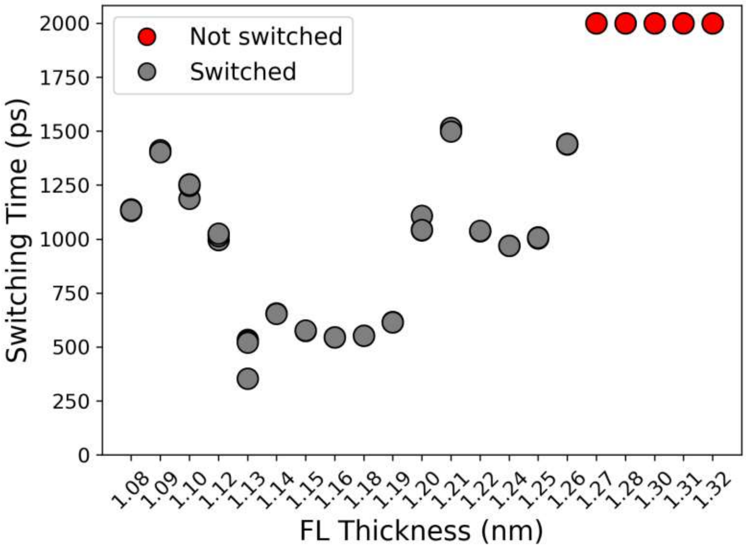

Figure 6.15: Switching times achieved by applying the derived static pulse sequence to FL thickness variations of up to ±10%. This figure was published in [165].

be avoided. In Fig. 6.16 results are presented for performing 50 independent switching realizations to study the influence of the current through NM2 on adjacent cells not targeted for reversal.

The upper panel of Fig. 6.16b shows the applied pulses, i.e. the NM1 pulse being turned off all the time, and the NM2 pulse being active for two short periods of 143 *ps* and 100 *ps*, respectively. The bottom panel shows the resulting displacement of the magnetization from its initial position. It can be seen, that the largest deflection of the magnetization reaches a value of ~ 0.95 and quickly settles back to the initial position. It is thus safe to say, that the impact of the pulse scheme on neighboring memory cells is negligible and does not lead to erroneous magnetization reversals.

6.5 Efficient SOT-Assisted STT-MRAM Switching

As described in Section 2.4, SOT-assisted STT-MRAM is a promising candidate for low power applications. While the procedure for reading of the stored information remains the same as in pure STT- and SOT-MRAM, altering the information in the free layer happens by a combination of STT and SOT. In the following an approach will be presented, how the previously introduced approach to let an ML agent learn to switch a MRAM cell can be used for optimizing SOT-assisted STT-MRAM cell switching for more energy-efficient switching.

Since the type of memory cell changes, also the equation describing the FL dynamics changes to:

$$\frac{\partial \mathbf{m}}{\partial t} = -\gamma\mu_0 \mathbf{m} \times \mathbf{H}_{\text{eff}} + \alpha \mathbf{m} \times \frac{\partial \mathbf{m}}{\partial t} + f_1(t)\mathbf{T}_{\text{SOT}} + f_2(t)\mathbf{T}_{\text{STT}} \tag{6.3}$$

with T_{SOT} being the torque generated the heavy metal wire attached to the FL, $f_1(t)$ being the function defining when the SOT pulse is turned on, T_{STT} being the torque generated by the current running through the MTJ and $f_2(t)$ determining when the STT pulse is active.

The general structure of the RL approach for training an agent to learn to switch an MRAM cell remains the same as described in Section 6.2. The agent is able to perform 4 different actions, but instead of controlling the current through the two orthogonal heavy metal wires, it controls the current

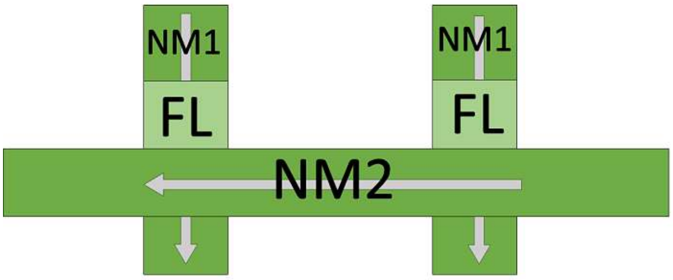

(a) Schematic of cross-bar structure in which the NM2 wire is shared between neighboring memory cells.

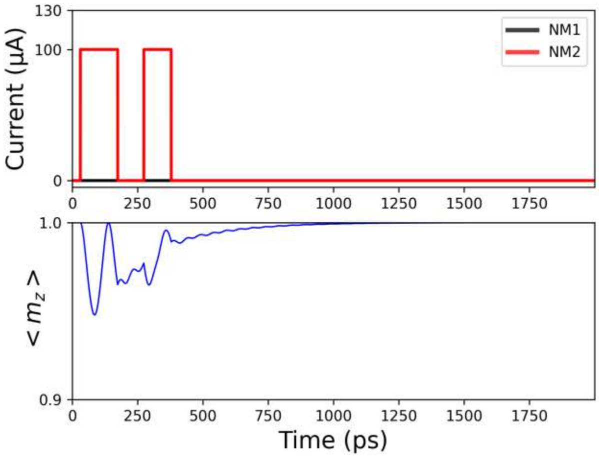

(b) z-component of the magnetization (lower panel) for NM2 pulse as shown in the upper panel.

Figure 6.16: Impact of NM2 pulses on neighboring memory cells in a crossbar architecture. These figures were published in [165]

through one heavy metal wire to create SOT and a current flowing through the MTJ to create STT. The frequency at which the pulse states can be altered remains at 10 GHz, the current for the STT pulse is limited to, while for the SOT pulse a voltage is set, which is fixed to V.

Figure 6.17 shows the trajectory of the averaged magnetization components, the pulses applied by the agent, as well as the accumulated reward over the simulated time.

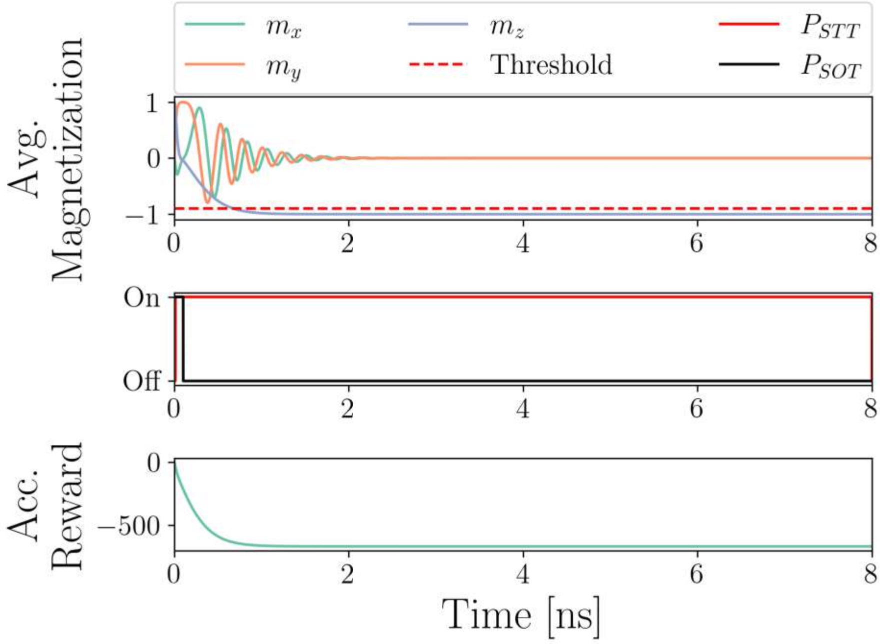

Figure 6.17: Averaged magnetization components (top panel) over a single switching simulation, with pulses applied by the agent (middle panel), leading to an accumulated reward (bottom panel) according to (6.2). This figure was published in [166].

The result presented in Fig. 6.17 highlights the importance of choosing an appropriate rewarding function for the respective application. While the agent achieves reversal of the magnetization, it does so by permanently turning on the STT pulse, which is of no practical use. For learning to switch SOT-assisted STT-MRAM it is thus not enough to employ the rewarding function given in (6.2) and the reward function has to be adjusted. To encourage the agent to turn the pulses off again, the following penalty is introduced:

$$r_{Pulse} = -\left(P_{STT} + P_{SOT}\right) \tag{6.4}$$

With P_{STT}/P_{SOT} being either 1 or 0 when the pulse is turned on or off, respectively. The penalty thus is largest when both pulses are turned on, and zero if they are turned off. Adding this penalty to (6.2) results in the new reward function:

$$r = r_{Pulse} + r_{m_z} \tag{6.5}$$

Figure 6.18 shows a visualization of the reward function given in (6.5). With the reward function (6.5), the reward the agent receives is always negative, unless the average z-component of the magnetization matches the target value and is reversed completely. Additionally, three rewarding regimes can be identified, which are a result of the three different levels of penalizing power consumption. The power consumption is highest when both pulses are turned on, resulting in the most negative reward. The least negative reward occurs when both pulses are turned off. The negative reward in this case stems from the deviation of the FL magnetization from the target value. When only one of the two pulses is turned on, the reward lies between the two aforementioned regimes.

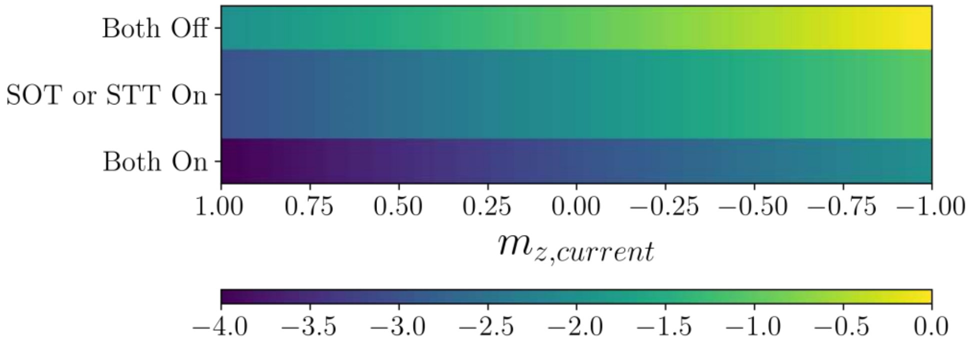

Figure 6.18: Visualization of the reward function with power consumption penalty. Color coding represents the reward returned by (6.4). This figure was published in [166].

Figure 6.19 presents results for a switching simulation, in which an agent trained with reward function (6.5) controls how the SOT and STT pulses are applied. In the middle panel, it is shown how the agent applies the pulses and one can see that, in contrast to Fig. 6.17, the STT pulse is not kept turned on for the whole simulation time, but is removed after 200 *ps*.

This, however, has the additional effect of extending the precessional time of the FL magnetization and increases the switching time from 0.678 ns to 2.76 ns. Looking at the accumulated reward during the simulation, shown in the bottom panel of Fig. 6.19, one can see the transition between rewarding regimes, indicated by the kinks in the accumulated reward.

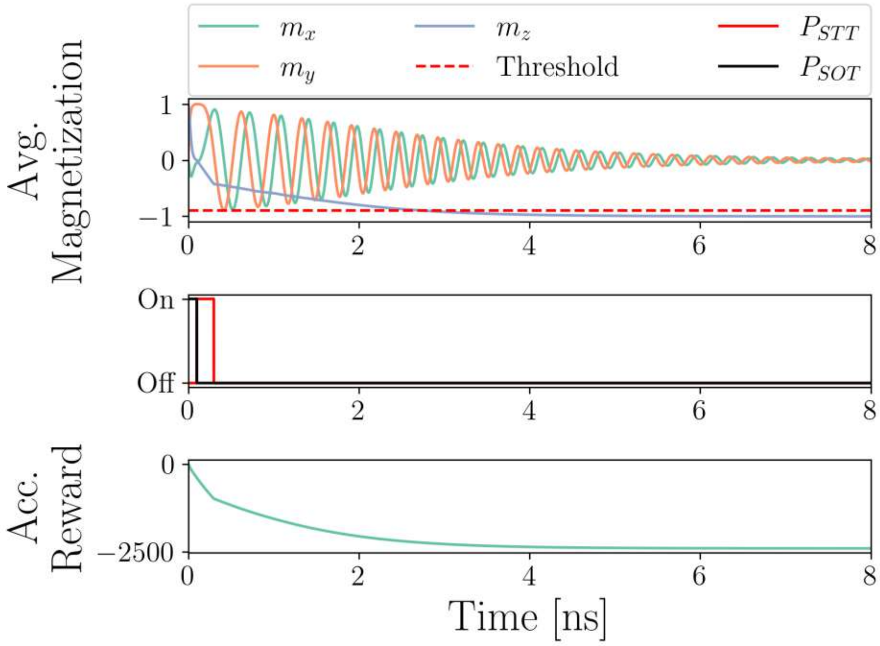

Figure 6.19: Averaged magnetization components (top panel) over a single switching simulation, with pulses applied by the agent (middle panel), leading to an accumulated reward (bottom panel) according to (6.4). This figure was published in [166].

6.6 Summary

The ongoing challenge to achieve deterministic switching in perpendicular SOT-MRAM devices, can be solved by several means. One of these solutions is a recently developed SOT-MRAM cell possessing two orthogonal heavy metal wires attached to the FL, both of which create SOT when a current is sent through. This, however, creates a new challenge of finding suitable sequences of current pulses to be applied to the wires in order to achieve fast and deterministic magnetization reversal.

This chapter introduced a new approach for the discovery of novel switching pulse schemes which uses the machine learning subfield of reinforcement learning for this purpose. It was shown how to use a micromagnetic simulation software in combination with a reinforcement learning framework to successfully train a reinforcement learning agent to efficiently reverse the magnetization in the MRAM cell free layer. Although only being exposed to the simulation environment with a fixed material parameter set, the agent was able to apply its knowledge to before unseen material parameter configurations, while maintaining excellent switching performance.

It was shown that the reinforcement learning approach can be used to optimize for the power consumption in SOT-assisted STT-MRAM devices, highlighting the importance of the choice of rewarding function but at the same time demonstrating the approach's flexibility.

Overall, the performed work demonstrates how reinforcement learning can be a valuable tool for optimizing the control of MRAM devices with respect to varied objectives and can be a good replacement for tedious manual experimentation for finding corresponding switching pulse sequences.

Chapter 7

Summary and Outlook

The increasing difficulty to further scale down CMOS based devices has driven research for the development of alternative, nonvolatile solutions [2]. MRAM devices are promising candidates for universal memory, exhibiting very good endurance and high speed, while at the same time being compatible with CMOS technology. Potential usages range from IoT and automotive applications to the use in last level caches.

In order to reduce development costs, reliable and accurate simulation tools for predicting the devices' behavior are indispensable. For this purpose, many computational approaches exist and are used. The main aim of this thesis was to implement and investigate existing approaches, as well as to develop new ones that may help in driving the development of future MRAM devices forward.

The computational challenges posed by the long-range interaction of the magnetic moments, which are the origin of the demagnetizing field, are the topic of the first part of this work. One approach for its calculation involves truncating a nonmagnetic domain, yielding a 10% relative error and computational penalties beyond the region of interest. Alternatively, the FEM-BEM approach reduces the computational domain to the magnetic region, utilizing matrix compression for efficiency, offering a more accurate and efficient demagnetizing field calculation. Using existing standard problems and analytical expressions, the accuracy of the two presented methods is compared.

By introducing novel computational approaches for MRAM device simulation combining reinforcement learning with micromagnetic simulations, the second part of the thesis addresses the optimization of MRAM switching. The way current pulses are usually applied to switch magnetoresistive memory cells is mostly based on heuristics. This work underscores reinforcement learning's value in MRAM device control, showcasing its efficiency in discovering switching pulse sequences and optimizing various objectives, eliminating the need for manual experimentation. A novel approach is devised, which couples the device simulation to a reinforcement learning agent. This agent autonomously interacts with the simulation, constantly exchanging action signals for state information.

It is shown that an agent trained on a fixed set of parameters is able to transfer the acquired knowledge about the dynamics of the magnetization in the free layer to scenarios with varying environmental conditions. Over a wide range of material parameters, reversal of the free layer magnetization can still be achieved. Further, the approach is extended to SOT-assisted STT-MRAM. By altering the rewarding strategy, the focus of the learned pulse scheme is shifted to different objectives. This is successfully presented, first optimizing for fast magnetization reversal, and then for more energy efficient switching. From the dynamically applied pulses of the reinforcement learning agent, static pulse sequences are condensed, which are shown to perform well over a wide parameter range.

Bibliography

[1] Q. Shao *et al.*, "Roadmap of spin–orbit torques," *IEEE Transactions on Magnetics*, vol. 57, no. 7, pp. 1–39, 2021.

[2] T. Hanyu *et al.*, "Standby-power-free integrated circuits using MTJ-based VLSI computing," *Proceedings of the IEEE*, vol. 104, no. 10, pp. 1844–1863, 2016.

[3] B. Chen *et al.*, "Spintronic devices for high-density memory and neuromorphic computing–A review," *Materials Today*, 2023.

[4] W. Gallagher *et al.*, "22nm STT-MRAM for reflow and automotive uses with high yield, reliability, and magnetic immunity and with performance and shielding options," in *2019 IEEE International Electron Devices Meeting (IEDM)*. IEEE, 2019, pp. 2–7.

[5] S. Sakhare *et al.*, "Enablement of STT-MRAM as last level cache for the high performance computing domain at the 5nm node," in *2018 IEEE International Electron Devices Meeting (IEDM)*. IEEE, 2018, pp. 18–3.

[6] S. Aggarwal *et al.*, "Demonstration of a reliable 1 Gb standalone spin-transfer torque MRAM for industrial applications," in *2019 IEEE International Electron Devices Meeting (IEDM)*. IEEE, 2019, pp. 2–1.

[7] K. Lee *et al.*, "1Gbit high density embedded STT-MRAM in 28nm FDSOI technology," in *2019 IEEE International Electron Devices Meeting (IEDM)*. IEEE, 2019, pp. 2–2.

[8] V. Naik *et al.*, "Manufacturable 22nm FD-SOI embedded MRAM technology for industrial-grade MCU and IOT applications," in *2019 IEEE International Electron Devices Meeting (IEDM)*. IEEE, 2019, pp. 2–3.

[9] J. Alzate *et al.*, "2 MB array-level demonstration of STT-MRAM process and performance towards L4 cache applications," in *2019 IEEE International Electron Devices Meeting (IEDM)*. IEEE, 2019, pp. 2–4.

[10] G. Hu *et al.*, "Spin-transfer torque MRAM with reliable 2 ns writing for last level cache applications," in *2019 IEEE International Electron Devices Meeting (IEDM)*. IEEE, 2019, pp. 2–6.

[11] S. Han *et al.*, "28nm 0.08 mm^2/Mb embedded MRAM for frame buffer memory," in *2020 IEEE International Electron Devices Meeting (IEDM)*. IEEE, 2020, pp. 11–2.

[12] Y.-C. Shih *et al.*, "A reflow-capable, embedded 8Mb STT-MRAM macro with 9ns read access time in 16nm FinFET logic CMOS process," in *2020 IEEE International Electron Devices Meeting (IEDM)*. IEEE, 2020, pp. 11–4.

[13] V. Naik *et al.*, "JEDEC-qualified highly reliable 22nm FD-SOI embedded MRAM for low-power industrial-grade, and extended performance towards automotive-grade-1 applications," in *2020 IEEE International Electron Devices Meeting (IEDM)*. IEEE, 2020, pp. 11–3.

[14] M. Nakayama *et al.*, "14nm High-Performance MTJ with Accelerated STT-Switching and High-Retention Doped Co-Pt Alloy Storage Layer for 1Znm MRAM," in *2023 IEEE International Electron Devices Meeting (IEDM)*, Dec. 2023.

[15] M. Gupta *et al.*, "Ultimate MRAM Scaling: Design Exploration of High-Density, High-Performance and Energy-Efficient VGSOT for Last Level Cache," in *2023 IEEE International Electron Devices Meeting (IEDM)*, Dec. 2023.

[16] K.-S. Li *et al.*, "First BEOL-compatible, 10 ns-fast, and Durable 55 nm Top-pSOT-MRAM with High TMR (>130%)," in *2023 IEEE International Electron Devices Meeting (IEDM)*, Dec. 2023.

[17] Wang Zihui *et al.*, "Dual QSPI 8Gb STT-MRAM For Space Applications," in *2023 IEEE International Electron Devices Meeting (IEDM)*, Dec. 2023.

[18] M. Y. Song *et al.*, "High RA Dual-MTJ SOT-MRAM devices for High Speed (10ns) Compute-in-Memory Applications," in *2023 IEEE International Electron Devices Meeting (IEDM)*, Dec. 2023.

[19] S. Van Beek *et al.*, "Scaling the SOT track – A path towards maximizing efficiency in SOT-MRAM," in *2023 IEEE International Electron Devices Meeting (IEDM)*, Dec. 2023.

[20] H. Suhai, "The First CMOS-Integrated Voltage-Controlled MRAM with 0.7ns Switching Time," in *2023 IEEE International Electron Devices Meeting (IEDM)*, Dec. 2023.

[21] R. B. Goldfarb, B. Dieny, and K.-J. Lee, *Introduction to magnetic random-access memory*. John Wiley & Sons, 2016.

[22] D. Worledge, "Spin flop switching for magnetic random access memory," *Applied Physics Letters*, vol. 84, no. 22, pp. 4559–4561, 2004.

[23] T. L. Gilbert, "A Lagrangian formulation of the gyromagnetic equation of the magnetization field," *Phys. Rev.*, vol. 100, p. 1243, 1955.

[24] T. L. Gilbert, “A phenomenological theory of damping in ferromagnetic materials,” *IEEE transactions on magnetics*, vol. 40, no. 6, pp. 3443–3449, 2004.

[25] J. Leliaert and J. Mulkers, “Tomorrow’s micromagnetic simulations,” *Journal of Applied Physics*, vol. 125, no. 18, 2019.

[26] G. Carleo *et al.*, “Machine learning and the physical sciences,” *Reviews of Modern Physics*, vol. 91, no. 4, p. 045002, 2019.

[27] M. N. Baibich *et al.*, “Giant magnetoresistance of (001) Fe/(001) Cr magnetic superlattices,” *Physical review letters*, vol. 61, no. 21, p. 2472, 1988.

[28] G. Binasch, P. Grünberg, F. Saurenbach, and W. Zinn, “Enhanced magnetoresistance in layered magnetic structures with antiferromagnetic interlayer exchange,” *Physical review B*, vol. 39, no. 7, p. 4828, 1989.

[29] P. Zahn and I. Mertig, “Handbook of Magnetism and Advanced Magnetic Materials, Volume Fundamentals and Theory, Chapter Enhanced Magnetoresistance,” 2007.

[30] M. Julliere, “Tunneling between ferromagnetic films,” *Physics letters A*, vol. 54, no. 3, pp. 225–226, 1975.

[31] S. Bhatti, R. Sbiaa, A. Hirohata, H. Ohno, S. Fukami, and S. Piramanayagam, “Spintronics based random access memory: a review,” *Materials Today*, vol. 20, no. 9, pp. 530–548, 2017.

[32] J.-G. J. Zhu and C. Park, “Magnetic tunnel junctions,” *Materials today*, vol. 9, no. 11, pp. 36–45, 2006.

[33] H. Jaffrès, D. Lacour, F. N. Van Dau, J. Briatico, F. Petroff, and A. Vaurès, “Angular dependence of the tunnel magnetoresistance in transition-metal-based junctions,” *Physical Review B*, vol. 64, no. 6, p. 064427, 2001.

[34] Y. Ji, J. Liu, and C. Yang, “Novel modeling and dynamic simulation of magnetic tunnel junctions for spintronic sensor development,” *Journal of Physics D: Applied Physics*, vol. 50, no. 2, p. 025005, 2016.

[35] T. Miyazaki and N. Tezuka, “Giant magnetic tunneling effect in Fe/Al2O3/Fe junction,” *Journal of magnetism and magnetic materials*, vol. 139, no. 3, pp. L231–L234, 1995.

[36] J. S. Moodera, L. R. Kinder, T. M. Wong, and R. Meservey, “Large magnetoresistance at room temperature in ferromagnetic thin film tunnel junctions,” *Physical review letters*, vol. 74, no. 16, p. 3273, 1995.

[37] D. Wang, C. Nordman, J. M. Daughton, Z. Qian, and J. Fink, “70% TMR at room temperature for SDT sandwich junctions with CoFeB as free and reference layers,” *IEEE Transactions on Magnetics*, vol. 40, no. 4, pp. 2269–2271, 2004.

[38] S. Peng, Y. Zhang, M. Wang, Y. Zhang, and W. Zhao, “Magnetic tunnel junctions for spintronics: Principles and applications,” *Wiley Encyclopedia of Electrical and Electronics Engineering*, pp. 1–16, 1999.

[39] W. H. Butler, X.-G. Zhang, T. C. Schulthess, and J. M. MacLaren, “Spin-dependent tunneling conductance of Fe | MgO | Fe sandwiches,” *Physical Review B*, vol. 63, no. 5, p. 054416, Jan. 2001. doi: 10.1103/PhysRevB.63.054416. . [Online]. Available: https://link.aps.org/doi/10.1103/PhysRevB.63.054416

[40] J. Mathon and A. Umerski, “Theory of tunneling magnetoresistance of an epitaxial Fe/MgO/Fe(001) junction,” *Physical Review B*, vol. 63, no. 22, p. 220403, May 2001. doi: 10.1103/PhysRevB.63.220403. . [Online]. Available: https://link.aps.org/doi/10.1103/PhysRevB.63.220403

[41] S. S. P. Parkin *et al.*, “Giant tunnelling magnetoresistance at room temperature with MgO (100) tunnel barriers,” *Nature Materials*, vol. 3, no. 12, pp. 862–867, Dec. 2004. doi: 10.1038/nmat1256. Number: 12 Publisher: Nature Publishing Group. [Online]. Available: https://www.nature.com/articles/nmat1256

[42] J. Hayakawa, S. Ikeda, F. Matsukura, H. Takahashi, and H. Ohno, “Dependence of Giant Tunnel Magnetoresistance of Sputtered CoFeB/MgO/CoFeB Magnetic Tunnel Junctions on MgO Barrier Thickness and Annealing Temperature,” *Japanese Journal of Applied Physics*, vol. 44, no. 4L, p. L587, Apr. 2005. doi: 10.1143/JJAP.44.L587. Publisher: IOP Publishing. [Online]. Available: https://iopscience.iop.org/article/10.1143/JJAP.44.L587/meta

[43] D. D. Djayaprawira *et al.*, “230% room-temperature magnetoresistance in CoFeB/MgO/CoFeB magnetic tunnel junctions,” *Applied Physics Letters*, vol. 86, no. 9, p. 092502, Feb. 2005. doi: 10.1063/1.1871344. . [Online]. Available: https://doi.org/10.1063/1.1871344

[44] S. Ikeda *et al.*, “Tunnel magnetoresistance of 604% at 300K by suppression of Ta diffusion in CoFeB/MgO/CoFeB pseudo-spin-valves annealed at high temperature,” *Applied Physics Letters*, vol. 93, no. 8, p. 082508, Aug. 2008. doi: 10.1063/1.2976435. . [Online]. Available: https://doi.org/10.1063/1.2976435

[45] L. Xue *et al.*, “Process Optimization of Perpendicular Magnetic Tunnel Junction Arrays for Last-Level Cache beyond 7 nm Node,” in *2018 IEEE Symposium on VLSI Technology*. Honolulu, HI: IEEE, Jun. 2018, pp. 117–118. doi: 10.1109/VLSIT.2018.8510642. . ISBN 978-1-5386-4218-4. [Online]. Available: https://ieeexplore.ieee.org/document/8510642/

[46] S. Ikeda *et al.*, “A perpendicular-anisotropy CoFeB–MgO magnetic tunnel junction,” *Nature materials*, vol. 9, no. 9, pp. 721–724, 2010.

[47] S. Ikeda *et al.*, "Magnetic tunnel junctions for spintronic memories and beyond," *IEEE Transactions on Electron Devices*, vol. 54, no. 5, pp. 991–1002, 2007.

[48] E. Chen *et al.*, "Advances and future prospects of spin-transfer torque random access memory," *IEEE Transactions on Magnetics*, vol. 46, no. 6, pp. 1873–1878, 2010.

[49] J. C. Slonczewski, "Current-driven excitation of magnetic multilayers," *Journal of Magnetism and Magnetic Materials*, vol. 159, no. 1-2, pp. L1–L7, 1996.

[50] L. Berger, "Emission of spin waves by a magnetic multilayer traversed by a current," *Physical Review B*, vol. 54, no. 13, p. 9353, 1996.

[51] D. C. Worledge, "Write-error-rate of spin-transfer-torque mram," in *2023 IEEE International Reliability Physics Symposium (IRPS)*. IEEE, 2023, pp. 1–4.

[52] L. Wu, M. Taouil, S. Rao, E. J. Marinissen, and S. Hamdioui, "Survey on STT-MRAM Testing: Failure Mechanisms, Fault Models, and Tests," Jan. 2020, arXiv:2001.05463 [cs]. [Online]. Available: http://arxiv.org/abs/2001.05463

[53] J. Z. Sun, T. Kuan, J. Katine, and R. H. Koch, "Spin angular momentum transfer in a current-perpendicular spin-valve nanomagnet," in *Quantum Sensing and Nanophotonic Devices*, vol. 5359. SPIE, 2004, pp. 445–455.

[54] D. Apalkov, S. Watts, A. Driskill-Smith, E. Chen, Z. Diao, and V. Nikitin, "Comparison of Scaling of In-Plane and Perpendicular Spin Transfer Switching Technologies by Micromagnetic Simulation," *IEEE Transactions on Magnetics*, vol. 46, no. 6, pp. 2240–2243, Jun. 2010. doi: 10.1109/TMAG.2010.2041330. . [Online]. Available: http://ieeexplore.ieee.org/document/5467399/

[55] L. Su *et al.*, "Current-limiting challenges for all-spin logic devices," *Scientific reports*, vol. 5, no. 1, p. 14905, 2015.

[56] W. Zhao *et al.*, "Failure analysis in magnetic tunnel junction nanopillar with interfacial perpendicular magnetic anisotropy," *Materials*, vol. 9, no. 1, p. 41, 2016.

[57] Z. Guo *et al.*, "Spintronics for energy-efficient computing: An overview and outlook," *Proceedings of the IEEE*, 2021.

[58] B. Tudu and A. Tiwari, "Recent developments in perpendicular magnetic anisotropy thin films for data storage applications," *Vacuum*, vol. 146, pp. 329–341, 2017.

[59] J. Herault *et al.*, "Pulsewidth dependence of barrier breakdown in MgO magnetic tunnel junctions," *IEEE Transactions on Magnetics*, vol. 44, no. 11, pp. 2581–2584, 2008.

[60] M. Schäfers *et al.*, "Electric breakdown in ultrathin MgO tunnel barrier junctions for spin-transfer torque switching," *Applied Physics Letters*, vol. 95, no. 23, 2009.

[61] I. M. Miron *et al.*, "Perpendicular switching of a single ferromagnetic layer induced by in-plane current injection," *Nature*, vol. 476, no. 7359, pp. 189–193, 2011.

[62] L. Liu, C.-F. Pai, Y. Li, H. Tseng, D. Ralph, and R. Buhrman, "Spin-torque switching with the giant spin Hall effect of tantalum," *Science*, vol. 336, no. 6081, pp. 555–558, 2012.

[63] J. Sinova, S. O. Valenzuela, J. Wunderlich, C. Back, and T. Jungwirth, "Spin hall effects," *Reviews of modern physics*, vol. 87, no. 4, p. 1213, 2015.

[64] V. M. Edelstein, "Spin polarization of conduction electrons induced by electric current in two-dimensional asymmetric electron systems," *Solid State Communications*, vol. 73, no. 3, pp. 233–235, 1990.

[65] A. Manchon and S. Zhang, "Theory of nonequilibrium intrinsic spin torque in a single nanomagnet," *Physical Review B*, vol. 78, no. 21, p. 212405, 2008.

[66] V. P. Amin and M. D. Stiles, "Spin transport at interfaces with spin-orbit coupling: Phenomenology," *Physical Review B*, vol. 94, no. 10, p. 104420, Sep. 2016. doi: 10.1103/PhysRevB.94.104420. Publisher: American Physical Society. [Online]. Available: https://link.aps.org/doi/10.1103/PhysRevB.94.104420

[67] A. Manchon and S. Zhang, "Theory of spin torque due to spin-orbit coupling," *Physical Review B*, vol. 79, no. 9, p. 094422, 2009.

[68] P. Gambardella and I. M. Miron, "Current-induced spin–orbit torques," *Philosophical Transactions of the Royal Society A: Mathematical, Physical and Engineering Sciences*, vol. 369, no. 1948, pp. 3175–3197, 2011.

[69] A. Manchon, H. C. Koo, J. Nitta, S. M. Frolov, and R. A. Duine, "New perspectives for Rashba spin–orbit coupling," *Nature materials*, vol. 14, no. 9, pp. 871–882, 2015.

[70] K. Garello *et al.*, "Manufacturable 300mm platform solution for Field-Free Switching SOT-MRAM," in *2019 Symposium on VLSI Circuits*, Jun. 2019, pp. T194–T195. doi: 10.23919/VLSIC.2019.8778100. ISSN: 2158-5636. [Online]. Available: https://ieeexplore.ieee.org/abstract/document/8778100

[71] D. MacNeill, G. M. Stiehl, M. H. D. Guimaraes, R. A. Buhrman, J. Park, and D. C. Ralph, "Control of spin–orbit torques through crystal symmetry in WTe2/ferromagnet bilayers," *Nature Physics*, vol. 13, no. 3, pp. 300–305, Mar. 2017. doi: 10.1038/nphys3933. Number: 3 Publisher: Nature Publishing Group. [Online]. Available: https://www.nature.com/articles/nphys3933

[72] G. Yu *et al.*, “Switching of perpendicular magnetization by spin–orbit torques in the absence of external magnetic fields,” *Nature Nanotechnology*, vol. 9, no. 7, pp. 548–554, Jul. 2014. doi: 10.1038/nnano.2014.94. Number: 7 Publisher: Nature Publishing Group. [Online]. Available: https://www.nature.com/articles/nnano.2014.94

[73] Y.-W. Oh *et al.*, “Field-free switching of perpendicular magnetization through spin–orbit torque in antiferromagnet/ferromagnet/oxide structures,” *Nature Nanotechnology*, vol. 11, no. 10, pp. 878–884, Oct. 2016. doi: 10.1038/nnano.2016.109. Number: 10 Publisher: Nature Publishing Group. [Online]. Available: https://www.nature.com/articles/nnano.2016.109

[74] S. Fukami, C. Zhang, S. DuttaGupta, A. Kurenkov, and H. Ohno, “Magnetization switching by spin-orbit torque in an antiferromagnet-ferromagnet bilayer system,” *Nature Materials*, vol. 15, no. 5, pp. 535–541, May 2016. doi: 10.1038/nmat4566. Number: 5 Publisher: Nature Publishing Group. [Online]. Available: https://www.nature.com/articles/nmat4566

[75] H. Honjo *et al.*, “First demonstration of field-free SOT-MRAM with 0.35 ns write speed and 70 thermal stability under 400° C thermal tolerance by canted SOT structure and its advanced patterning/SOT channel technology,” in *2019 IEEE International Electron Devices Meeting (IEDM)*. IEEE, 2019, pp. 28–5.

[76] K.-S. Lee, S.-W. Lee, B.-C. Min, and K.-J. Lee, “Threshold current for switching of a perpendicular magnetic layer induced by spin Hall effect,” *Applied Physics Letters*, vol. 102, no. 11, p. 112410, 2013, publisher: American Institute of Physics. [Online]. Available: https://doi.org/10.1063/1.4798288

[77] A. van den Brink *et al.*, “Spin-Hall-assisted magnetic random access memory,” *Applied Physics Letters*, vol. 104, no. 1, 2014.

[78] Z. Wang, W. Zhao, E. Deng, J.-O. Klein, and C. Chappert, “Perpendicular-anisotropy magnetic tunnel junction switched by spin-Hall-assisted spin-transfer torque,” *Journal of Physics D: Applied Physics*, vol. 48, no. 6, p. 065001, 2015.

[79] H.-S. P. Wong and S. Salahuddin, “Memory leads the way to better computing,” *Nature nanotechnology*, vol. 10, no. 3, pp. 191–194, 2015.

[80] A. D. Kent and D. C. Worledge, “A new spin on magnetic memories,” *Nature nanotechnology*, vol. 10, no. 3, pp. 187–191, 2015.

[81] J. K. De Brosse, L. Liu, and D. Worledge, “Spin Hall effect assisted spin transfer torque magnetic random access memory,” 2014, uS Patent 8,896,041.

[82] M. Wang *et al.*, “Field-free switching of a perpendicular magnetic tunnel junction through the interplay of spin–orbit and spin-transfer torques,” *Nature electronics*, vol. 1, no. 11, pp. 582–588, 2018.

[83] W. Cai *et al.*, “Sub-ns field-free switching in perpendicular magnetic tunnel junctions by the interplay of spin transfer and orbit torques,” *IEEE Electron Device Letters*, vol. 42, no. 5, pp. 704–707, 2021.

[84] C. Zhang, Y. Takeuchi, S. Fukami, and H. Ohno, “Field-free and sub-ns magnetization switching of magnetic tunnel junctions by combining spin-transfer torque and spin–orbit torque,” *Applied Physics Letters*, vol. 118, no. 9, 2021.

[85] W. F. Brown, “Micromagnetics,” *(No Title)*, 1963.

[86] L. Landau and E. Lifshitz, “On the theory of the dispersion of magnetic permeability in ferromagnetic bodies,” *Phys. Z. Sowjetunion*, vol. 8, p. 153, 1935.

[87] J. D. Jackson, *Classical electrodynamics.* John Wiley & Sons, 2021.

[88] A. Hubert and R. Schäfer, “Magnetic Domains Springer,” *Berlin, Heidelberg, New York, pgs*, vol. 255, 1998.

[89] J. E. Miltat, M. J. Donahue *et al.*, “Numerical micromagnetics: Finite difference methods,” *Handbook of magnetism and advanced magnetic materials*, vol. 2, pp. 742–764, 2007.

[90] G. Finocchio, M. Carpentieri, B. Azzerboni, L. Torres, E. Martinez, and L. Lopez-Diaz, “Micromagnetic simulations of nanosecond magnetization reversal processes in magnetic nanopillar,” *Journal of applied physics*, vol. 99, no. 8, 2006.

[91] G. Finocchio, B. Azzerboni, G. Fuchs, R. Buhrman, and L. Torres, “Micromagnetic modeling of magnetization switching driven by spin-polarized current in magnetic tunnel junctions,” *Journal of applied physics*, vol. 101, no. 6, 2007.

[92] J. L. García-Palacios and F. J. Lázaro, “Langevin-dynamics study of the dynamical properties of small magnetic particles,” *Physical Review B*, vol. 58, no. 22, p. 14937, 1998.

[93] J. Slonczewski, “Currents and torques in metallic magnetic multilayers,” *Journal of magnetism and magnetic materials*, vol. 247, no. 3, pp. 324–338, 2002.

[94] S. Zhang, P. Levy, and A. Fert, “Mechanisms of spin-polarized current-driven magnetization switching,” *Physical review letters*, vol. 88, no. 23, p. 236601, 2002.

[95] M. Chshiev *et al.*, “Analytical description of ballistic spin currents and torques in magnetic tunnel junctions,” *Physical Review B*, vol. 92, no. 10, p. 104422, 2015.

[96] J. C. Slonczewski, “Currents, torques, and polarization factors in magnetic tunnel junctions,” *Physical Review B*, vol. 71, no. 2, p. 024411, 2005.

[97] C. Abert, “Micromagnetics and spintronics: models and numerical methods,” *The European Physical Journal B*, vol. 92, pp. 1–45, 2019.

[98] S. Lepadatu, “Unified treatment of spin torques using a coupled magnetisation dynamics and three-dimensional spin current solver,” *Scientific Reports*, vol. 7, no. 1, p. 12937, 2017.

[99] C. Petitjean, D. Luc, and X. Waintal, “Unified drift-diffusion theory for transverse spin currents in spin valves, domain walls, and other textured magnets,” *Physical review letters*, vol. 109, no. 11, p. 117204, 2012.

[100] P. Graczyk and M. Krawczyk, “Nonresonant amplification of spin waves through interface magnetoelectric effect and spin-transfer torque,” *Scientific Reports*, vol. 11, no. 1, p. 15692, 2021.

[101] P. M. Haney, H.-W. Lee, K.-J. Lee, A. Manchon, and M. D. Stiles, “Current induced torques and interfacial spin-orbit coupling: Semiclassical modeling,” *Physical Review B*, vol. 87, no. 17, p. 174411, 2013.

[102] S. Fiorentini, J. Ender, S. Selberherr, R. De Orio, W. Goes, and V. Sverdlov, “Coupled spin and charge drift-diffusion approach applied to magnetic tunnel junctions,” *Solid-State Electronics*, vol. 186, p. 108103, Dec. 2021. doi: 10.1016/j.sse.2021.108103. . [Online]. Available: https://linkinghub.elsevier.com/retrieve/pii/S0038110121001489

[103] S. Fiorentini *et al.*, “Finite Element Approach for the Simulation of Modern MRAM Devices,” *Micromachines*, vol. 14, no. 5, p. 898, 2023.

[104] S. Fiorentini, “Computation of torques in magnetic tunnel junctions,” Thesis, Technische Universität Wien, 2023. doi: 10.34726/hss.2023.109800. Accepted: 2023-03-03T06:42:32Z. [Online]. Available: https://repositum.tuwien.at/handle/20.500.12708/158338

[105] N. P. Jørstad, S. Fiorentini, W. J. Loch, W. Goes, S. Selberherr, and V. Sverdlov, “Finite element modeling of spin–orbit torques,” *Solid-State Electronics*, vol. 194, p. 108323, Aug. 2022. doi: 10.1016/j.sse.2022.108323. . [Online]. Available: https://www.sciencedirect.com/science/article/pii/S0038110122000958

[106] V. Tsiantos, J. Miles, and B. Middleton, “Stiffness in micromagnetic simulations,” in *16th IMACS World Congress*, 2000, pp. 21–25.

[107] M. Torfeh-Isfahani and E. Della Torre, “Mode pushing and stiff convergent problems,” *IEEE Transactions on Magnetics*, vol. 19, no. 6, pp. 2527–2530, 1983.

[108] E. Della Torre, “Stiff nodes in numerical micromagnetic problems,” *IEEE transactions on magnetics*, vol. 29, no. 6, pp. 2371–2373, 1993.

[109] Z. Guo and E. Della Torre, “Micromagnetic analysis of domain variations in thin films,” *IEEE transactions on magnetics*, vol. 29, no. 6, pp. 2521–2523, 1993.

[110] I. Cimrák, "A survey on the numerics and computations for the Landau-Lifshitz equation of micromagnetism," *Archives of Computational Methods in Engineering*, vol. 15, no. 3, pp. 1–37, 2007.

[111] D. Suess *et al.*, "Time resolved micromagnetics using a preconditioned time integration method," *Journal of Magnetism and Magnetic Materials*, vol. 248, no. 2, pp. 298–311, 2002.

[112] M. d'Aquino, C. Serpico, and G. Miano, "Geometrical integration of Landau–Lifshitz–Gilbert equation based on the mid-point rule," *Journal of Computational Physics*, vol. 209, no. 2, pp. 730–753, 2005.

[113] F. Alouges, "A new finite element scheme for Landau-Lifchitz equations," *Discrete Contin. Dyn. Syst. Ser. S*, vol. 1, no. 2, pp. 187–196, 2008.

[114] F. Alouges, E. Kritsikis, and J.-C. Toussaint, "A convergent finite element approximation for Landau–Lifschitz–Gilbert equation," *Physica B: Condensed Matter*, vol. 407, no. 9, pp. 1345–1349, 2012.

[115] G. Hrkac, C.-M. Pfeiler, D. Praetorius, M. Ruggeri, A. Segatti, and B. Stiftner, "Convergent tangent plane integrators for the simulation of chiral magnetic skyrmion dynamics," *Advances in Computational Mathematics*, vol. 45, pp. 1329–1368, 2019.

[116] C. Abert, L. Exl, F. Bruckner, A. Drews, and D. Suess, "magnum. fe: A micromagnetic finite-element simulation code based on FEniCS," *Journal of Magnetism and Magnetic Materials*, vol. 345, pp. 29–35, 2013.

[117] P. Goldenits, G. Hrkac, D. Praetorius, and D. Süss, "An effective integrator for the Landau-Lifshitz-Gilbert equation," *IFAC Proceedings Volumes*, vol. 45, no. 2, pp. 493–497, 2012.

[118] C. Grossmann, *Numerical treatment of partial differential equations*. Springer, 2007.

[119] H. P. Langtangen and S. Linge, *Finite difference computing with PDEs: a modern software approach*. Springer Nature, 2017.

[120] A. Makarov, "Modeling of Emerging Resistive Switching Based Memory Cells," Ph.D. dissertation, Institut für Mikroelektronik, 2014. doi: 10.34726/hss.2014.23875. . [Online]. Available: http://www.iue.tuwien.ac.at/phd/makarov/

[121] D. Tomáš, "Modelling of micromagnetic structures," Ph.D. dissertation, Ph. D. Thesis (in English), Paris-Sud University, Orsay and Charles . . . , 1999.

[122] Y. Saad, *Iterative methods for sparse linear systems*. SIAM, 2003.

[123] "ViennaMag," https://www.iue.tuwien.ac.at/software/viennamag/, 2024.

[124] R. Anderson *et al.*, "MFEM: A Modular Finite Element Methods Library," *Computers & Mathematics with Applications*, vol. 81, pp. 42–74, 2021. doi: 10.1016/j.camwa.2020.06.009.

[125] L. Graesser and W. L. Keng, *Foundations of deep reinforcement learning: theory and practice in Python.* Addison-Wesley Professional, 2019.

[126] J. Randløv and P. Alstrøm, "Learning to Drive a Bicycle Using Reinforcement Learning and Shaping," Jul. 1998. [Online]. Available: https://www.semanticscholar.org/paper/Learning-to-Drive-a-Bicycle-Using-Reinforcement-and-Randl%C3%B8v-Alstr%C3%B8m/9d8f6219fbd2da14d8d55562dcedf43fe671d0e3?p2df

[127] I. Popov *et al.*, "Data-efficient Deep Reinforcement Learning for Dexterous Manipulation," Apr. 2017, arXiv:1704.03073 [cs]. [Online]. Available: http://arxiv.org/abs/1704.03073

[128] B. Zhang *et al.*, "On the Importance of Hyperparameter Optimization for Model-based Reinforcement Learning," Feb. 2021, arXiv:2102.13651 [cs, eess]. [Online]. Available: http://arxiv.org/abs/2102.13651

[129] B. Ibarz, J. Leike, T. Pohlen, G. Irving, S. Legg, and D. Amodei, "Reward learning from human preferences and demonstrations in Atari," Nov. 2018, arXiv:1811.06521 [cs, stat]. [Online]. Available: http://arxiv.org/abs/1811.06521

[130] G. A. Rummery and M. Niranjan, *On-line Q-learning using connectionist systems.* University of Cambridge, Department of Engineering Cambridge, UK, 1994, vol. 37.

[131] C. J. C. H. Watkins, "Learning from delayed rewards," 1989.

[132] V. Mnih *et al.*, "Playing atari with deep reinforcement learning," *arXiv preprint arXiv:1312.5602*, 2013.

[133] V. Mnih *et al.*, "Human-level control through deep reinforcement learning," *nature*, vol. 518, no. 7540, pp. 529–533, 2015.

[134] R. S. Sutton and A. G. Barto, *Reinforcement learning: An introduction*, 2018.

[135] Q. Chen and A. Konrad, "A review of finite element open boundary techniques for static and quasi-static electromagnetic field problems," *IEEE Transactions on Magnetics*, vol. 33, no. 1, pp. 663–676, 1997.

[136] D. Fredkin and T. Koehler, "Hybrid method for computing demagnetizing fields," *IEEE Transactions on Magnetics*, vol. 26, no. 2, pp. 415–417, 1990.

[137] N. Popović and D. Praetorius, "Applications of $\mathcal{H}$-matrix techniques in micromagnetics," *Computing*, vol. 74, pp. 177–204, 2005.

[138] W. Hackbusch *et al.*, *Hierarchical matrices: algorithms and analysis.* Springer, 2015, vol. 49.

[139] J. Ender *et al.*, "Efficient Demagnetizing Field Calculation for Disconnected Complex Geometries in STT-MRAM Cells," in *Proceedings of the International Conference on Simulation of Semiconductor Processes and Devices (SISPAD)*, 2020, pp. 213–216. doi: 10.23919/SISPAD49475.2020.9241662. Talk: International Conference on Simulation of Semiconductor Processes and Devices (SISPAD), Kobe, Japan - virtual; 2020-09-23 – 2020-10-06. [Online]. Available: http://www.iue.tuwien.ac.at/pdf/ib_2020/CP2020_Ender_1.pdf

[140] N. C. μMag Modeling Group, "Standard problem #3." [Online]. Available: https://www.ctcms.nist.gov/~rdm/spec3.html

[141] C. Abert, L. Exl, G. Selke, A. Drews, and T. Schrefl, "Numerical methods for the stray-field calculation: A comparison of recently developed algorithms," *Journal of Magnetism and Magnetic Materials*, vol. 326, pp. 176–185, 2013.

[142] J. M. Camacho and V. Sosa, "Alternative method to calculate the magnetic field of permanent magnets with azimuthal symmetry," *Revista mexicana de física E*, vol. 59, no. 1, pp. 8–17, 2013.

[143] V. Sverdlov, A. Makarov, and S. Selberherr, "Two-pulse sub-ns switching scheme for advanced spin-orbit torque MRAM," *Solid-State Electronics*, vol. 155, pp. 49–56, 2019.

[144] R. Orio, S. Selberherr, and V. Sverdlov, "Magnetic Field-Free Deterministic Switching of a Perpendicular Magnetic Layer by Spin-Orbit Torques," *Proceedings of SPIE*, vol. 11090, pp. 110 903F–1–110 903F–6, 2019. doi: 10.1117/12.2529119. Invited. [Online]. Available: http://www.iue.tuwien.ac.at/pdf/ib_2019/JB2019_Orio_1.pdf

[145] R. Orio *et al.*, "Efficient Magnetic Field-Free Switching of a Symmetric Perpendicular Magnetic Free Layer for Advanced SOT-MRAM," in *Proceedings of the 2019 Joint International EUROSOI Workshop and International Conference on Ultimate Integration on Silicon (EUROSOI-ULIS)*, J. Lacord and M. Bawedin, Eds. IEEE, 2019, pp. 1–4. ISBN 978-1-7281-1658-7. doi: 10.1109/EUROSOI-ULIS45800.2019.9041920. . [Online]. Available: http://www.iue.tuwien.ac.at/pdf/ib_2019/BC2019_Orio_1.pdf

[146] R. Orio *et al.*, "Robust Magnetic Field-Free Switching of a Perpendicularly Magnetized Free Layer for SOT-MRAM," *Solid-State Electronics*, vol. 168, pp. 107 730–1–107 730–7, 2020. doi: 10.1016/j.sse.2019.107730. . [Online]. Available: http://www.iue.tuwien.ac.at/pdf/ib_2020/JB2020_Orio_2.pdf

[147] R. Orio, A. Makarov, W. Goes, J. Ender, S. Fiorentini, and V. Sverdlov, "Two-Pulse Magnetic Field-Free Switching Scheme for Perpendicular SOT-MRAM with a Symmetric Square Free Layer," *Physica B: Condensed Matter*, vol. 578, p. 411743, 2020. doi: 10.1016/j.physb.2019.411743. . [Online]. Available: http://www.iue.tuwien.ac.at/pdf/ib_2020/JB2020_Orio_1.pdf

[148] R. Orio, J. Ender, S. Fiorentini, W. Goes, S. Selberherr, and V. Sverdlov, "Optimization of a Spin-Orbit Torque Switching Scheme Based on Micromagnetic Simulations and Reinforcement Learning," *Micromachines*, vol. 12, no. 4, p. 443, 2021. doi: 10.3390/mi12040443. . [Online]. Available: https://www.iue.tuwien.ac.at/pdf/ib_2021/JB2021_Orio_2.pdf

[149] J. Ender, R. Orio, S. Fiorentini, S. Selberherr, W. Gös, and V. Sverdlov, "Improving Failure Rates in Pulsed SOT-MRAM Switching by Reinforcement Learning," in *Proceedings of the 32nd European Symposium on the Reliability of Electron Devices, Failure Physics and Analysis*, 2021, pp. 1–4. doi: 10.1016/j.microrel.2021.114231. . ISSN 0026-2714 Talk: European Symposium on Reliability of Electron Devices, Failure Physics and Analysis (ESREF), Bordeaux, France; 2021-10-04 – 2021-10-07. [Online]. Available: https://www.iue.tuwien.ac.at/pdf/ib_2021/CP2021_Ender_06.pdf

[150] R. Orio *et al.*, "Efficient Magnetic Field Free Switching of Symmetric Perpendicular Magnetic Free Layer for Advanced SOT-MRAM," in *Proceedings of the Joint International EUROSOI Workshop and International Conference on Ultimate Integration on Silicon (EUROSOI-ULIS)*, 2019, pp. 152–153. [Online]. Available: http://www.iue.tuwien.ac.at/pdf/ib_2019/CP2019_Orio_3.pdf

[151] R. Orio, A. Makarov, W. Goes, J. Ender, S. Fiorentini, and V. Sverdlov, "Two-Pulse Magnetic Field Free Switching Scheme for Advanced Perpendicular SOT-MRAM," in *Book of Abstracts of the International Symposium on Hysteresis Modeling and Micromagnetics (HMM)*, 2019, p. 34. [Online]. Available: http://www.iue.tuwien.ac.at/pdf/ib_2019/CP2019_Orio_1.pdf

[152] R. Orio *et al.*, "Robust Magnetic Field Free Switching Scheme for Perpendicular Free Layer in Advanced Spin Orbit Torque Magnetoresistive Random Access Memory," in *Book of Abstracts of the International Workshop on Computational Nanotechnology (IWCN)*, 2019, pp. 69–71. ISBN 978-3-9504738-0-3. [Online]. Available: http://www.iue.tuwien.ac.at/pdf/ib_2019/CP2019_Orio_2.pdf

[153] R. Orio, S. Selberherr, and V. Sverdlov, "Magnetic Field-Free Deterministic Switching of a Perpendicular Magnetic Layer by Spin-Orbit Torques," in *Proceedings of SPIE Spintronics*, 2019, pp. 11 090–123. [Online]. Available: http://www.iue.tuwien.ac.at/pdf/ib_2019/CP2019_Sverdlov_5.pdf

[154] R. Orio *et al.*, "Switching Speedup of the Magnetic Free Layer of Advanced SOT-MRAM," in *Proceedings of the European Solid-State Device Research Conference (ESSDERC)*, 2019, pp. 146–149. doi: 10.1109/ESSDERC.2019.8901780. ISSN: 2378-6558. [Online]. Available: http://www.iue.tuwien.ac.at/pdf/ib_2019/CP2019_Orio_4.pdf

[155] R. Orio, S. Selberherr, J. Ender, S. Fiorentini, W. Goes, and V. Sverdlov, “Robustness of the Two-Pulse Switching Scheme for SOT-MRAM,” in *Abstracts of the Workshop on Innovative Nanoscale Devices and Systems (WINDS)*, 2019, pp. 54–55. ISBN 978-0-578-61722-0. [Online]. Available: https://www.iue.tuwien.ac.at/pdf/ib_2019/CP2019_Orio_6.pdf

[156] R. Orio *et al.*, “A Dynamical Approach to Fast and Reliable External Field Free Perpendicular Magnetization Reversal by Spin-Orbit Torques,” in *Proceedings of the IEEE International Electron Devices Meeting (IEDM) Special Poster Session Dedicated to MRAM*, 2019. [Online]. Available: http://www.iue.tuwien.ac.at/pdf/ib_2019/CP2019_Orio_5.pdf

[157] R. Orio, J. Ender, S. Fiorentini, W. Goes, S. Selberherr, and V. Sverdlov, “Reduced Current Spin-Orbit Torque Switching of a Perpendicularly Magnetized Free Layer,” in *Book of Abstracts of the Joint International EUROSOI Workshop and International Conference on Ultimate Integration on Silicon (EUROSOI-ULIS)*, 2020, pp. 123–124. [Online]. Available: http://www.iue.tuwien.ac.at/pdf/ib_2020/CP2020_Orio_2.pdf

[158] R. Orio *et al.*, “Switching of a Perpendicularly Magnetized Free-Layer by Spin-Orbit-Torques with Reduced Currents,” in *Proceedings of the World Multi-Conference on Systemics, Cybernetics and Informatics (WMSCI)*, 2020, pp. 58–61. ISBN 978-1-950492-37-4. [Online]. Available: http://www.iue.tuwien.ac.at/pdf/ib_2020/CP2020_Orio_1.pdf

[159] R. Orio, J. Ender, S. Fiorentini, W. Goes, S. Selberherr, and V. Sverdlov, “Deterministic Spin-Orbit Switching Scheme for an Array of Perpendicular MRAM Cells Suitable for Large Scale Integration,” in *Proceedings of the Trends in Magnetism Conference (TMAG)*, 2021. [Online]. Available: https://www.iue.tuwien.ac.at/pdf/ib_2021/CP2021_Sverdlov_3.pdf

[160] J. Ender, S. Fiorentini, R. Orio, W. Goes, V. Sverdlov, and S. Selberherr, “Emerging CMOS Compatible Magnetic Memories and Logic,” *IEEE Journal of the Electron Devices Society*, vol. 9, pp. 456–463, 2021. doi: 10.1109/JEDS.2021.3066679. Invited. [Online]. Available: https://www.iue.tuwien.ac.at/pdf/ib_2021/JB2021_Ender_1.pdf

[161] R. Orio, J. Ender, S. Fiorentini, W. Goes, S. Selberherr, and V. Sverdlov, “Numerical Analysis of Deterministic Switching of a Perpendicularly Magnetized Spin-Orbit Torque Memory Cell,” *IEEE Journal of the Electron Devices Society*, vol. 9, pp. 61–67, 2021. doi: 10.1109/JEDS.2020.3039544. . [Online]. Available: https://www.iue.tuwien.ac.at/pdf/ib_2021/JB2021_Orio_1.pdf

[162] A. Raffin, A. Hill, A. Gleave, A. Kanervisto, M. Ernestus, and N. Dormann, "Stable-Baselines3: Reliable Reinforcement Learning Implementations," *Journal of Machine Learning Research*, vol. 22, no. 268, pp. 1–8, 2021. [Online]. Available: http://jmlr.org/papers/v22/20-1364.html

[163] J. Ender, R. Orio, S. Fiorentini, S. Selberherr, W. Goes, and V. Sverdlov, "Reinforcement Learning Approach for Deterministic SOT-MRAM Switching," *Proceedings of SPIE*, vol. 11805, pp. 1 180 519–1–1 180 519–8, 2021. doi: 10.1117/12.2593937. Invited. [Online]. Available: https://www.iue.tuwien.ac.at/pdf/ib_2021/JB2021_Ender_2.pdf

[164] J. Song, H. Dixit, B. Behin-Aein, C. H. Kim, and W. Taylor, "Impact of process variability on write error rate and read disturbance in STT-MRAM devices," *IEEE Transactions on Magnetics*, vol. 56, no. 12, pp. 1–11, 2020.

[165] J. Ender, R. Lacerda de Orio, S. Fiorentini, S. Selberherr, W. Goes, and V. Sverdlov, "Reinforcement learning to reduce failures in SOT-MRAM switching," *Microelectronics Reliability*, vol. 135, no. 114570, pp. 1–5, 2022. doi: 10.1016/j.microrel.2022.114570. Invited. [Online]. Available: https://publik.tuwien.ac.at/files/publik_304551.pdf

[166] J. Ender, R. Lacerda de Orio, W. Goes, and V. Sverdlov, "Towards Efficient SOT-assisted STT-MRAM Cell Switching using Reinforcement Learning," 2023, submitted, under review.

List of Publications

Journal Articles

[1] N. Jørstad, S. Fiorentini, **J. Ender**, W. Goes, S. Selberherr, V. Sverdlov, "Micromagnetic modeling of SOT-MRAM dynamics", *PHYSICA B-CONDENSED MATTER*, vol. 676 2024, doi: 10.1016/j.physb.2023.415612

[2] S. Fiorentini, **J. Ender**, S. Selberherr, R. Orio, W. Goes, V. Sverdlov, "Comprehensive evaluation of torques in ultra-scaled MRAM devices", *Solid-State Electronics*, vol. 199 2023, doi: 10.1016/j.sse.2022.108491

[3] S. Fiorentini, M. Bendra, **J. Ender**, R. Orio, W. Goes, S. Selberherr, V. Sverdlov, "Spin and charge drift-diffusion in ultra-scaled MRAM cells", *Scientific Reports*, vol. 12 2022, doi: 10.1038/s41598-022-25586-4

[4] S. Fiorentini, M. Bendra, **J. Ender**, R. Orio, W. Goes, S. Selberherr, V. Sverdlov, "Spin and charge drift-diffusion in ultra-scaled MRAM cells", *Scientific Reports*, vol. 12 2022, doi: 10.1038/s41598-022-25586-4

[5] T. Hadámek, S. Fiorentini, M. Bendra, **J. Ender**, R. Orio, W. Goes, S. Selberherr, V. Sverdlov, "Temperature Increase in STT-MRAM at Writing: A Fully Three-Dimensional Finite Element Approach", *Solid-State Electronics*, vol. 193 2022, doi: 10.1016/j.sse.2022.108269

[6] S. Fiorentini, **J. Ender**, S. Selberherr, W. Goes, V. Sverdlov, "Spin Transfer Torque Evaluation Based on Coupled Spin and Charge Transport: A Finite Element Method Approach", *Journal on Systemics, Cybernetics and Informatics*, vol. 20, pp. 40–44 2022, doi: 10.54808/JSCI.20.04.40

[7] **J. Ender**, R. Orio, S. Fiorentini, S. Selberherr, W. Goes, V. Sverdlov, “Reinforcement learning to reduce failures in SOT-MRAM switching”, *Microelectronics Reliability*, vol. 135 2022, doi: 10.1016/j.microrel.2022.114570

[8] **J. Ender**, R. Orio, S. Fiorentini, S. Selberherr, W. Goes, V. Sverdlov, “Improving failure rates in pulsed SOT-MRAM switching by reinforcement learning”, *Microelectronics Reliability*, vol. 126, pp. 1–5 2021, doi: 10.1016/j.microrel.2021.114231

[9] **J. Ender**, R. Orio, S. Fiorentini, S. Selberherr, W. Goes, V. Sverdlov, “Improving Failure Rates in Pulsed SOT-MRAM Switching by Reinforcement Learning”, *Microelectronics Reliability*, vol. 126 2021, doi: 10.1016/j.microrel.2021.114231

[10] R. Orio, **J. Ender**, S. Fiorentini, W. Goes, S. Selberherr, V. Sverdlov, “Two-Pulse Switching Scheme and Reinforcement Learning for Energy Efficient SOT-MRAM Simulations”, *Solid-State Electronics*, vol. 185 2021, doi: 10.1016/j.sse.2021.108075

[11] S. Fiorentini, **J. Ender**, S. Selberherr, R. Orio, W. Goes, V. Sverdlov, “Coupled Spin and Charge Drift-Diffusion Approach Applied to Magnetic Tunnel Junctions”, *Solid-State Electronics*, vol. 186 2021, doi: 10.1016/j.sse.2021.108103

[12] R. Orio, **J. Ender**, S. Fiorentini, W. Goes, S. Selberherr, V. Sverdlov, “Numerical Analysis of Deterministic Switching of a Perpendicularly Magnetized Spin-Orbit Torque Memory Cell”, *IEEE Journal of the Electron Devices Society*, vol. 9, pp. 61–67 2021, doi: 10.1109/jeds.2020.3039544

[13] **J. Ender**, S. Fiorentini, R. Orio, W. Goes, V. Sverdlov, S. Selberherr, “Emerging CMOS Compatible Magnetic Memories and Logic”, *IEEE Journal of the Electron Devices Society*, vol. 9, pp. 456–463 2021, doi: 10.1109/jeds.2021.3066679

[14] R. Orio, **J. Ender**, S. Fiorentini, W. Goes, S. Selberherr, V. Sverdlov, “Optimization of a Spin-Orbit Torque Switching Scheme Based on Micromagnetic Simulations and Reinforcement Learning”, *Micromachines*, vol. 12 2021, doi: 10.3390/mi12040443

[15] R. Orio, A. Makarov, W. Goes, **J. Ender**, S. Fiorentini, V. Sverdlov, “Two-Pulse Magnetic Field-Free Switching Scheme for Perpendicular SOT-MRAM with a Symmetric Square Free Layer”, *Physica B: Condensed Matter*, vol. 578 2020, doi: 10.1016/j.physb.2019.411743

[16] R. Orio, A. Makarov, S. Selberherr, W. Goes, **J. Ender**, S. Fiorentini, V. Sverdlov, “Robust Magnetic Field-Free Switching of a Perpendicularly Magnetized Free Layer for SOT-MRAM”, *Solid-State Electronics*, vol. 168 2020, doi: 10.1016/j.sse.2019.107730

[17] S. Fiorentini, R. Orio, S. Selberherr, **J. Ender**, W. Goes, V. Sverdlov, “Analysis of Switching Under Fixed Voltage and Fixed Current in Perpendicular STT-MRAM”, *IEEE Journal of the Electron Devices Society*, vol. 8, pp. 1249–1256 2020, doi: 10.1109/jeds.2020.3023577

Book Contributions

[18] S. Fiorentini, R. Orio, S. Selberherr, **J. Ender**, W. Goes, V. Sverdlov, “Influence of Current Redistribution in Switching Models for Perpendicular STT-MRAM”, in *ECS Transactions*, pp. 159–164, 2020, doi: 10.1149/09705.0159ecst

Conference Contributions

[19] R. Orio, A. Makarov, S. Selberherr, W. Goes, **J. Ender**, S. Fiorentini, V. Sverdlov, “Switching Speedup of the Magnetic Free Layer of Advanced SOT-MRAM”, 2019, in *ESSDERC 2019 - 49th European Solid-State Device Research Conference (ESSDERC)*, doi: 10.1109/essderc.2019.8901780

[20] R. Orio, A. Makarov, S. Selberherr, W. Goes, **J. Ender**, S. Fiorentini, V. Sverdlov, “Robust Magnetic Field Free Switching Scheme for Perpendicular Free Layer in Advanced Spin Orbit Torque Magnetoresistive

Random Access Memory", pp. 69–71, 2019, in *Book of Abstracts of the International Workshop on Computational Nanotechnology (IWCN 2019).*

[21] V. Sverdlov, M. Bendra, B. Pruckner, N. Jørstad, T. Hadámek, **J. Ender**, R. Orio, W. Goes, "Spin and Charge Transport in Ultra-Scaled MRAM Cells", pp. 55–55, 2023, in *Proceedings of the International Conference Micro- and Nanoelectronics (ICMNE)*, doi: 10.29003/m3563.ICMNE-2023

[22] V. Sverdlov, M. Bendra, S. Fiorentini, **J. Ender**, R. Orio, T. Hadámek, W. Loch, N. Jørstad, W. Goes, S. Selberherr, "Advanced Modeling of Emerging Magneto-resistive Memory", pp. 78–79, 2022, in *NANOMEET 2022 2nd International Meet & Expo on Nanotechnology.*

[23] V. Sverdlov, M. Bendra, S. Fiorentini, **J. Ender**, R. Orio, T. Hadámek, W. Loch, N. Jørstad, W. Goes, S. Selberherr, "Advanced Modeling of Emerging Devices for Digital Spintronics", pp. 40–40, 2022, in *2nd International Conference on Nanoscience and Nanotechnology.*

[24] N. Jørstad, T. Hadámek, M. Bendra, **J. Ender**, B. Pruckner, W. Goes, V. Sverdlov, "Numerical Simulations of Spintronic Magnetoresistive Memories", pp. 1–1, 2023, in *SURGE Virtual Event North America 2023: Agenda.*

[25] N. Jørstad, S. Fiorentini, **J. Ender**, R. Orio, T. Hadámek, W. Loch, M. Bendra, W. Goes, S. Selberherr, V. Sverdlov, "Finite Element Modeling of Spin-Orbit Torques", pp. 1–2, 2022, in *Proceedings of the Joint International EuroSOI Workshop and International Conference on Ultimate Integration on Silicon (EuroSOI-ULIS 2022)).*

[26] T. Hadámek, M. Bendra, S. Fiorentini, **J. Ender**, R. Orio, W. Goes, S. Selberherr, V. Sverdlov, "Temperature Increase in MRAM at Writing: A Finite Element Approach", 2021, in *Book of Abstracts of the Joint International EUROSOI Workshop and International Conference on Ultimate Integration on Silicon (EUROSOI-ULIS).*

[27] S. Fiorentini, M. Bendra, **J. Ender**, T. Hadámek, W. Loch, N. Jørstad, R. Orio, W. Goes, S. Selberherr, V. Sverdlov, "Modeling Advanced Spintronic Based Magnetoresistive Memory", pp.

49–52, 2022, in *International Conference on Microwave & THz Technologies, Wireless Communications and OptoElectronics (IRPhE 2022)*, doi: 10.1049/icp.2022.2795

[28] M. Bendra, S. Fiorentini, T. Hadámek, N. Jørstad, **J. Ender**, R. Orio, S. Selberherr, W. Goes, V. Sverdlov, “Switching Composite Free Layers in Ultra-Scaled MRAM Cells”, pp. 184–185, 2023, in *22nd International Winterschool - New Developments in Solid State Physics - Abstract Book*.

[29] M. Bendra, S. Fiorentini, **J. Ender**, R. Orio, T. Hadámek, N. Jørstad, B. Pruckner, S. Selberherr, W. Goes, V. Sverdlov, “Back-Hopping in Ultra-Scaled MRAM Cells”, pp. 159–162, 2023, in *Proceedings of the International Convention MIPRO*, doi: 10.23919/MIPRO57284.2023.10159764

[30] V. Sverdlov, W. Loch, M. Bendra, S. Fiorentini, **J. Ender**, R. Orio, T. Hadámek, N. Jørstad, W. Goes, S. Selberherr, “Modeling Approach to Ultra-Scaled MRAM Cells”, pp. 7–8, 2022, in *Book of Abstracts of the International Meet On Applied Science, Engineering and Technology (ASETMEET)*.

[31] T. Hadámek, M. Bendra, S. Fiorentini, **J. Ender**, R. Orio, W. Goes, S. Selberherr, V. Sverdlov, “Temperature increase in STT-MRAM at writing: A fully three-dimensional finite element approach”, 2021, in *2021 Joint International EUROSOI Workshop and International Conference on Ultimate Integration on Silicon (EUROSOI-ULIS’2021)*, doi: 10.1109/EuroSOI-ULIS53016.2021.9560669

[32] **J. Ender**, R. Orio, W. Goes, V. Sverdlov, “Towards Efficient SOT-assisted STT-MRAM Cell Switching using Reinforcement Learning”, 2024, in *Large-Scale Scientific Computing*, submitted, under review.

[33] S. Fiorentini, R. Orio, W. Goes, **J. Ender**, V. Sverdlov, “Comprehensive Comparison of Switching Models for Perpendicular Spin-Transfer Torque MRAM Cells”, 2019, in *2019 International Conference on Simulation of Semiconductor Processes and Devices (SISPAD)*, doi: 10.1109/sispad.2019.8870359

[34] R. Orio, S. Selberherr, **J. Ender**, S. Fiorentini, W. Goes, V. Sverdlov, “Robustness of the Two-Pulse Switching Scheme for SOT-MRAM”, pp. 54–55, 2019, in *Abstracts of the Workshop on Innovative Nanoscale Devices and Systems (WINDS)*.

[35] R. Orio, A. Makarov, **J. Ender**, S. Fiorentini, W. Goes, S. Selberherr, V. Sverdlov, “A Dynamical Approach to Fast and Reliable External Field Free Perpendicular Magnetization Reversal by Spin-Orbit Torques”, 2019, in *Proceedings of the IEEE International Electron Devices Meeting (IEDM) Special Poster Session Dedicated to MRAM.*

[36] S. Fiorentini, R. Orio, S. Selberherr, **J. Ender**, W. Goes, V. Sverdlov, “Comprehensive Modeling of Switching in Perpendicular STT-MRAM”, pp. 107–108, 2019, in *Abstracts of the Workshop on Innovative Nanoscale Devices and Systems (WINDS).*

[37] R. Orio, A. Makarov, S. Selberherr, W. Goes, **J. Ender**, S. Fiorentini, V. Sverdlov, “Efficient Magnetic Field Free Switching of Symmetric Perpendicular Magnetic Free Layer for Advanced SOT-MRAM”, pp. 152–153, 2019, in *Proceedings of the Joint International EUROSOI Workshop and International Conference on Ultimate Integration on Silicon (EUROSOI-ULIS).*

[38] R. Orio, A. Makarov, W. Goes, **J. Ender**, S. Fiorentini, V. Sverdlov, “Two-Pulse Magnetic Field Free Switching Scheme for Advanced Perpendicular SOT-MRAM”, 2019, in *Book of Abstracts of the International Symposium on Hysteresis Modeling and Micromagnetics (HMM).*

[39] S. Fiorentini, **J. Ender**, M. Mohamedou, R. Orio, S. Selberherr, W. Goes, V. Sverdlov, “Computation of Torques in Magnetic Tunnel Junctions through Spin and Charge Transport Modeling”, 2020, in *2020 International Conference on Simulation of Semiconductor Processes and Devices (SISPAD)*, doi: 10.23919/sispad49475.2020.9241657

[40] S. Fiorentini, R. Orio, S. Selberherr, **J. Ender**, W. Goes, V. Sverdlov, “Influence of Current Redistribution in Switching Models for Perpendicular STT-MRAM”, pp. 1389–1389, 2020, in *ECS Meeting Abstracts*, doi: 10.1149/ma2020-01241389mtgabs

[41] **J. Ender**, M. Mohamedou, S. Fiorentini, R. Orio, S. Selberherr, W. Goes, V. Sverdlov, “Efficient Demagnetizing Field Calculation for Disconnected Complex Geometries in STT-MRAM Cells”, 2020, in *2020 International Conference on Simulation of Semiconductor Processes and Devices (SISPAD)*, doi: 10.23919/sispad49475.2020.9241662

[42] R. Orio, **J. Ender**, S. Fiorentini, W. Goes, S. Selberherr, V. Sverdlov, “Reduced Current Spin-Orbit Torque Switching of a Perpendicularly

Magnetized Free Layer”, 2020, in *2020 Joint International EUROSOI Workshop and International Conference on Ultimate Integration on Silicon (EUROSOI-ULIS)*, doi: 10.1109/eurosoi-ulis49407.2020.9365283

[43] S. Fiorentini, **J. Ender**, M. Mohamedou, S. Selberherr, R. Orio, W. Goes, V. Sverdlov, “Comprehensive Modeling of Coupled Spin-Charge Transport and Magnetization Dynamics in STT-MRAM Cells”, pp. 50–56, 2020, in *Spintronics XIII*, doi: 10.1117/12.2567480

[44] S. Fiorentini, **J. Ender**, S. Selberherr, R. Orio, W. Goes, V. Sverdlov, “Comprehensive Modeling of Coupled Spin and Charge Transport through Magnetic Tunnel Junctions”, 2020, in *2020 Joint International EUROSOI Workshop and International Conference on Ultimate Integration on Silicon (EUROSOI-ULIS)*, doi: 10.1109/eurosoi-ulis49407.2020.9365497

[45] V. Sverdlov, S. Fiorentini, **J. Ender**, W. Goes, R. Orio, S. Selberherr, “Emerging CMOS Compatible Magnetic Memories and Logic”, 2020, in *2020 IEEE Latin America Electron Devices Conference (LAEDC)*, doi: 10.1109/laedc49063.2020.9073332

[46] S. Fiorentini, **J. Ender**, R. Orio, S. Selberherr, W. Goes, V. Sverdlov, “Spin and Charge Drift-Diffusion Approach to Torque Computation in Magnetic Tunnel Junctions”, 2021, in *2021 International Conference on Simulation of Semiconductor Processes and Devices (SISPAD)*, doi: 10.1109/sispad54002.2021.9592559

[47] S. Fiorentini, R. Orio, S. Selberherr, **J. Ender**, W. Goes, V. Sverdlov, “Perpendicular STT-MRAM Switching at Fixed Voltage and at Fixed Current”, 2020, in *2020 4th IEEE Electron Devices Technology & Manufacturing Conference (EDTM)*, doi: 10.1109/edtm47692.2020.9117985

[48] R. Orio, A. Makarov, W. Goes, **J. Ender**, S. Fiorentini, S. Selberherr, V. Sverdlov, “Switching of a Perpendicularly Magnetized Free-Layer by Spin-Orbit-Torques with Reduced Currents”, pp. 58–61, 2020, in *Proceedings of the World Multi-Conference on Systemics, Cybernetics and Informatics (WMSCI)*.

[49] **J. Ender**, R. Orio, S. Fiorentini, S. Selberherr, W. Goes, V. Sverdlov, “Reinforcement Learning Approach for Sub-Critical Current SOT-MRAM Switching”, 2021, in *2021 International Conference on Simulation of Semiconductor Processes and Devices (SISPAD)*, doi: 10.1109/sispad54002.2021.9592561

[50] S. Fiorentini, R. Orio, S. Selberherr, **J. Ender**, W. Goes, V. Sverdlov, “Spin and Charge Drift-Diffusion Approach to Torque Computation in Spintronic Devices”, pp. 12–13, 2021, in *WINDS Book of Abstracts*.

[51] **J. Ender**, R. Orio, S. Fiorentini, S. Selberherr, W. Goes, V. Sverdlov, “Reinforcement Learning Approach for Deterministic SOT-MRAM Switching”, pp. 1180519–1–1180519–8, 2021, in *Spintronics XIV*, doi: 10.1117/12.2593937

[52] S. Fiorentini, **J. Ender**, R. Orio, S. Selberherr, W. Goes, V. Sverdlov, “Spin Drift-Diffusion Approach for the Computation of Torques in Multi-Layered Structures”, pp. 51–52, 2021, in *Book of Abstracts of the International Workshop on Computational Nanotechnology (IWCN 2021)*.

[53] S. Fiorentini, M. Bendra, **J. Ender**, R. Orio, S. Selberherr, W. Goes, V. Sverdlov, “Spin and Charge Drift-Diffusion in Ultra-Scaled MRAM Cells”, 2021, in *Proceedings of the IEEE International Electron Devices Meeting (IEDM) Special Poster Session Dedicated to MRAM*, doi: 10.21203/rs.3.rs-1915307/v1

[54] M. Bendra, **J. Ender**, S. Fiorentini, T. Hadámek, R. Orio, W. Goes, S. Selberherr, V. Sverdlov, “Finite Element Method Approach to MRAM Modeling”, 2021, in *2021 44th International Convention on Information, Communication and Electronic Technology (MIPRO)*, doi: 10.23919/mipro52101.2021.9597194

[55] **J. Ender**, R. Orio, S. Fiorentini, S. Selberherr, W. Goes, V. Sverdlov, “Reinforcement Learning to Reduce Failures in SOT-MRAM Switching”, 2021, in *2021 IEEE International Symposium on the Physical and Failure Analysis of Integrated Circuits (IPFA)*, doi: 10.1109/ipfa53173.2021.9617362

[56] **J. Ender**, S. Fiorentini, R. Orio, T. Hadámek, M. Bendra, W. Goes, S. Selberherr, V. Sverdlov, “Advanced Modeling of Emerging MRAM: From Finite Element Methods to Machine Learning Approaches”, 2021, in *Proceedings of the International Conference Micro- and Nanoelectronics (ICMNE)*.

[57] **J. Ender**, R. Orio, V. Sverdlov, “Enhancing SOT-MRAM Switching Using Machine Learning”, 2021, in *Proceedings of the Silvaco Users Global Event (SURGE)*.

[58] **J. Ender**, R. Orio, S. Fiorentini, S. Selberherr, W. Goes, V. Sverdlov, "Improving failure rates in pulsed SOT-MRAM switching by reinforcement learning", pp. 114231, 2021, in *Microelectronics Reliability*, doi: 10.1016/j.microrel.2021.114231

[59] **J. Ender**, S. Fiorentini, S. Selberherr, W. Goes, V. Sverdlov, "Advanced Modeling of Emerging Nonvolatile Magnetoresistive Devices", pp. 45–46, 2021, in *Book of Abstracts of the International Workshop on Computational Nanotechnology (IWCN 2021)*.

[60] R. Orio, **J. Ender**, S. Fiorentini, W. Goes, S. Selberherr, V. Sverdlov, "Deterministic Spin-Orbit Switching Scheme for an Array of Perpendicular MRAM Cells Suitable for Large Scale Integration", 2021, in *Proceedings of the Trends in Magnetism Conference (TMAG)*.

[61] V. Sverdlov, M. Bendra, S. Fiorentini, **J. Ender**, R. Orio, T. Hadámek, W. Loch, N. Jørstad, W. Goes, S. Selberherr, "Emerging Devices for Digital Spintronics", pp. 32–33, 2022, in *2nd Global Conference & Expo on Nanotechnology & Nanoscience*.

[62] R. Orio, **J. Ender**, W. Goes, S. Fiorentini, S. Selberherr, V. Sverdlov, "About the Switching Energy of a Magnetic Tunnel Junction determined by Spin-Orbit Torque and Voltage-Controlled Magnetic Anisotropy", 2022, in *2022 IEEE Latin American Electron Devices Conference (LAEDC)*, doi: 10.1109/laedc54796.2022.9908222

[63] S. Fiorentini, **J. Ender**, R. Orio, S. Selberherr, W. Goes, V. Sverdlov, "Comprehensive Evaluation of Torques in Ultra Scaled MRAM Devices", pp. 11–12, 2022, in *SISPAD 2022: International Conference on Simulation of Semiconductor Processes and Devices - Conference Abstract Booklet*.

[64] S. Fiorentini, M. Bendra, **J. Ender**, R. Orio, W. Goes, S. Selberherr, V. Sverdlov, "Spin Torques in ULTRA-Scaled MRAM Devices", pp. 348–351, 2022, in *Proceedings of the European Solid-State Device Research Conference (ESSDERC)*.

[65] V. Sverdlov, M. Bendra, S. Fiorentini, **J. Ender**, R. Orio, T. Hadámek, W. Loch, N. Jørstad, W. Goes, S. Selberherr, "Modeling Advanced Spintronic Based Magnetoresistive Memory", 2022, in *International Conference on Microwave & THz Technologies, Wireless Communications and OptoElectronics (IRPhE 2022)*, doi: 10.1049/icp.2022.2795

[66] S. Fiorentini, W. Loch, M. Bendra, N. Jørstad, **J. Ender**, R. Orio, T. Hadámek, W. Goes, V. Sverdlov, S. Selberherr, "Design Analysis of Ultra-Scaled MRAM Cells", 2022, in *Proceedings of 2022 IEEE 16th International Conference on Solid-State & Integrated Circuit Technology (ICSICT).*

[67] M. Bendra, S. Fiorentini, **J. Ender**, R. Orio, T. Hadámek, W. Loch, N. Jørstad, W. Goes, S. Selberherr, "Interface Effects in Ultra-Scaled MRAM Cells", 2022, in *Letters from the 8th Joint International EuroSOI Workshop and International Conference on Ultimate Integration on Silicon (EuroSOI-ULIS) 2022*, doi: 10.1016/j.sse.2022.108373

[68] S. Fiorentini, **J. Ender**, S. Selberherr, W. Goes, V. Sverdlov, "Spin Transfer Torque Evaluation Based on Coupled Spin and Charge Transport: A Finite Element Method Approach", pp. 40–44, 2022, in *The 26th World Multi-Conference on Systemics, Cybernetics and Informatics: WMSCI 2022. Proceedings Volume II.*

[69] S. Fiorentini, M. Bendra, **J. Ender**, W. Goes, V. Sverdlov, S. Selberherr, "Evaluating Spin Transfer Torques in Multilayered Magnetic Tunnel Junctions and Spin Valves", pp. 44–45, 2022, in *Workshop on Innovative Nanoscale Devices and Systems. Book of Abstracts.*

[70] M. Bendra, S. Fiorentini, **J. Ender**, R. Orio, T. Hadámek, W. Loch, N. Jørstad, S. Selberherr, W. Goes, V. Sverdlov, "Spin Transfer Torques in Ultra-Scaled MRAM Cells", pp. 129–132, 2022, in *2022 45th Jubilee International Convention on Information, Communication and Electronic Technology (MIPRO).*

[71] **J. Ender**, S. Fiorentini, R. Orio, T. Hadámek, M. Bendra, W. Goes, S. Selberherr, V. Sverdlov, "Advances in Modeling Emerging Magnetoresistive Random Access Memories: From Finite Element Methods to Machine Learning Approaches", 2022, in *Proc. SPIE 12157, International Conference on Micro- and Nano-Electronics 2021*, ISSN: 0277-786x, doi: 10.1117/12.2624595

[72] V. Sverdlov, M. Bendra, S. Fiorentini, **J. Ender**, R. Orio, T. Hadámek, W. Loch, N. Jørstad, S. Selberherr, "Modeling Advanced Magnetoresistive Memory: A Journey from Finite Element Methods to Machine Learning Approaches", 2022, in *2nd Global Webinar on Nanoscience & Nanotechnology.*

[73] **J. Ender**, R. Orio, W. Goes, V. Sverdlov, "Towards Efficient SOT-assisted STT-MRAM Cell Switching using Reinforcement Learning", pp. 39–39, 2023, in *14th International Conference, Large-Scale Scientific Computations LSSC'23 : Scientific Program, Abstracts, List of Participants*.